

Driven and Thermal Microparticle Rheology of Complex Biopolymer Systems

by
Jeremy Cribb

A dissertation submitted to the faculty of the University of North Carolina at Chapel Hill in partial fulfillment of the requirements for the degree of Doctor of Philosophy in the Department of Biomedical Engineering.

Chapel Hill
2010

Approved by:

Rich Superfine, Advisor

Michael Rubinstein, Reader

M. Greg Forest, Reader

John Sheehan, Reader

Henry Hsiao, Reader

© 2010
Jeremy Cribb
ALL RIGHTS RESERVED

ABSTRACT

**JEREMY CRIBB: Driven and Thermal Microparticle Rheology of
Complex Biopolymer Systems.
(Under the direction of Rich Superfine.)**

Mucociliary clearance is the process by which cilia actively transport mucus from the airway in order to keep a sterile environment in the lung. The flow properties, or the rheology, of mucus is of particular importance when considering mucus function since its modulus and viscosity result in net mucociliary transport. For example, when the protective layer of mucus is too thick, transport stops because the cilia cannot carry the increased load, as is the case in several lung-related pathologies like cystic fibrosis, COPD, and asthma.

The 3DFM is an instrument we designed, implemented, and validated in our lab. Evolving significantly over the last several years, the 3DFM is a system that can image and manipulate biological specimens in all three spatial dimensions at microscopic length scales. When we subject a bead embedded in a fluid to an applied force, its spatiotemporal response depends on the rheological properties of the surrounding fluid. For example, in a Newtonian fluid the terminal velocity of a bead is inversely proportional to the fluid viscosity.

Applying magnetic forces to micron sized spheres or even rod-shaped particles (i.e. bacteria or magnetically permeable nanoparticles) allows us to study the correspondence (or lack thereof) between micro-physical measurements and the canonical characterizations of macroscopic rheology techniques like cone-and-plate rheometers. Also,

such a microscale technique is desirable since it is often difficult to acquire sufficient volume of a purified biological sample to test using macroscale rheological techniques such as cone and plate. Biological systems can also be highly heterogeneous and present a challenge for any measurement technique because of this variability. Finally, we must mention the necessity of performing measurements at relevant length scales since evolutionary pressure is the driving force for these biopolymer systems.

Here I will argue the usefulness of driven microbead rheology (DMBR) as a measurement technique for soft biopolymer solutions. I begin by explaining the effects of probe shape and make first observations regarding a preference in particle shape for drug delivery. Next, I describe the fundamental measurements in our DMBR system and offer data for well-characterized Newtonian and homogeneous viscoelastic polymer solutions. I will present experimental results and will establish the ability of DMBR as a technique for measuring both linear and nonlinear properties of non-Newtonian fluids. Finally, there will be particular attention on strain-thickening, a dynamic and nonlinear rheological property of mucus that I have observed for the first time at the microscale, making it interesting in understanding mucociliary clearance.

ACKNOWLEDGMENTS

It takes a village...never before have truer words been spoken, just probably not about a mere graduate student. This adventure has taken me longer than anyone expected and about half as long as I would have liked. I believe that speaks loudly and clearly about the wonderful time I have had in graduate school and the caliber of people that I have had the pleasure to work beside.

I would like to first thank my committee: Rich, my thesis and research advisor, “thabks for thid” [sic]. I find your energy and love for science and engineering infectious. I just hope that someday I can manage to wrangle grants as effectively as you. To Greg, Michael, and Henry, thanks for your patience with my plasticized deadlines. Bill, thank you for my first chance to work in an academic lab and for stepping in for John when necessary for whatever reason. Finally, John, I thought only kids found mucus cool, but I was very, very wrong. You continually trod along through stuff children even fear to tread.

As for my family, I must first thank my parents and my grandmother. Their unshakable belief in me and their willingness to fill a dollar gap here and there allowed me to focus on the work. My sisters, Becky and Erin, have always been quite successful at managing “big head” and must be thanked for occasionally venting the ego of and pol-

ishing the pulpit for their older brother. McClain, your laugh and voluntary deafness speak for themselves. Morgan... what can I say? Thank you for your patience. Some day you may fully understand my absence. Even so, with all these miles between us, I think of you and miss you relentlessly every day.

To computer science folks: I have much gratitude for the many colleagues that helped this information on the instrumentation come together. Without Russ Taylor and Ryan Schubert, my many whinings regarding the functionality of the Video Spot Tracker would go unheard, and worse, unchanged. I must also acknowledge the CS group for providing me access to the BASS supercomputer which I used to model bead paths for the strain thickening project.

On the colleague front: Ben Wilde for an irreverent sense of humor and an exquisite job functioning as the lab's EHO, Jay Fisher for flight support, the occasional pint, and the countless explanations of optics and 3DFM hardware, Kalpit Desai for his intricate knowledge of DAQ and DSP and his paperclip manufacturing pockets, David Hill for his assistance in experiments and tutelage in diffusion, Ben Evans and Leandra Vicci for their patience in helping me to understand magnetics, Adam Shields for the philosophical side of everything (ever find out what it all means?), Jerome for myriad distractions with questions I would never think to ask, Tim Meehan for teaching me how to write a scientific paper effortlessly, Tim O'Brien for his boundless optimism, and finally Ricky Spero for unknowingly teaching me to accept and manage minions.

To those students tasked with assisting me: First the "Triforce of Microrheology"—Thanks to Stephen Norris for dedicating his time to help advance my work at first

without pay, Patrick Moore for the excitement he brought to the project as well as the early versions of the Rolie-Poly modeling, Sheel Shah for his patience in dealing with my infantile questions like "What's a tensor ϵ ," as well as modeling the maximum shear rate for the prolate spheroid. Other students played pivotal roles as well: David Bober's help with the variable force calibration technique has promoted the driven-bead experiments for every member of the lab as well as visiting collaborators and workshop attendees. Briana Fiser provided many hours of her time first by helping me process strain thickening data by hand and then by writing the Matlab code that largely automated the process.

To my friends: I would like to thank Nicole for the swift kick in the pants with the "what are you waiting for?" line of questioning. Renee and Mike, thank you so much for your moral support and willingness to read through this fascinating and exciting piece of literature. Genevieve, I miss you terribly, dear, and I know you are just waiting along with Titan and Banjo for us to continue our frequent treks through Carolina North. We shall continue in short order, I do apologize for the delay.

To Juan, for being the Yin to my Yin and the Yang to my Yang.

Finally, I would like to dedicate this work to two unrelated people that share a space within though they are no longer here. To my Paw-Paw: I will never forget your pride, your relentless work ethic, and your endless questioning about the "letters behind my name" you never got to see. To Gloria Suarez: I value her dearly for her expansive positive attitude, boundless energy, and crystallized sense-of-self, but mostly I must thank her for the existential experience that goes along with losing someone like her.

Contents

List of Tables	xv
List of Figures	xvi
1 Introduction	1
1.1 Overview	1
1.2 Thesis statement and contributions	5
1.3 Outline	7
2 Measuring Microrheology	9
2.1 Overview	9
2.2 Probe Geometries and Navier-Stokes	10
2.2.1 Momentum balance produces the equation of motion.	11
2.2.2 Constitutive laws relate stress to flow (strain-rate)	12
2.2.3 The Navier-Stokes Equation	13
2.2.4 Stream Functions	14
2.2.5 Solving for Stokes flow	16
2.2.6 The Cone and Plate Rheometer	17
2.2.7 Spherical Probe Geometry	20

2.2.8	Rod Probe Geometry	26
2.3	Passive Microrheology	31
2.4	Active microrheology	38
2.4.1	Magnetic Force on a Spherical Particle	43
2.4.2	Magnetic Force on a Rod-shaped Particle	45
2.5	Conclusions	48
3	The 3DFM as a microrheometer	49
3.1	Overview	49
3.2	Methods	50
3.2.1	Sample Preparation	50
3.2.2	Bead PEGylation	51
3.2.3	Distributing beads into a sample	51
3.2.4	Boundary Effects	52
3.3	Video Subsystem	55
3.3.1	Image Acquisition	57
3.3.2	Data Collection	58
3.3.3	GLUItake Software	59
3.3.4	Particle Tracking	61
3.3.5	Measurement Resolution	62
3.3.6	Editing Video Tracking Data	64
3.4	Magnetics Subsystem	65

3.4.1	The Magnetics Stage	67
3.4.2	Pole Tips	68
3.4.3	Calibrating with Newtonian Fluids	70
3.4.4	Variable Force Calibration	73
3.5	Limits of measure with 3DFM Rheometry	86
3.5.1	Thermal Methods	86
3.5.2	Driven Methods	89
3.5.3	Measurements of Selected Biopolymer Systems	90
3.6	Predicting Force Requirements	92
3.7	Conclusions	94
4	Multiscale Rheology of selected biofluids	97
4.1	Overview	97
4.2	Polymer systems	99
4.3	DNA	101
4.3.1	CAP	106
4.3.2	TMBR	111
4.3.3	DMBR	113
4.4	HA	120
4.5	Guar	124
4.6	PGM	126
4.7	Mucus	128

4.8	Discussion	134
4.9	Conclusions	135
5	Shape Effects	137
5.1	Overview	137
5.2	Background	138
5.3	Methodology	142
5.3.1	Nanoparticles	142
5.3.2	Magnetic Characterization of Nanoparticles	143
5.3.3	Newtonian fluid and Viscoelastic λ -DNA solution	145
5.3.4	Viscometry of transport media	146
5.3.5	Microparticle Magnetophoresis Apparatus	147
5.3.6	Modeling and Measuring Field and Field Gradient	149
5.3.7	Quantitative Microparticle Magnetophoresis	150
5.3.8	Stokes Drag Forces	150
5.3.9	Validating Particle Transport Experiments	151
5.3.10	Estimating Shear Thinning	151
5.3.11	Shape Effect Attributes	153
5.4	Results	157
5.4.1	Solution Viscometry	157
5.4.2	Nanoparticle Magnetic Properties	158
5.4.3	Magnetic Forces on Particles	159

5.4.4	Driven particle transport in complex fluids	160
5.5	Discussion	163
5.6	Conclusions	168
6	Strain Thickening	170
6.1	Overview	170
6.2	Introduction	172
6.3	Background	173
6.4	Nonlinear active microrheology	175
6.5	Materials and Methods	176
6.5.1	Probes	176
6.5.2	Solutions	177
6.5.3	Light Scattering	177
6.5.4	CAP Methods	178
6.5.5	DMBR Methods	179
6.5.6	Force Actuation and Extraction of VE parameters	181
6.6	Results	182
6.7	What the DSTE is NOT	185
6.7.1	Edge Effects	185
6.7.2	Local Concentration Inhomogeneities	186
6.7.3	DNA Sticks to Bead	187
6.7.4	Dynamic Instability	188

6.8	Rolie-Poly model	191
6.9	Modeling a Rolie-Poly fluid around a moving sphere	192
6.9.1	Parameters for Rolie-Poly simulations	194
6.10	Results	194
6.11	Discussion	199
6.12	Conclusions	200
7	Conclusion	201
A	Reagent Protocols	203
A.1	Preparation of Newtonian Fluids	203
A.1.1	2 M Sucrose Solution	203
A.1.2	2.5 M Sucrose Solution	204
A.1.3	Corn Syrup	204
A.2	Bead PEGylation	204
A.2.1	Materials	204
A.2.2	Reaction Protocol	205
A.3	Distributing Probes into Specimen	206
A.4	Vortex Addition	208
A.5	λ -DNA Polymer System	208
A.6	Concentrating λ -DNA	215
A.6.1	Microcentrifugation	215
A.6.2	Alcoholic Precipitation	216

B Optimized Sequences for Variable Force Calibration	219
Bibliography	222

List of Tables

3.1	Magnetic Materials used for 3DFM pole tips	69
3.2	Measurement of Newtonian Viscosity	70
3.3	Newtonian Standard Solutions used in VFC	72
4.1	Summary of intrinsic polymer system modeling parameters.	100
4.2	Summary of extrinsic polymer system modeling parameters.	100
4.3	Persistence lengths for several biopolymers.	102
4.4	Human Mucin Family	129
5.1	Carreau Parameters for λ -DNA solutions	146
5.2	Ratios of Particle Velocity	163
6.1	Measurements of Molecular Weight and Radius of Gyration.	178
6.2	RP parameters for different polymer systems.	194

List of Figures

2.1	Schematic of CAP Rheometer	21
2.2	Fluid stresses on a Sphere	25
2.3	Shear rate imposed on fluid by bead	25
2.4	Expected MSD for spheres	36
2.5	The Maxwell model and its strain response	41
2.6	Kelvin-Voight Model: the viscoelastic solid and its strain response	42
2.7	The Jeffrey model: strain response to input stress	44
2.8	Effect of aspect ratio on demagnetization factor	47
3.1	Dispersing dry beads into specimen	53
3.2	End and Edge Effects	55
3.3	Video flow diagram	57
3.4	User Interface for GLUItake	60
3.5	Flow diagram for GLUItake	61
3.6	Position noise for Hercules video tracking system	63
3.7	Position noise for Hercules laser tracking system	64
3.8	Variable Force Calibration Contour Plot	66
3.9	3DFM thin-foil clam-shell magnetics stage	68

3.10	<i>Pole flat</i> magnetic geometry	69
3.11	Degauss Routine for 3DFM magnets	74
3.12	Effect of degauss on bead displacement	76
3.13	Voltage sequence applied to magnetics system	77
3.14	Locating Virtual monopole in 3DFM	79
3.15	Force vs. Distance from poletip	81
3.16	Dependence of Force on 3DFM Input Current	83
3.17	Saturation of Poletip	84
3.18	Forces on MyOne beads, 10 μm from pole-tip surface	86
3.19	Limits of Measure for TMBR	88
3.20	Limits of Measure for TMBR and DMBR	90
3.21	Biomaterials, measurable with TMBR and/or DMBR	91
3.22	Force requirements for spheres in PGM	95
4.1	CAP Strain Amplitude Sweep for 1.4 mg/mL λ -DNA	107
4.2	Viscoelastic frequency response of λ -DNA using CAP	110
4.3	CAP Shear Thinning in λ -DNA	111
4.4	MSD for λ -DNA Solutions using TMBR	114
4.5	Slow DMBR pull in 1.4 mg/mL λ -DNA	115
4.6	DMBR of λ -DNA	116
4.7	Sensitivity of Probe to Specimen History	119

4.8	Multiscale Rheology of DNA	119
4.9	DMBR Creep for 10mg/mL HA	122
4.10	Linear and nonlinear viscoelastic response in DMBR	123
4.11	HA does not shear thin at shear rates tested with DMBR	124
4.12	CAP and DMBR shear thinning in Guar	125
4.13	PGM CAP and DMBR rheology	127
4.14	Heterogeneous viscoelastic response in human sputum using DMBR . . .	130
4.15	DNA and actin in mucus	133
4.16	Multiscale measurements for HBE mucus	134
4.17	Viscoelastic phase plane of Mucus and DNA	135
5.1	SEM of nanoparticles used in DMBR experiments	143
5.2	SQUID characterization of beads and rods	144
5.3	Magnetophoretic apparatus	148
5.4	Definition of Aspect Ratio	157
5.5	Viscosity of Newtonian Standard, measured by CAP, beads, and nanorods	158
5.6	Magnetic Forces on beads and rods due to field and field gradient . . .	160
5.7	Normalized Mobility of Transport Particles	162
5.8	Shear Thinning in λ -DNA with nanorods	164
6.1	Viscosity Overshoots in 1.5 mg/mL λ -DNA from Teixeira, 2007	179
6.2	Overshoots in Viscosity in 1% guar using CAP	180

6.3	Two Examples of DSTE	183
6.4	Schematic of Strain Thickening in DMBR	184
6.5	Dynamic Instability	189
6.6	Simulated bead displacement in a Rolie-Poly fluid	195
6.7	Simulated compliance in a Rolie-Poly fluid	196
6.8	Simulated Shear thinning in a Rolie-Poly fluid	197
6.9	CAP & simulated shear thinning in DNA	197
6.10	Simulated strain thickening in a Rolie-Poly fluid	198
6.11	Strain Thickening in DMBR	199

Chapter 1

Introduction

1.1 Overview

Materials fascinate us. Anthropologists named the early ages of history for our ability to engineer tools with particular materials. Stone, bronze, and iron all require specific knowledge and innovation before successful fracturing, shaping, or smelting can occur. Early engineers must have found the challenge exciting, with each new incremental development expanding the state-of-the-art. Alongside the evolution of our engineering ability and our machines, we as humans evolved a passionate interest in the study of human disease. We have hence tasked ourselves with curing ills that range from simple inconvenient aches to incurable conditions. A most interesting development in our technology over the past 60 years is the explosion in our understanding of biomaterials, the most complex materials in our world.

Nature works patiently, taking millennia to design strategies for handling any given type of environmental pressure. In many cases these methods produced biopolymers like proteins or carbohydrate chains that function as fundamental structural elements.

Combining these constituent elements in various ways allows nature to create a diverse array of materials such as bone, keratin, tubulin, actin, fibrin, DNA, or mucus, whereby all exhibit vast differences from one another in their physical properties. These materials form biopolymer systems that can safely encode genetic information, solve diverse morphological challenges, and provide protection against invading microorganisms.

All of these substances exist as viscoelastic (VE) materials, located somewhere between the canonical liquid and solid phases of matter and most exhibit easily measurable properties of both phases. As such, VE materials have time-dependent responses where they store energy in the network as well as dissipate it into the background solvent. Storing energy in the polymer network results in a material similar to mayonnaise that holds its shape better than a typical liquid under a small load but flows when subjected to sufficient stress.

Rheology is the term used to describe the study of VE materials. Coined by Eugene Bingham in 1920, the word is derived from the Greek verb, $\rho\epsilon\upsilon\upsilon$, which means *to flow*. Thus, rheology is the study of the deformation of matter subjected to an external force or, more specifically, to an anisotropic stress (Macosko and Larson, 1994).

Here, I will focus on creating a reliable methodology for studying the rheology of mucus, the biopolymer system for mucociliary clearance (MCC). Our bodies use MCC to free our lungs of collected debris and pathogens and keep us healthy. Mucus serves as a moving trap for inhaled particulates, including bacteria. A sterile environment is maintained in the lung through the MCC process, where cellular organelles called cilia actively beat and propel mucus along the lung's surface. A hydrodynamic perspective

on MCC would argue that because the cilia are ultimately force-limited (Hill et al., 2010), it is the *rheology* of the mucus that dictates successful MCC (Eliezer et al., 1970). Suboptimal MCC leads to the devastating properties of the pathology of several respiratory diseases, including chronic obstructive pulmonary disorder (COPD), asthma, and cystic fibrosis (CF).

Rheology is of particular importance when considering mucus function since its modulus and viscosity must be optimal for successful transport (Shih et al., 1977; Puchelle et al., 1980a; Chen and Dulfano, 1978). If the protective layer of mucus is too elastic, transport ceases because the cilia, which are responsible for moving it, cannot carry the increased load (Hill et al., 2010). In contrast, if the elasticity is too small, the fluid might not maintain its association with a vertical surface and could collect in the bottom of the lung due to gravimetric flow (King and Macklem, 1977).

To determine the rheology of a viscoelastic material, we need a volume of the testing material and an instrument capable of measuring the response to a known input strain rate or stress. The conventional instrumentation for making such measurements is the macroscale cone-and-plate (CAP) rheometer. The CAP geometry imparts a simple uniform shear rate in the material for a given stress (or vice versa) and measures the rheology of materials at length scales that can range from 10^{-4} m to 10^{-2} m with volumes as small as 100 μm . Collecting enough mucus to use in conventional cone and plate (CAP) rheometry is extremely difficult, costly, and time-consuming.

In contrast, our microscale rheology techniques can take microliter volumes of mucus directly from a single cell culture and perform similar measurements as seen in CAP,

except at smaller and physiologically relevant length scales. At these smaller length scales CAP averages out heterogeneity. Whatever the method, I retain the fundamental hypothesis that mucus is first and foremost a collection of heavily glycosylated proteins that cooperate to form a polymer network and that associations between these proteins might form transient crosslinks, possibly by smaller linking molecules. Mucus is therefore not a homopolymer system, nor is it spatially homogeneous. This hypothesis guides the logic I use to create the aforementioned methodology.

I make use of both the homogeneous, macroscale shear field when acquiring measurements with CAP and the heterogeneous shear field when I use microrheology techniques. I assume that all specimens I examine are spatially homogeneous at the length scales explored by the probe so that I might use the principles of continuum mechanics. Again, this assumption of continuity has its hazards as it requires the dominant length scales of the specimen to be smaller than the probe used to measure the physical properties. Also, I do not consider other processes that may be vitally important in MCC, such as osmotic pressure or mucin adhesion.

Using the 3D force microscope (3DFM), an instrument designed, implemented, and validated in our lab, we can make microrheological measurements (Fisher et al., 2005). Ultimately, the 3DFM is a system that images and manipulates biological samples in all three spatial dimensions at microscopic length scales. Among others, the 3DFM includes a magnetics subsystem encapsulated in a modular shell into which I place a 2 μL specimen volume (see Figure 3.9). The entire assembly fits into the body of a commercially manufactured inverted optical microscope. Thin films of μ -metal

in various geometries channel magnetic flux to the region of interest. Magnetomotive force actuates the displacement of magnetic particles embedded in the specimen. While some pole geometries generate forces with variable magnitudes in any direction, others sacrifice directional control for a supplemented force magnitude (Fisher et al., 2006a; Fisher et al., 2006b).

When we subject a bead embedded in a fluid to an applied force, its spatiotemporal response depends on the rheological properties of the surrounding fluid (Zwanzig and Bixon, 1970). For example, in a Newtonian fluid the terminal velocity of a bead is inversely proportional to the fluid viscosity (Happel and Brenner, 1991). Applying magnetic forces allows us to study the correspondence between micro-physical measurements and the canonical characterizations of macroscopic rheology techniques like CAP rheometers.

This work is my contribution to the state-of-the-art, a continuing effort to better understand the material properties of these biopolymer systems and to develop tools to study them.

1.2 Thesis statement and contributions

The thesis here argues the usefulness of driven microbead rheology (DMBR) as a measurement technique for the non-Newtonian rheology of soft biopolymer solutions. I begin with by comparing the flow fields and stresses for both macroscale CAP and microscale particle rheologies for both spherical and rod-like geometries. I then follow

with a review of the literature and describe the theory behind both thermal and driven microbead rheology techniques. In subsequent chapters, I introduce the 3DFM, our DMBR system, and describe how we calibrate our applied forces, and validate our 3DFM microrheology measurements. I offer data for well-characterized Newtonian and homogeneous viscoelastic polymer solutions and present experimental results, thereby establishing the ability of DMBR as a technique that can consistently measure both linear and non-linear properties of non-Newtonian fluids for the first time. Next, I study how probe shape affects the surrounding system rheology and make first observations regarding a preference in particle shape for drug delivery. Finally, I present a study on strain-thickening, a dynamic rheological property not previously reported in the literature at the microscale. I have successfully made first measurements of strain thickening in DNA, guar, porcine gastric mucus, as well as in human mucus which may help explain the mechanism behind mucociliary clearance.

Biological systems can present a challenge for any measurement technique because of their wide variability and the lack of knowledge of their constituent elements. It is also often difficult to acquire sufficient volume of a purified sample to test using macroscale rheological techniques such as CAP. Finally, we must mention the necessity of performing measurements at relevant length scales since evolutionary pressure is the driving force for these biopolymer systems. Based on the wide range of topics addressed in this dissertation, the information herein contributes directly to the studies of rheology and biomaterials and illuminates possible mechanisms for successful mucociliary transport.

1.3 Outline

This work is organized as follows:

Chapter 2 models a sphere moving through a Newtonian fluid with the Navier-Stokes (NS) equation and uses it to review current passive and driven microbead techniques. The NS equation provides a framework that can predict shear thinning and even strain thickening of material that surrounds a bead when it is subjected to an externally applied force. Results from this microscale modeling are then compared with reviewed macroscale cone and plate methods. Emphasis is placed on mechanical models used in CAP and how microscale measurements correspond to these models. I use this information to generate a methodology for performing these experiments in the microscale.

In Chapter 3, I explain the general design of the 3D force microscope (3DFM) and its implementation as a microrheometer. The video and tracking systems will be illustrated along with their limits of measure. Additionally, I will highlight a new method called variable force calibration (VFC) that we now use to quantify the magnetic forces in the 3DFM as a function of both drive current and distance from the pole-tip. Concluding this chapter will be an error analysis of our methods.

Chapter 4 uses polymer physics to model several polymer solutions including DNA, HA, and mucus. I will expand on the Navier-Stokes interpretation for the experimental design and then present CAP and DMBR data that shows the correspondence between macroscale and microscale measurements at steady state.

Chapter 5 discusses the effects of shape on the mobility of sub-micron particles

through basic Newtonian as well as shear-thinning viscoelastic biopolymer solutions. Considering a particle's shape offers the scientist another parameter to modify when considering tradeoffs in payload and rate of transport in nanoscale drug delivery systems.

Chapter 6 ramps up the complexity of the modeling and shows probe sensitivity to measurements of dynamic phenomena in viscoelastic materials. Strain thickening is shown as a dynamic, non-linear rheological response of polymer systems at the micron-sized length scales. A spontaneous shift from high to low viscosity occurs at a quasi-steady state velocity. I will show this behavior in data collected for several polymer systems: DNA, reconstituted PGM, guar gum, and human mucus. Because mucus exhibits this nonlinear response, it may offer profound implications in the mechanism used by cilia in successful mucociliary transport.

A global discussion about these results along with conclusions and future directions follows in Chapter 7.

Chapter 2

Measuring Microrheology

2.1 Overview

Typical microparticle rheology techniques include the passive or active transport of particles such as spheres or prolate ellipsoids through a viscoelastic medium. Over macroscale techniques such as cone and plate (CAP), microrheology offers the advantages of smaller sample size, sensitivity to heterogeneity, and physiologically relevant probe sizes. In this chapter I begin with a general description of the physics involved when a material experiences a stress/strain inside a CAP rheometer and then follow with the microscale analog when a spherical or prolate ellipsoidal particle is pulled through a viscous medium. This description will use the Navier-Stokes equation and general concepts of fluid mechanics to wed both thermal and driven microbead rheology techniques to macroscale CAP. With these concepts in hand we can measure for the first time shear-thinning and even strain-thickening of surrounding biomaterials when the probe is subjected to an externally applied force. I find in such experiments that the maximum shear rate dominates the responses for both beads (Chapter 4) and rod-

shaped (Chapter 5) microparticles in a shear thinning fluid. For driven microparticle techniques, emphasis is placed on mechanical models used in CAP rheometry and how microscale measurements can correspond to these models. Later, in Chapters 4, 5, and 6, I will present empirical results from experiments that show these relationships for both microscale methods and compare them with reviewed macroscale CAP methods.

2.2 Probe Geometries and Navier-Stokes

Types of flow in fluids can be described in several different ways. Fluid flow can be *laminar* or *turbulent*, terms which describe the direction of adjacent fluid parcels wherein a “parcel” describes an infinitesimal volume element of fluid. When the streamlines for two closely spaced fluid parcels are parallel, the flow is called laminar whereas nonparallel streamlines indicate turbulent flow conditions. Flow is also described as steady or unsteady. In unsteady flow there is no restriction on the velocity of fluid parcels, whereas in steady flow, the velocity is not allowed to change with respect to time. Other types of flows include rotational flows, which describe the motion of fluid parcels around an axis of rotation, versus uniform flows which have identical velocity magnitude and direction at all points in space.

The Navier-Stokes (NS) equation (Eq. 2.10) provides a generalized framework for understanding both thermal and driven microparticle rheologies. To derive the NS equation, I first restrict flows to particular types and apply assumptions about them in order to derive a flow field. Secondly, I identify the fundamental equation of motion for

a fluid parcel. Lastly, I apply the constitutive equation for a Newtonian fluid, which defines the relationship between stress and strain rate.

2.2.1 Momentum balance produces the equation of motion.

In continuum mechanics, solving for the balance of forces on a fluid parcel using Newton's Second Law results in

$$\rho \frac{D\vec{v}}{Dt} = -\nabla \cdot \underline{\underline{\Pi}} + \vec{F} \quad (2.1)$$

where \vec{F} describes an externally applied force such as gravity ($\vec{F} = \rho\vec{g}$). The operator D/Dt defines the substantive derivative, equal to

$$\frac{D}{Dt} = \partial/\partial t + \vec{v} \cdot \nabla \quad (2.2)$$

and when used it provides a clearer view of Equation 2.1 as a momentum balance. Finally, $\underline{\underline{\Pi}}$ is the total stress tensor, which is a sum of the isotropic stress, or bulk pressure, p , and the extra stress tensor, $\underline{\underline{\sigma}}$

$$\underline{\underline{\Pi}} = p\underline{\underline{I}} + \underline{\underline{\sigma}} \quad (2.3)$$

Expanding $\underline{\underline{\Pi}}$ and simplifying the right side of Equation 2.1 results in the equation of motion in terms of $\underline{\underline{\sigma}}$

$$\rho \frac{D\vec{v}}{Dt} = -\nabla p - \nabla \cdot \underline{\underline{\sigma}} + \vec{F} \quad (2.4)$$

2.2.2 Constitutive laws relate stress to flow (strain-rate)

The Navier-Stokes equation describes the motion of a Newtonian fluid. It intrinsically contains a constitutive equation which is empirically derived from observations in the lab and defines the relationship between the stress, $\underline{\underline{\sigma}}$, and the strain rate $\underline{\underline{\dot{\gamma}}}$. The constitutive equation for a compressible Newtonian fluid is

$$\underline{\underline{\sigma}} = -\eta \left[\nabla \vec{v} + (\nabla \vec{v})^T \right] + \left(\frac{2\eta}{3} - \kappa \right) (\nabla \cdot \vec{v}) \underline{\underline{I}} \quad (2.5)$$

where η is the shear viscosity, κ is the dilatational viscosity, and $\underline{\underline{I}}$ is the identity tensor (Morrison, 2001). If we assume the fluid is incompressible, then, at any given moment the mass entering the system is exactly equal to the mass exiting the system. Mathematically this is easily described as the zero divergence of the velocity field

$$\nabla \cdot \vec{v} = 0 \quad (2.6)$$

where Equation 2.6 is called the continuity equation for incompressible fluids. For an incompressible Newtonian fluid we can substitute the continuity equation and simplify the constitutive relation to

$$\underline{\underline{\sigma}} = -\eta \left[\nabla \vec{v} + (\nabla \vec{v})^T \right] \quad (2.7)$$

Then we define the strain rate tensor as

$$\underline{\underline{\dot{\gamma}}} = \nabla \vec{v} + (\nabla \vec{v})^T \quad (2.8)$$

reducing the expression to a tensor form similar to Newton's first description of viscous drag

$$\underline{\underline{\sigma}} = \eta \underline{\underline{\dot{\gamma}}} \quad (2.9)$$

. The above equation is the constitutive law for an incompressible Newtonian fluid, where the fluid stress is related to its resulting strain rate through a constant viscosity. Several models in the literature provide progressively more complex constitutive laws that attempt to replicate the behavior of non-Newtonian fluids. The Rolie-Poly model is another constitutive equation that uses polymer physics principles such as reptation and convective-constraint release (CCR) to model non-Newtonian behavior like strain thickening and shear thinning found in some polymer systems ([Likhtman and Graham, 2003](#)). I discuss this constitutive equation in more detail and use it to model flow in biopolymer systems in Chapter 6.

2.2.3 The Navier-Stokes Equation

Substituting the Newtonian constitutive equation (Eq. 2.9) into the equation of motion (Eq. 2.4) results in the common form of the Navier-Stokes relationship for incompressible, Newtonian flows

$$\rho \frac{D\vec{v}}{Dt} = -\nabla p + \eta \nabla^2 \vec{v} + \vec{F} \quad (2.10)$$

To reduce the NS equation to the simpler Stokes equation, we assume steady, creeping flow conditions such that $D\vec{v}/Dt = 0$. In order to validate this assumption, I need to

be able to disregard the inertial terms so that the velocity field does not change with respect to time ($\partial\vec{v}/\partial t = 0$). In a liquid, motion at the microscopic scale is highly dissipative, as shown by the dimensionless Reynolds number, Re , defined as the ratio of inertial to viscous forces, or

$$Re = \frac{\rho v L}{\eta} \quad (2.11)$$

where L and v are characteristic length and velocity scales, ρ and η are the density and viscosity of the surrounding medium. When Re is sufficiently low ($Re \ll 1$), the inertial effects become vanishingly small (Purcell, 1977), thus minimizing the impact the object's mass has on its own motion, and eliminating any turbulence in the now laminar flow field. For a neutrally buoyant $1 \mu\text{m}$ bead in water (1 mPa s) moving at $100 \mu\text{m/s}$, the Re is 10^{-4} , well within the low Reynolds number regime.

When in the low Reynolds number regime, the NS equation becomes equivalent to the Stokes equation (Happel and Brenner, 1991),

$$\nabla p = \eta \nabla^2 \vec{v} + \vec{F} \quad (2.12)$$

2.2.4 Stream Functions

Utilizing streamlines is a convenient method for representing and visualizing a two-dimensional flow field for Stokes flows. Computed from the aptly named stream function, ψ , streamlines indicate the direction of flow because, by definition, the direction of the velocity vector field is always tangent to the streamline at every point. Con-

ceptually, the streamline traces the paths of neutrally buoyant, non-diffusing, passive particle trajectories in a steady flow.

A number of conditions must be met to allow the use of the stream function. First, it must be true that the flow field be irrotational, meaning that the vorticity (curl) must be equal to zero

$$\nabla \times \vec{v} = \left(\frac{\partial v_z}{\partial y} - \frac{\partial v_y}{\partial z} \right) \hat{i} + \left(\frac{\partial v_x}{\partial z} - \frac{\partial v_z}{\partial x} \right) \hat{j} + \left(\frac{\partial v_y}{\partial x} - \frac{\partial v_x}{\partial y} \right) \hat{k} = 0 \quad (2.13)$$

Flows such as these are called potential flows. In a potential flow, \vec{v} must be equal to the gradient of a scalar function called the velocity potential, ϕ , described mathematically as

$$\vec{v} = \nabla \phi = \frac{\partial \phi}{\partial x} \hat{i} + \frac{\partial \phi}{\partial y} \hat{j} + \frac{\partial \phi}{\partial z} \hat{k} \quad (2.14)$$

Secondly, we must meet the conditions of continuity (Eq. 2.6), meaning that

$$\nabla \cdot \vec{v} = \frac{\partial v_x}{\partial x} + \frac{\partial v_y}{\partial y} + \frac{\partial v_z}{\partial z} = \nabla \cdot \nabla \phi = \nabla^2 \phi = 0 \quad (2.15)$$

where ∇^2 is the Laplacian operator, which in Cartesian coordinates is

$$\frac{\partial^2 \phi}{\partial x^2} + \frac{\partial^2 \phi}{\partial y^2} + \frac{\partial^2 \phi}{\partial z^2} = 0 \quad (2.16)$$

for the velocity potential.

For planar flow in xy , the stream function, ψ , is defined as a function of x and y ,

i.e. $\psi = \psi(x, y)$, making v_z and $\partial/\partial z$ both zero in Equations 2.13 through 2.16. In these flows, the streamline functions are defined as

$$v_y = \frac{\partial\psi}{\partial y} \quad (2.17)$$

$$v_x = \frac{-\partial\psi}{\partial x} \quad (2.18)$$

which is equivalent to

$$\vec{v} = \nabla \times \vec{\psi} \quad (2.19)$$

where $\vec{v} = v_x\hat{i} + v_y\hat{j}$ and $\vec{\psi} = \psi\hat{k}$.

2.2.5 Solving for Stokes flow

Substituting the continuity equation (Eq. 2.6) into the Stokes equation, shown as Equation 2.12, expands in two dimensions to

$$-\frac{\partial p}{\partial x} + \eta \left(\frac{\partial^2 v_x}{\partial x^2} + \frac{\partial^2 v_x}{\partial y^2} \right) = 0 \quad (2.20)$$

$$-\frac{\partial p}{\partial y} + \eta \left(\frac{\partial^2 v_y}{\partial x^2} + \frac{\partial^2 v_y}{\partial y^2} \right) = 0 \quad (2.21)$$

Using the stream functions defined for planar flow in Equations 2.17 and 2.18, differentiating with respect to y and x and subtracting equations, one can eliminate the pressure term and result in a fourth order differential equation that in Cartesian coordinates is

$$\frac{\partial^4 \psi}{\partial x^4} + \frac{2\partial^4 \psi}{\partial x^2 \partial y^2} + \frac{\partial^4 \psi}{\partial y^4} = 0 \quad (2.22)$$

which is equivalent to

$$\nabla^4 \psi = 0 \tag{2.23}$$

with the biharmonic operator, ∇^4 , defined in Cartesian coordinates as

$$\nabla^4 = \nabla^2 (\nabla^2) = \frac{\partial^4}{\partial x^4} + \frac{2\partial^4}{\partial x^2 \partial y^2} + \frac{\partial^4}{\partial y^4} \tag{2.24}$$

Solving this differential equation for ψ generates the two dimensional stream function $\psi(x, y)$ for creeping Stokes flows in the desired coordinate system. In later sections of this chapter, I will briefly show these solutions for the sphere and prolate spheroid shapes. For more detailed information regarding the derivations, the reader is referred to (Happel and Brenner, 1991).

2.2.6 The Cone and Plate Rheometer

Currently, the cone and plate rheometer finds widespread use as a macroscale measurement standard. Named after its shape, the CAP rheometer takes advantage of small cone angles, φ , to apply a constant rate of shear, $\dot{\gamma}$, across the entire cone with surface area, A , approximated as

$$A \approx \pi R_{cap}^2 \tag{2.25}$$

where R_{cap} is the radius of the cone and the plate.

Turning the cone induces a shear stress, σ , or, inversely, applying a stress turns the cone and induces a shear strain, γ . The stress, defined physically as $\sigma = F/A$, is

applied through a torque, T , on the cone, making the stress in the CAP geometry equal to

$$\sigma = \frac{3T/2R_{cap}}{\pi R_{cap}^2} = \frac{3T}{2\pi R_{cap}^3} \quad (2.26)$$

Turning the cone from rest to an angle, θ , rotates each position in the surface by the arc length, $R_{cap}\theta$. The effective distance, h , between the cone and the plate is related to the cone angle by

$$h = R_{cap}\tan\varphi \quad (2.27)$$

which reduces by the small angle approximation to $h = R_{cap}\varphi$ for $\varphi \leq 4^\circ$. The shear strain is defined physically as

$$\gamma = \frac{\Delta x}{h} \quad (2.28)$$

where x denotes a displacement in one dimension. In the CAP geometry, this physical definition becomes

$$\gamma = \frac{\theta}{\varphi} \quad (2.29)$$

after factoring out R_{cap} . Similarly, the shear strain-rate is independent of R_{cap} , and depends on the natural frequency at which the cone rotates, ω as

$$\dot{\gamma} = \frac{\omega}{\varphi} \quad (2.30)$$

The resulting strain field is homogeneous, meaning that for any given height from the plate, the strain is constant across the entire cone. Sample sizes range from 100

μL to a milliliter or more. Applied stresses or strains often span several orders of magnitude, with an oscillatory limitation of < 100 Hz due to the imperfect and thus non-zero moment of inertia (Ferry, 1980; Macosko and Larson, 1994).

Two primary experimental modes are available with the macroscale CAP rheometer: *unidirectional* and *oscillatory*. For controlled-stress rheometry, the unidirectional mode is used in creep and flow experiments, where the primary result is a viscosity at one or more input stresses. The creep experiment is useful for direct examination of test material to a step stress. The flow experiment typically measures viscosity as a function of a stepped-series or even a ramp of input stresses or shear rates and provides insight into shear-thinning, one of the simplest nonlinear properties of non-Newtonian fluids. Procedurally, one can think of a flow measurement as a series of creep measurements where the viscosity estimate is taken from the constant, steady-state shear rate resulting from the input stress. For a Newtonian fluid, the creep test should result immediately in a constant shear rate when driven by a constant stress and satisfies the basic constitutive equation defined earlier as Equation 2.9. Any deviations from this expected behavior indicates that either the material is non-Newtonian or the instrument is not linear in the applied stresses for the tested regime (Ferry, 1980).

In contrast to unidirectional mode, oscillatory measurements in CAP rheometry involve rotating the cone in an oscillatory fashion, with an input of frequency or amplitude. The frequency dependence of viscoelastic materials uses the complex shear modulus, $G^*(\omega)$, which is a sum of the in-phase storage modulus, $G'(\omega)$, and the out-

of-phase loss modulus, $G''(\omega)$, i.e.

$$G^*(\omega) = G'(\omega) + iG''(\omega) \quad (2.31)$$

The complex modulus is related to the complex viscosity, $\eta^*(\omega)$ by the relationship

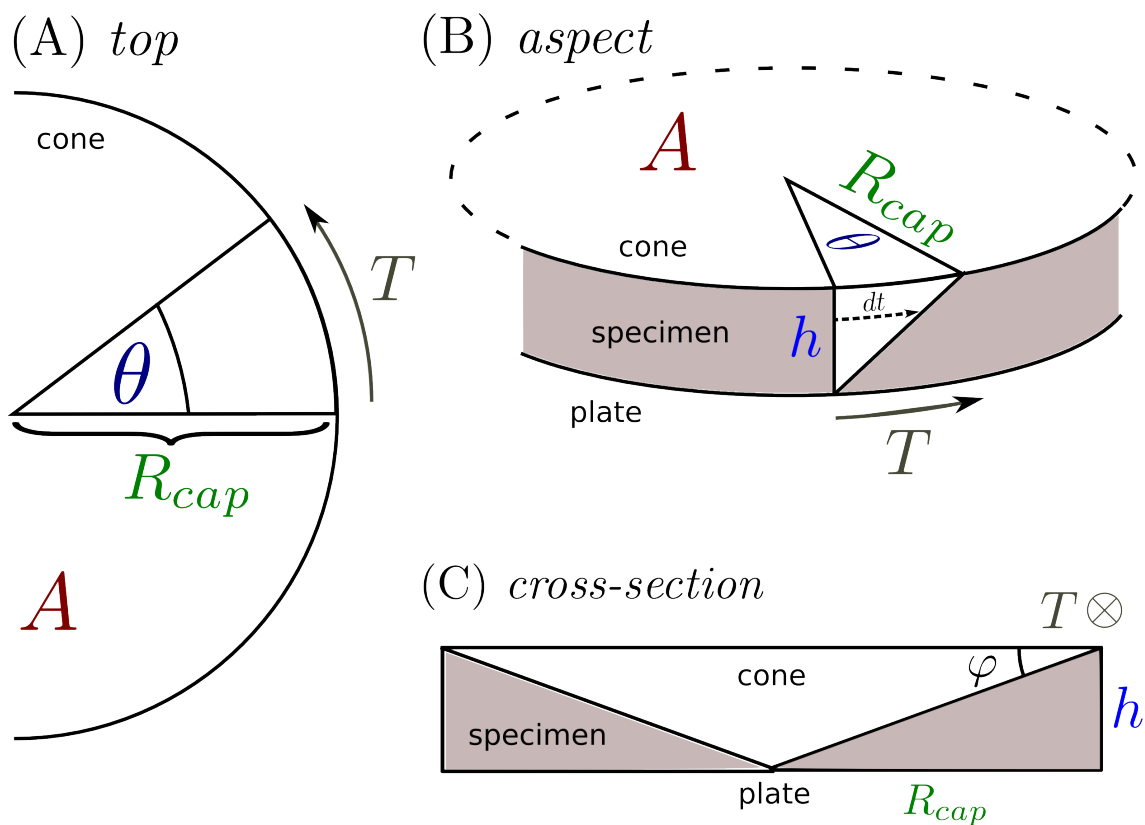
$$G^*(\omega) = -i\omega\eta^*(\omega) \quad (2.32)$$

where $\eta^*(\omega) = \eta'(\omega) - i\eta''(\omega)$, the real part of which is called the dissipative or real viscosity and the imaginary part, the elasticity.

2.2.7 Spherical Probe Geometry

2.2.7.1 Stokes Flow Field around Sphere

The velocity field, \vec{v} , around a sphere moving steadily through an unbounded Newtonian solution is one of the few geometries where an analytical solution for Equation 2.10 can be found. Given that the fluid flows past the sphere with a velocity in the \hat{z} -direction such that $\vec{v} = v\hat{z}$ as $r \rightarrow \infty$, and no-slip conditions exist at the boundary ($\vec{v}|_{\Omega} = 0$), we get the linear problem of Stokes flow around a sphere, where the flow equation is independent of coordinate systems, provided as Equation 2.12. We can reformulate the problem in terms of the dimensionless stream function (Eq. 2.19). We start with transforming Cartesian coordinates into spherical coordinates, which are



$$A \approx \pi R_{cap}^2 \quad h = R_{cap} \tan \varphi \approx R_{cap} \varphi$$

$$\sigma = \frac{F}{A} = \frac{3T}{2\pi R_{cap}^3}$$

$$\gamma = \frac{\Delta x}{h} = \frac{R_{cap} \theta}{R_{cap} \tan \varphi} \approx \frac{\theta}{\varphi}$$

$$\dot{\gamma} = \frac{d\gamma}{dt} = \frac{R_{cap} \omega}{R_{cap} \tan \varphi} \approx \frac{\omega}{\varphi}$$

Figure 2.1: The CAP rheometer makes use of its small cone angle to balance specimen strain across the entire cone surface, thus making it a homogeneous strain device. Shown in the figure are (A) top-down, (B) aspect, and (C) cross-sectional angles.

related through the equations

$$x = a \sin(\theta) \cos(\phi) \quad (2.33)$$

$$y = a \sin(\theta) \sin(\phi) \quad (2.34)$$

$$z = a \cos(\theta) \quad (2.35)$$

For axisymmetric flow, the operator ∇^2 is given by

$$\nabla^2 = \frac{d^2}{dr^2} - \frac{2}{r^2} \quad (2.36)$$

which generates the stream function

$$\psi(r, \theta) = \frac{v_d r_s^2}{4} \left[2 \left(\frac{r}{r_s} \right)^2 - \frac{3r}{r_s} + \frac{r_s}{r} \right] \sin^2 \theta \quad (2.37)$$

where the components of \vec{v} are given by

$$v_r = -v_d \cos \theta \left(1 - \frac{3r_s}{2r} + \frac{r_s^3}{2r^3} \right) \quad (2.38)$$

$$v_\theta = v_d \sin \theta \left(1 - \frac{3r_s}{4r} - \frac{r_s^3}{4r^3} \right) \quad (2.39)$$

where r_s is the sphere's radius, r is the radial location of the fluid moving with respect to the sphere, and θ is the angular location for the velocity in question ([Happel and Brenner, 1991](#)).

2.2.7.2 Stokes Drag Force on a Sphere

The fluid pressure, P against a sphere in laminar flow, moving in the direction of the unit vector \hat{v}_d , generates a drag force F_P , expressed as

$$F_P = \int_0^{2\pi} \int_0^\pi \vec{P} \cdot d\vec{A} \cdot \hat{v}_d \quad (2.40)$$

where the normal force against each surface area element of the sphere is integrated into a total force.

Drag forces due to shear stress applied by the incoming fluid upon the sphere is

$$F_\gamma = \int_0^{2\pi} \int_0^\pi \vec{\sigma}_\gamma \cdot \hat{v}_d \cdot dA \quad (2.41)$$

It follows that the total drag force is

$$\vec{F}_d = \vec{F}_P + \vec{F}_\gamma \quad (2.42)$$

Generally, the frictional Stokes drag force, F_d , on a particle under such conditions is

$$\vec{F}_d = \beta\eta\vec{v} \quad (2.43)$$

where \vec{v} is the particle velocity, η is the medium viscosity, and β is the geometry coefficient specific to the particle geometry (Happel and Brenner, 1991). This relation enables the determination of forces when particles are transported in a fluid of known

viscosity and vice-versa when the applied forces are well understood. In Newtonian fluids the medium viscosity is constant and particle motion lacks inertial effects because of the low Reynolds number ($Re < 10^{-4}$) conditions. Actuating particles under such conditions provides a convenient and simple method for computing the force on a particle when the effects of its geometry are known.

For a spherical geometry with radius r_s , the geometry coefficient β_s is simply

$$\beta_s = 6\pi r_s \quad (2.44)$$

When we substitute β_s into the generalized form of Equation 2.43, our result is the well-recognized form of Stokes equation on a sphere:

$$\vec{F} = 6\pi r_s \eta \vec{v}_s \quad (2.45)$$

where η is the dynamic viscosity of the fluid, and \vec{v}_s is the sphere velocity. A particle tracking algorithm measures particle velocity in a Newtonian fluid of known viscosity, allowing one to compute the force applied to the sphere.

2.2.7.3 Maximum Shear rate around Sphere

The strain rate tensor in spherical coordinates is

$$\dot{\gamma} = \begin{bmatrix} \frac{\partial v_r}{\partial r} & \frac{1}{2} \left(r \frac{\partial(v_\theta/r)}{\partial r} + \frac{1}{r} \frac{\partial v_r}{\partial \theta} \right) \\ \frac{1}{2} \left(r \frac{\partial(v_\theta/r)}{\partial r} + \frac{1}{r} \frac{\partial v_r}{\partial \theta} \right) & \frac{1}{r} \frac{\partial v_\theta}{\partial \theta} + \frac{v_r}{r} \end{bmatrix} \quad (2.46)$$

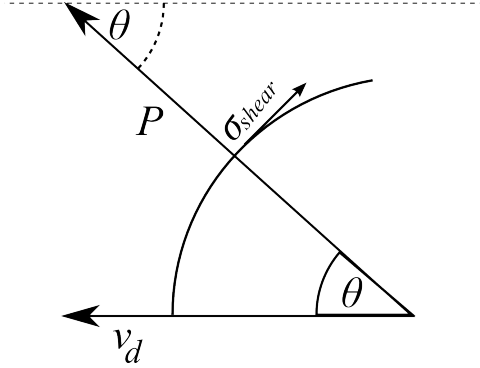


Figure 2.2: The fluid pressure against the sphere in laminar flow consists of normal and shear drag forces for each area element, where the integral across all area patches becomes the total force.

For the conversion of bead velocity to shear rate in a viscous fluid, we use the azimuthal velocity, v_θ , of the fluid with respect to the bead given earlier as Equation 2.39.

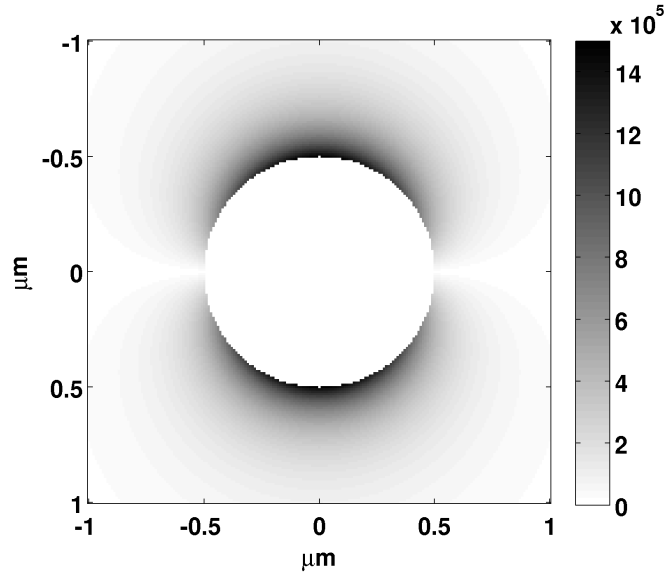


Figure 2.3: Shear rate imposed on fluid by bead

The maximum shear rate component of the strain rate tensor is found by differentiating v_θ with respect to r , setting $r = r_s$, and $\theta = \pi/2$. Taking the norm of the tensor

yields

$$\dot{\gamma}_{max} = \frac{3v_d}{\sqrt{2}r_s} \quad (2.47)$$

which agrees with results found in the literature.

2.2.8 Rod Probe Geometry

2.2.8.1 Stokes Flow around Rod (Prolate Spheroid)

Let us consider the case of a prolate spheroid in an unbounded fluid. Given that the fluid flows past the spheroid with a velocity \vec{v} in the z -direction and that we are sufficiently in the low Reynolds number regime so that we may disregard the inertial (nonlinear) term in the Navier-Stokes equation (Eq. 2.10), we get the linear problem of Stokes flow around a prolate spheroid.

Cartesian coordinates are related to prolate spheroidal coordinates through the equations

$$x = a \sinh(\xi) \sin(\theta) \cos(\phi) \quad (2.48)$$

$$y = a \sinh(\xi) \sin(\theta) \sin(\phi) \quad (2.49)$$

$$z = a \cosh(\xi) \cos(\theta) \quad (2.50)$$

Here we introduce the following transformation for convenience

$$\tau = \cosh(\xi) \quad (2.51)$$

$$\zeta = \cos(\theta) \quad (2.52)$$

In this basis, the operator ∇^2 is given by

$$\nabla^2 = \frac{1}{a(\tau^2 - \zeta^2)} \left[(\tau^2 - 1) \frac{\partial^2}{\partial \tau^2} + (1 - \zeta^2) \frac{\partial^2}{\partial \zeta^2} \right] \quad (2.53)$$

The velocity equations in terms of the stream functions are given by

$$v_\tau = \frac{1}{a\sqrt{(\tau^2 - \zeta^2)(\tau^2 - 1)}} \frac{\partial \psi}{\partial \zeta} \quad (2.54)$$

$$v_\zeta = \frac{1}{a\sqrt{(\tau^2 - \zeta^2)(1 - \zeta^2)}} \frac{\partial \psi}{\partial \tau} \quad (2.55)$$

The divergence condition is automatically satisfied by the above conditions and applying the no-slip and limiting case boundary conditions yields the well-known stream function for the case of a prolate spheroid ([Dassios et al., 1995](#)) as

$$\psi(\tau, \zeta) = \frac{a}{2} (\tau^2 - 1) (1 - \zeta^2) \left(1 - \frac{\frac{\tau_\alpha + 1}{\tau_\alpha - 1} \coth^{-1} \tau - \frac{\tau}{\tau^2 - 1}}{\frac{\tau_\alpha + 1}{\tau_\alpha - 1} \coth^{-1} \tau_\alpha - \frac{\tau_\alpha}{\tau_\alpha^2 - 1}} \right) \quad (2.56)$$

where τ_α is the value of τ at the surface of the spheroid. The velocity field is then given

by the equations

$$v_\tau = \frac{\zeta(-(\tau_\alpha - \tau)(1 + \tau_\alpha \tau) - (1 + \tau_\alpha^2)(\tau^2 - 1) \coth^{-1}(\tau_\alpha) + (1 + t^2)(\tau^2 - 1) \coth^{-1}(\tau))}{\sqrt{\zeta^2 - (1 + \zeta^2)\tau^2 + \tau^4(-\tau_\alpha + (1 + \tau_\alpha^2) \coth^{-1}(\tau_\alpha))}} \quad (2.57)$$

$$v_\zeta = \frac{\tau(\zeta^2 - 1)(\tau_\alpha(\tau_\alpha - \tau) + (1 + \tau_\alpha^2)(\coth^{-1} \tau_\alpha - \coth^{-1} \tau))}{\sqrt{(\zeta^2 - 1)(\zeta^2 - \tau^2)(-\tau_\alpha + (1 + \tau_\alpha^2) \coth^{-1} \tau_\alpha)}} \quad (2.58)$$

2.2.8.2 Stokes Drag Force on an Axially translating rod

Tirado, et al. approximated the geometry coefficient, β_c , for an axially translating cylindrical rod with an aspect ratio greater than 2 as

$$\beta_c = \frac{2\pi L}{\ln \frac{L}{2r_c} + \gamma_{\parallel}} \quad (2.59)$$

where r_c is the rod radius, L is the length of the rod, and γ_{\parallel} is equal to -0.19, as an end correction factor (Tirado and de la Torre, 1979).

2.2.8.3 Maximum Shear rate around Rod (Prolate Spheroid)

Equations 2.57 and 2.58 can be transformed back into the dimensional prolate spheroidal coordinates using the transforms given in Equation 2.52. The shear rate tensor, $\underline{\underline{\dot{\gamma}}}$, can then be calculated using the defined relationship in Equation 2.8 making its form in prolate spheroidal coordinates given by

$$\underline{\underline{\dot{\gamma}}} = \frac{1}{aM} \begin{pmatrix} \frac{\partial v_\xi}{\partial \xi} + \frac{v_\theta \cos(\theta) \sin(\theta)}{M^2} & \gamma_{shear} \\ \gamma_{shear} & \frac{\partial v_\theta}{\partial \theta} + \frac{v_\xi \cosh(\xi) \sinh(\xi)}{M^2} \end{pmatrix} \quad (2.60)$$

where the shear component expands to

$$\gamma_{shear} = \frac{1}{2} \left(\frac{\partial v_\xi}{\partial \theta} + \frac{\partial v_\theta}{\partial \xi} - \frac{U_\xi \cos(\theta) \sin(\theta)}{M^2} - \frac{U_\theta \cosh(\xi) \sinh(\xi)}{M^2} \right) \quad (2.61)$$

and $M = \sqrt{\sin^2 \theta \sinh^2 \xi}$. U_ξ and U_θ indicate coordinate specific components for the particle velocity.

Substituting in the appropriate equations into the tensor above and setting $\xi = \xi_\alpha$ and $\theta = \pi/2$ gives the maximum shear rate tensor at the top of the spheroid to be

$$\dot{\gamma}_{12} = \dot{\gamma}_{21} = \frac{\partial U}{a \sinh 2\xi_\alpha (-2 \cosh \xi_\alpha + (3 + \cosh 2\xi_\alpha) \coth^{-1}(\cosh \xi_\alpha))} \quad (2.62)$$

where ξ_α is the value of ξ at the surface of the spheroid. The shear rate magnitude at the surface of the prolate spheroid is then given by the equation

$$|\dot{\gamma}_{top}| = \frac{8\sqrt{2}U}{a \sinh 2\xi_\alpha (-2 \cosh \xi_\alpha + (3 + \cosh 2\xi_\alpha) \coth^{-1}(\cosh \xi_\alpha))} \quad (2.63)$$

where $\xi_\alpha = 1/2 [\ln(c+b) - \ln(c-b)]$ and $a = \sqrt{c^2 - b^2}$.

When the major axis, b of the prolate spheroid is much greater than its equatorial radius, c , the spheroid resembles a long, thin rod. For this limiting case the following

approximations can be made (Happel and Brenner, 1991):

$$\tau_\alpha \approx 1 + \frac{1}{2} \left(\frac{b}{c} \right)^2 \quad (2.64)$$

$$\coth^{-1} \tau_\alpha \approx \ln 2 + \ln \frac{c}{b} \quad (2.65)$$

$$a \approx c \quad (2.66)$$

Making the appropriate substitutions leads to an approximate expression for the shear rate at the top of a long rod

$$|\dot{\gamma}_{top}| = \frac{32c^5\sqrt{2}U}{(b^2 + 2c^2) \sqrt{c^{-4}(b^4 + 4b^2c^2)} (-2c^2(b^2 + 2c^2) + (b^4 + 4b^2c^2 + 8c^4)(\ln 2c - \ln b))} \quad (2.67)$$

This equation simplifies by defining $s = (b/c)^2$ to

$$|\dot{\gamma}_{top}| = \frac{64\sqrt{2}U}{(s + 2) \sqrt{s(4 + s)} (-8 + 16 \ln 2 + 2s(-2 + s \ln 2 + \ln 16) - (8 + s(4 + s)) \ln s)} \quad (2.68)$$

Using the fact that in this geometry, $s \ll 1$, and making the substitution $s = p^{-2}$ we can simplify the equation significantly to

$$|\dot{\gamma}_{top}| = \frac{2\sqrt{2}U}{b(-1 + \ln 4 - 2 \ln p)} \quad (2.69)$$

Equation 2.69 deviates from the exact solution by 0.5% at an aspect ratio of 15 and converges better for aspect ratios greater than 15. Later, in Chapter 5, I will use this shear rate equation to quantify shear thinning around a magnetically actuatable

rod-shaped particle.

2.3 Passive Microrheology

Microrheological measurements can be successfully subdivided into passive and active techniques. Passive microrheology measurements make use of the stochastic, thermal displacements of particles provided by the kT energy that serves as the background thermal fluctuations of molecular motion (Rubinstein and Colby, 2003), whereas active measurements use a deterministic, directed, and controlled force of known magnitude that drives the particles through the medium in a manner that belies the medium’s viscoelastic properties (Waigh, 2005).

In 1827 Robert Brown first documented the random motion of micron-sized particles in which he observed pollen grains “very evidently in motion ... [arising] neither from currents in the fluid, nor from its gradual evaporation” (Brown, 1828). Caused by a constant bombardment of solvent molecules, “Brownian motion” was not well understood and characterized fundamentally until Einstein began to tackle it during his *Annus Mirabilis* in 1905 (Stachel and Raman, 1990; Einstein, 1905).

Several experimental methods in the literature take advantage of particle diffusion to measure microrheology, some of which include Dynamic Light Scattering (DLS) (Maret and Wolf, 1987), Diffusing Wave Spectroscopy (DWS) (Pine et al., 1988; Mason and Weitz, 1995), Single Particle Tracking (SPT) (Mason et al., 1997), Multiple Particle Tracking (MPT) (Apgar et al., 2000), and two-particle microrheology (TPM) (Crocker

et al., 2000).

Developed first, DLS monitors time-dependent fluctuations from a molecular light scatterer and uses a detector such as a photomultiplier tube to record information about the particle size or surrounding solution viscosity. DWS, while based on DLS, does not share its single scatterer constraint. Both DLS and DWS offer rheology information across several orders of magnitude but only for solutions that are close to optically clear. Biological systems such as biopolymers or cell cultures become difficult to measure with these methods because they often contain scatterers of unknown size and/or shape (Gardel et al., 2005).

Passive, or thermal microbead rheology (TMBR) is an umbrella technique that estimates response functions for materials with a greater focus on those materials traditionally difficult to obtain in large quantities or for those with heterogeneities at small length scales. It can include single, multiple, and two particle methods. By using laser interferometric or video-based tracking techniques one can measure the displacement of spheres on the order of $1 \mu\text{m}$ in diameter to a few nanometers of resolution using only the thermal motion of the sphere as the driving force. By monitoring only the displacement of particles at constant temperature as a function of time, we can use mean-square displacement (MSD) and Generalized Stokes-Einstein Relation (GSER) methods to generate estimates of the viscoelastic response functions.

The remaining methods, single particle tracking (SPT), multiple particle tracking (MPT), and two-point microrheology (TPM) all use particle tracking methods in a video microscopy configuration. SPT monitors the displacement of single particles,

traditionally fluorophores or microspheres (Saxton and Jacobson, 1997), while MPT handles simultaneous tracking of many particles in the same field of view, treating each as a distinct, isolated particle (Apgar et al., 2000). Particle tracking methods are more sensitive to heterogeneous materials, generating wide variances in the results that macroscale rheometry methods such as CAP would otherwise average across its vast contact area (Schmidt et al., 2000). While this is a limitation when trying to generate data comparable to CAP but with a much smaller specimen, it can also be considered an advantage when one wants to sample the heterogeneity in a material such as mucus for a given length scale.

Generally, the characterized length and time scales must be relevant to the phenomenon of interest. A variant on multiple particle tracking (MPT) is two particle microrheology (TPM), which uses the correlated motion between pairs of particles. TPM recovers and reproduces macroscale results more faithfully because the probed length scales become the intervening distances between particles and not the sizes of the particles themselves (Crocker et al., 2000).

Random walks are used to describe many of these stochastic processes. Molecules diffusing in solvent codify the lower bound on the rate at which chemical reactions take place. The diffusion rate for any particle in solution is described by the Stokes-Einstein relation, (Eq. 2.73), which depends on the temperature of the solution and the viscous drag the solution imparts on the particle's motion. (Berg, 1993).

The root-mean-square displacement, $\langle r \rangle = \sqrt{\langle r^2 \rangle}$, defines a characteristic length scale for a diffusing particle with radius a and is a relationship that functions at every

observational time and length scale, a consequence of the fractal nature of stochastic processes and the ergodic theorem. The mean-squared displacement (MSD), $\langle r^2 \rangle$, of a diffusing particle in a Newtonian fluid will vary in time according to the statistics of a random walk,

$$\langle r^2 \rangle = 2dD\tau \quad (2.70)$$

where d defines the dimensionality of the *observed* process ($d = 2$ for either diffusion in two dimensions or for the two-dimensional projection of diffusion in three dimensions, such as that measured by a camera). D is the diffusion coefficient, and τ describes a window of time, or period of duration (Rubinstein and Colby, 2003).

Raw position data of diffusing particles as a function of time are used to compute the MSD across varying τ by

$$\Delta \bar{r}^2(\tau) = (N - \tau) \sum_{k=\tau}^{N-\tau} (r_{k+\tau} - r_k)^2 \quad (2.71)$$

where r_k defines the position of the particle by

$$r_k = \sqrt{(x_k - x_o)^2 + (y_k - y_o)^2} \quad (2.72)$$

Einstein described the diffusion coefficient in a general form, i.e.

$$D = kT/\zeta \quad (2.73)$$

where ζ is a quantity that defines the Stokes drag interaction between a solvent with viscosity, η , and a diffusing particle's size and shape (Einstein, 1905). For a diffusing sphere with radius, a , $\zeta_s = 6\pi a\eta$, the the specific diffusion coefficient is

$$D = \frac{kT}{6\pi\eta a} \quad (2.74)$$

commonly called the Stokes-Einstein relation (Rubinstein and Colby, 2003). Expanded, this makes the MSD equation,

$$\langle r^2 \rangle = \frac{2dkT\tau}{6\pi\eta a} \quad (2.75)$$

It is important to notice that this equation describes an averaged, statistical value for $\langle r^2 \rangle$ in a Newtonian fluid, as is the case when a single particle is monitored for an extended period of time, or when a large number of particles are tracked and their squared displacements averaged together. The MSD will be a linear function of τ , and the average displacement will be zero (Rubinstein and Colby, 2003). Because of its linear dependence on τ shown in Equation 2.75, the MSD as a function of τ for a Newtonian fluid will have a slope equal to one in log space. When the test material is viscoelastic this slope will decrease to < 1 for some time scales and for purely elastic materials the slope would decrease even further to equal zero for all time scales (Fig. 2.4).

In 1995 Mason and Weitz proposed a generalized Stokes-Einstein relation (GSER) that extracted linear viscoelastic moduli for DLS (Mason and Weitz, 1995). By 2000

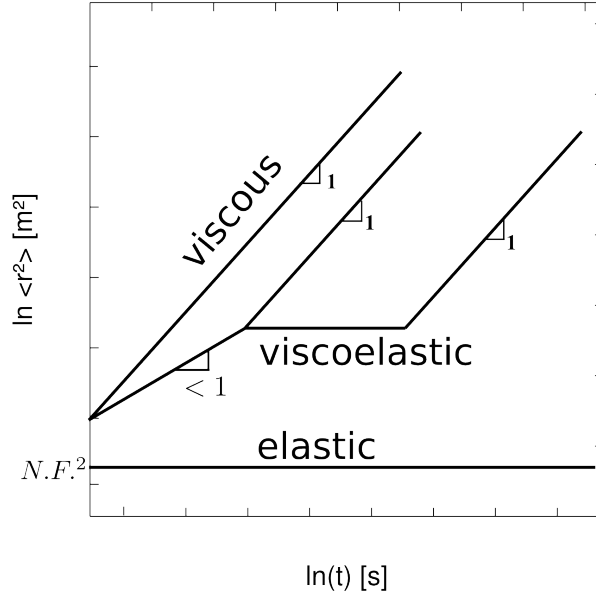


Figure 2.4: Expected MSD power laws for spheres diffusing in viscous, viscoelastic, and elastic materials

the technique had spread to cover single and multiple particle tracking (Mason, 2000). Briefly, the GSER generalizes the Stokes-Einstein relation by making the diffusion coefficient, D , a function of complex frequency which propagates into the complex shear modulus, $G^*(\omega)$,

$$G^*(\omega) = \frac{kT}{6\pi a D^*(\omega)} \quad (2.76)$$

where $D^*(\omega)$ is a frequency-dependent complex diffusion function. Mason estimates the transform from the time to the frequency domain first with a power law expansion about the frequency, ω

$$\langle \Delta r^2(t) \rangle \approx \langle \Delta r^2(1/\omega) \rangle (\omega t)^{\alpha(\omega)} \quad (2.77)$$

where $\alpha(\omega)$ is the power-law slope, defined by Mason as

$$\alpha(\omega) \equiv \frac{d \ln \langle \Delta r^2(t) \rangle}{d \ln t} \quad (2.78)$$

evaluated with $t = 1/\omega$. The Fourier transform for the power law is approximately

$$i\omega \mathcal{F} \{ \langle \Delta r^2(t) \rangle \} \approx \langle \Delta r^2(1/\omega) \rangle \Gamma[1 + \alpha(\omega)] \cdot i^{-\alpha(\omega)} \quad (2.79)$$

where the well-known gamma function is $\Gamma(x) = \int_0^\infty t^{(x-1)} e^{-t} dt$ (Mason, 2000; Greenberg, 1998). Finally, the complex shear modulus, $G^*(\omega) = G'(\omega) + iG''(\omega)$ with its components equal to

$$G'(\omega) = |G^*(\omega)| \cos(\pi\alpha(\omega)/2) \quad (2.80)$$

$$G''(\omega) = |G^*(\omega)| \sin(\pi\alpha(\omega)/2) \quad (2.81)$$

and its scalar magnitude equal to

$$|G^*(\omega)| = \frac{kT}{\pi a \langle \Delta r^2(1/\omega) \rangle \Gamma[1 + \alpha(\omega)]} \quad (2.82)$$

A consequence of this methodology extends the slope from only the diffusive range with $\alpha(\omega) = 1$ across all time scales down to $\alpha = 0$ corresponding to a material that is completely elastic (Gardel et al., 2005). The limits for each of these slopes, their terminal values in both displacement and time scales are all predictable according to

polymer physics models such as the Doi-Edwards tube model of polymer reptation (Rubinstein and Colby, 2003).

In summary, by tracing particle paths in the material, the GSER provides an adequate estimate for frequency-dependent relationships between the viscous and elastic moduli for a given material without the large amount of material that macroscale measurements such as CAP require. However, because the nature of the process is stochastic, large numbers of particles must be tracked, and because of the linear relationship between $D^*(\omega)$ and $\langle r^2 \rangle$, the method is limited to the linear viscoelastic regime. Size-dependence properties which may be inherent in the material are measurable by this method but is limited when one wants to make large length scale measurements. Even with these precautions the GSER can have artifacts at extremes of frequency due to data truncation (Mason, 2000).

2.4 Active microrheology

Unlike passive microrheology, active microrheology techniques can be divided into methods where the measuring probe is attached to the host instrumentation and into those with detached probes (Fisher et al., 2006b). Systems with attached probes typically use different types of deflection technologies. Earlier systems used microneedles or glass fibers to measure the effects of forces on chromosome movement (Kishino and Yanagida, 1988; Schmitz et al., 2000) and those of myosin on actin (Skibbens and Salmon, 1997). More recent methods like atomic force microscopy (AFM) still use ba-

sic cantilever deflection but with exceptional spatial and force resolution (Florin et al., 1998). The primary disadvantage of these methods for living biological systems lies in their invasiveness; measuring subcellular elements inherently destroys the system of interest.

Systems with detached probes typically use optical or magnetic forces to control the position and velocity of a microscopic probe particle. The probe, typically a microsphere, is often made of polystyrene and, if magnetic, is also embedded with enough ferrous material to make it superparamagnetic. The probe is free to diffuse or directly move throughout the volume and sample its environment. Its position provides information in time regarding the rheological parameters of its surroundings. Optical tweezers systems use a high-powered laser to interact with a probe of different refractive index than the background solvent to generate sufficient optical force to maintain a trap, or energy well, in which the probe inhabits (Ashkin and Dziedzic, 1987). In addition to being force-limited to ≤ 200 pN, optical tweezers suffer from specimen heating (Peterman et al., 2003; Mao et al., 2005) and lack specificity with regard to probes located in the sample space. Sub-cellular organelles will migrate to the center of an optical trap provided the objects refract with respect to the background solvent. In spite of these shortcomings, optical traps have managed rousing success with measurements of transcription forces (Yin et al., 1995) as well as forces generated by molecular motors (Block et al., 1990; Hirakawa et al., 2000; Kuo and Sheetz, 1993; Mao et al., 2005; Peterman et al., 2003).

Contrasting the optical trap, magnetic tweezers systems like the 3DFM offer probe

specificity, do not appreciably heat the specimen, and offer forces greater than 10 nN on 4.5 μm and close to 1 nN on 1 μm sized beads (Fisher et al., 2006a). Early magnetorheometry systems offered even higher forces but with the caveat of larger probes that limited frequency response because of inertial effects. Even so, many experiments successfully measured rheological properties for canine mucus (King and Macklem, 1977). More recently, similar systems with smaller probes measured the viscoelastic properties of cell membranes (Bausch et al., 1998; Feneberg et al., 2004; de Morales et al., 2001), actin (Amblard et al., 1996a; Schmidt et al., 2000; Uhde et al., 2005a; Uhde et al., 2005b), as well as hyaluronan and sputum (Parkin et al., 2006; O'Brien et al., 2008).

Aside from thermal motion, all biological systems move in some fashion at some length and time scales, whether it involves a cheetah running at 70 mph, the incremental growth of the mighty sequoia, or an ATP synthase lodged on the cell membrane's surface cranking out new ATP. The motion in biological systems ties them inextricably to the other scientific discipline concerned on a fundamental level with motion, i.e. physics. Using a form of Newton's laws of motion we find the displacement, x , velocity, v , and acceleration, a , of an object depend on the force applied to it, F_{ext} , as well as the object's mass, m , and friction, f_v , and spring constant, k , between the object and its environment

$$F_{ext} - f_v v - kx = ma \tag{2.83}$$

. With this relationship, we realize that to draw conclusions regarding the physics of

a biological system, our fundamental measurements would need to quantify forces and displacements, in addition to keeping track of the passage of time.

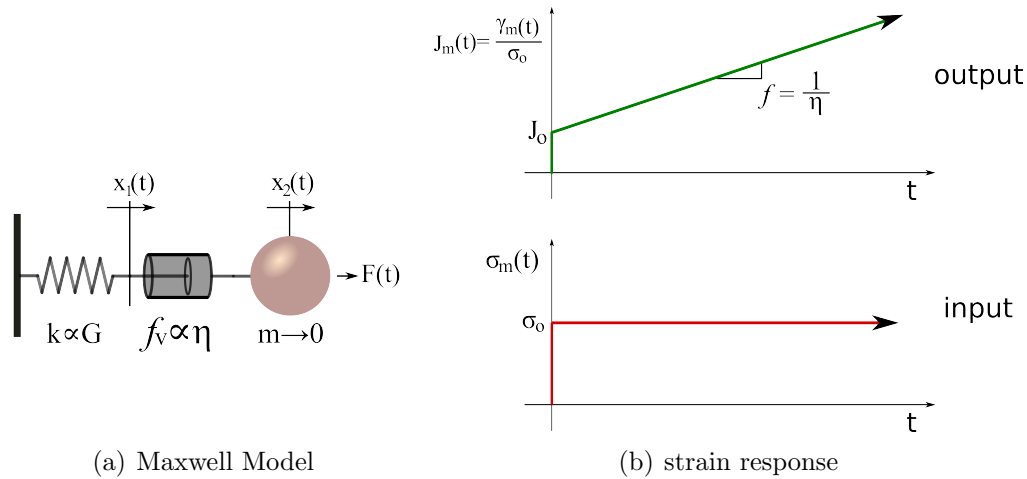


Figure 2.5: The Maxwell model and its strain response

Here, we concern ourselves with the biophysics at microscopic length scales along with relatively fast time scales. Motion at this scale is highly overdamped, as shown by the dimensionless Reynolds Number (Re) defined in Equation 2.11. Re is sufficiently low ($Re < 10^{-2}$) for all experiments discussed in this work, such that the inertial effects are vanishingly small (Purcell, 1977), which reduces Eq. 2.83 to

$$F = f_v v + kx \quad (2.84)$$

This equation has been used to describe the motion of many different types of overdamped objects, including macroscale Kelvin-Voight viscoelastic materials (Ferry, 1980) and, at micron-sized length scales, bacteria. A relative measure that is an apparent favorite among researchers computes the “coasting” distance of a bacterium devoid

of motor activity; because the bacterium travels through a highly overdamped system, the coasting distance is much smaller than even the size of the water (solvent) molecules (Berg, 1993; Howard, 2001)!

In viscoelastic systems, f_v in Eq. 2.84 is due to the viscosity, η , (Figure 2.5) experienced by some component in the system while k correlates with the elastic modulus, G , of the system. The viscosity is acquired by solving Stokes flow for a sphere for η

$$\eta = \frac{F}{6\pi r_s v(t)} \quad (2.85)$$

while computing the shear modulus requires computing the compliance J first,

$$J = 1/G = \frac{6\pi r_s x(t)}{F} \quad (2.86)$$

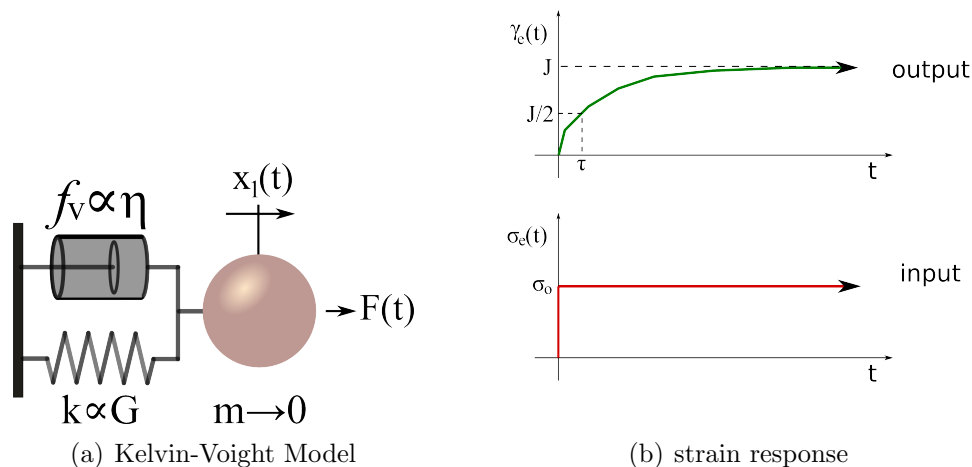


Figure 2.6: Kelvin-Voigt Model: the viscoelastic solid and its strain response

Measuring the microrheology of biological materials with active techniques began

early in the 1920s with the manipulation of iron filings (Gardel et al., 2005). Probably most notable of the early work with magnetics was Crick’s experiments with cytoplasm in 1949, in which he measured the viscoelastic parameters of cytoplasm *in vitro*. (Crick and Hughes, 1949).

Measurements of linear viscoelastic materials with DMBR can be modeled easily with canonical mechanical models. For instance, for a Newtonian fluid the expected response of a sphere to a step force input would reduce to Stokes Law (Eq. 2.45).

The Jeffrey model, shown in Figure 2.7 with its step response, captures behavior typically seen in a viscoelastic liquid. The η_0 damper accesses viscous-only modes of the material. The stress-controlled step response, $J(t)$ is

$$J(t) = \frac{1}{G} + \frac{t}{\eta_0} - \frac{1}{G} \exp\left(\frac{-Gt}{\eta_1}\right) \quad (2.87)$$

The steady-state, zero-shear viscosity is extracted from the slope of the test material’s step response while the modulus, G , can be estimated from the projected intercept (Maxwell model approximation).

2.4.1 Magnetic Force on a Spherical Particle

To describe the magnetic driving forces, \vec{F}_m , applied to spherical and cylindrical particles in these studies we start with

$$\vec{F}_m = \left(\vec{m}_{eff} \cdot \vec{\nabla}\right) \vec{B} \quad (2.88)$$

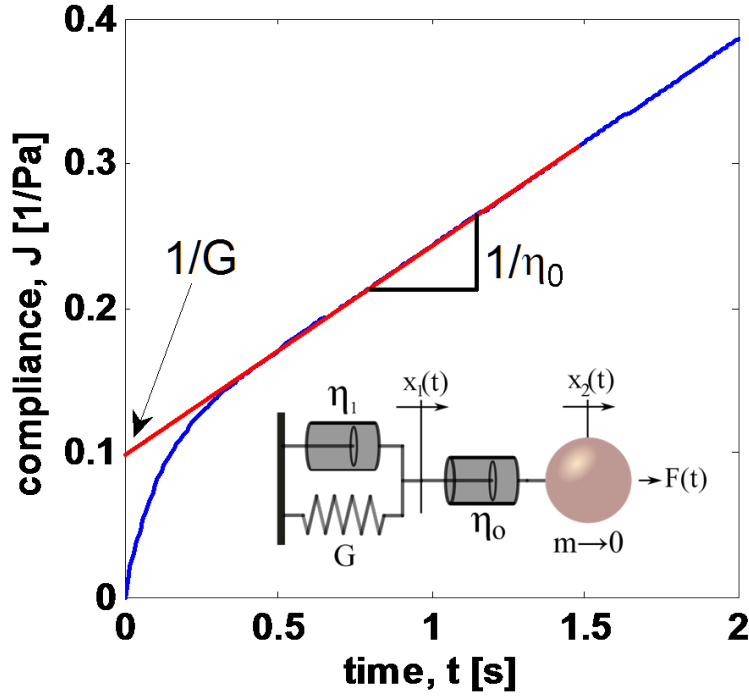


Figure 2.7: The Jeffrey model: strain response to input stress

where the effective magnetization of the particles \vec{m}_{eff} is a function of the magnetic induction \vec{B} and the magnetic properties of the particles. In addition to \vec{m}_{eff} , \vec{F}_m is a function of $\vec{\nabla}B$. Under the conditions of these experiments, the applied force, \vec{F}_m is

$$\vec{F}_m = \chi B \cdot \nabla B \quad (2.89)$$

In addition, particle shape affects the magnetic force sensed by the particle from a given source. This occurs because of the changes in magnitude of the magnetizing force, H , with respect to particle orientation. Isotropic particles, like the sphere, have equal demagnetization factors for all degrees of freedom and thus show no preference or optimization along any one given axis (Osborn, 1945).

We previously described the force applied to a magnetic bead in a magnetophoretic system in Fisher, et al. To summarize here, the force on a soft, magnetically permeable, and unsaturated sphere, F_s , is

$$F_s = \frac{\pi d^3}{4\mu_0} \left(\frac{\mu_r - 1}{\mu_r + 2} \right) \nabla(B \cdot B) \quad (2.90)$$

where d is the bead diameter, μ_0 is the permeability of free space in SI units. We use the standard definition of relative permeability, μ_r , as $\mu_r = \mu/\mu_0$, and is the ratio of the material permeability to the permeability of free space. Finally, $\nabla(B \cdot B)$ is the incident magnetic field and field gradient, indicating, for a permanent drive magnet, a dependence on its material properties as well as its shape (Fisher et al., 2006a).

We can rewrite the relation in Equation 2.90 that defines the magnetic force on a sphere as

$$F_s = \frac{(\mu_r - 1)}{2\mu_0} \cdot \frac{3}{8(\mu_r + 2)} \cdot V_s \cdot \nabla(B^2) \quad (2.91)$$

where V_s and μ_r are the volume and the relative permeability of the sphere, respectively (Meehan, 2007).

2.4.2 Magnetic Force on a Rod-shaped Particle

From (Osborn, 1945), the magnetization of an ellipsoid in the i th direction is

$$M_i = \frac{H_{0,i}}{N_i - \frac{1}{\chi_0}} \quad (2.92)$$

where H is the applied field, N is the demagnetization factor, and χ is its susceptibility.

By rewriting this equation in terms of SI units, and dropping the subscript, we get

$$M = \frac{1}{\mu_0} \cdot \frac{B}{N - \frac{1}{\chi}} \quad (2.93)$$

Replacing χ with μ by $\mu = \mu_0(1 + \chi)$:

$$M = \frac{1}{\mu_0} \cdot \frac{B}{N - \frac{\mu_0}{\mu - \mu_0}} \quad (2.94)$$

Then, according to Osborn, the demagnetization factor, N , along the length of a sufficient aspect ratio ellipsoid is zero, resulting in magnetization per unit volume, M , of

$$M = \frac{B}{\mu_0} (\mu_r - 1) \quad (2.95)$$

where μ_r is the relative permeability of the magnetic material. For the magnetic moment, m , we simply multiply M by the volume of a cylinder, $V_c = \pi r_c^2 L$, to get

$$m = \frac{\pi r_c^2 L}{\mu_0} (\mu_r - 1) B \quad (2.96)$$

Finally, by substituting equation 2.96 into equation 2.88 we approximate the force applied to a cylinder in the axial direction as

$$F_c = \frac{\pi r_c^2 L}{2\mu_0} (\mu_r - 1) \nabla(B^2) \quad (2.97)$$

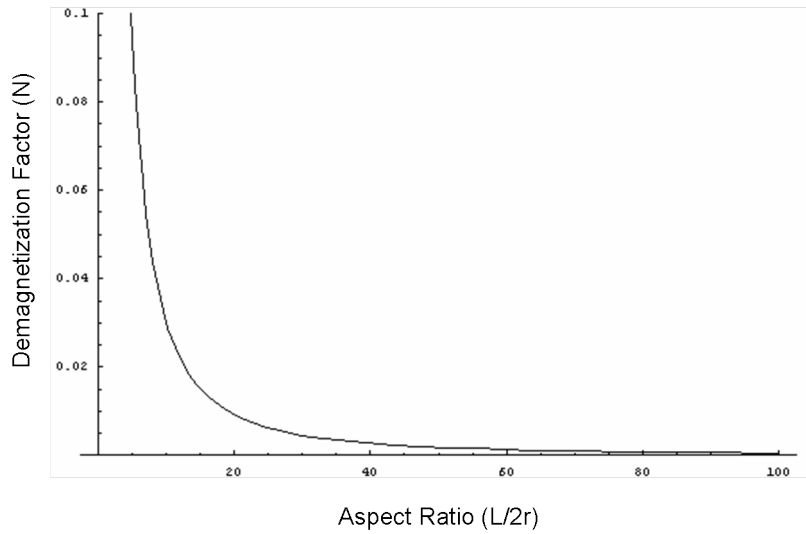


Figure 2.8: Effect of aspect ratio on demagnetization factor

Because Equation 2.97 is an approximation of the force on a cylinder as a prolate ellipsoid, we must establish the constraints concerning the allowable aspect ratios for our cylindrical particles. When we plot the effect of aspect ratio on the demagnetization factor computed by Osborn and shown in Figure 2.8, we can conclude that particles with an aspect ratio greater than 20 contributes minimal error in the computed force in the axial direction (Osborn, 1945).

We can now rewrite equation 2.97 the force exerted on a cylinder, F_c , as

$$F_c = \frac{(\mu_r - 1)}{2\mu_0} \cdot V_c \cdot \nabla (B^2) \quad (2.98)$$

where V_c is the volume of a cylinder and μ_r is the relative permeability of the magnetic material (Osborn, 1945).

Under low Reynolds number ($Re \ll 1$) conditions, the driven particle transport

described above enables the correlation of magnetic driving forces, particle geometries, and velocities in any Newtonian fluid through Stokes Law. We compared these empirical magnetophoretic forces with predicted values based on independently measured magnetic characteristics of the system. Due to the low Reynolds number conditions, we set F_m equal to the magnitude of the frictional drag force on the particle, F_d .

2.5 Conclusions

In this chapter I reviewed the Navier-Stokes equation and showed how it arises from basic fluid mechanics principles. I showed how NS can be used to estimate the maximum shear rate imparted on the fluid by two simple particle geometries. I reviewed the literature and illustrated the basic principles of both thermal and active microbead rheology.

Chapter 3

The 3DFM as a microrheometer

3.1 Overview

The three-dimensional force microscope (3DFM) provides a wide variety of testing modalities for small volumes of soft viscoelastic specimens at nanometer length scales. Video, magnetic, and interferometric tracking subsystems comprise its general framework. Here we explain how these subsystems are used together to perform new experiments in microrheology and provide knowledge regarding heretofore unknown phenomena in biopolymer systems.

I briefly introduced microrheology methods in Chapter 2. Here I begin with a description of our methods of sample preparation for both thermal and driven-bead microrheology experiments which include neutralizing bead polymer interactions as well as methods for distributing particles into thick or highly viscoelastic materials. Following, I define the components and capabilities for the video and tracking subsystems, thus defining error in position for the video-based technique and compare it to our high resolution 3D laser interferometric tracking subsystem. Next, I describe the

magnetics subsystem for the 3DFM, taking care to elaborate in detail the calibration techniques I use to provide a complete force map as a function of both distance and drive current. Finally, I combine these subsystems to define useful force ranges and to predict the forces required to make effective measurements of viscoelasticity with the 3DFM.

3.2 Methods

3.2.1 Sample Preparation

For either thermal or driven microbead rheology techniques, a “specimen” is defined as a volume of some viscous or viscoelastic material as small as $10 - 20 \mu\text{L}$ through which are distributed microparticles that can be fluorescent, magnetic, surface-coated, or any combination thereof (see Figure 3.2a). A smaller volume ($1 - 2 \mu\text{L}$) is ultimately placed into a “sandwich” of coverslips measuring $24 \times 40 \text{ mm}$ with $100 \mu\text{m}$ (No. 0) or $175 \mu\text{m}$ (No. $1\frac{1}{2}$) thickness (Fig. 3.10). If using driven microbead rheology (DMBR), the coverslip sandwich includes a magnetically permeable pole tip, calibrated for forces.

Before making a finished sample, one must control for experimental conditions. The surface fictionalization of the bead can affect the microrheology measurement through bead interactions with the polymer in the sample. We compensate for these interactions by PEGylating the bead surface thus neutralizing the charge.

3.2.2 Bead PEGylation

PEGylating particles involves attaching polyethylene glycol (PEG) molecules with appropriate chemical modification to beads with complimentary surface modification. In short, the reaction utilizes common EDAC chemistry, where EDAC (linker) and NHS (stabilizer) are used to react and attach PEG to the probe surface. The resulting PEG coated surface reduces the surface charge and thus the adhesion of the probes to the materials in which they are embedded.

We use the method found in (Lai et al., 2007) to PEGylate our probes because interactions between the particles and their environment may cause unwanted artifacts in the determination of solution material properties/rheology. To test the efficacy of our PEGylated beads, we measured the zeta potential of the beads before and after the PEGylation process, looking for a significant drop in the magnitude of the surface charge. Specifics for the protocol are located in Appendix A.2.

3.2.3 Distributing beads into a sample

A critical step in measuring the microrheology of any soft material involves the distribution of the probe particles in the material of interest. For materials like DNA or mucus, vortexing the sample, or subjecting the sample to large amounts of repeated shearing can cause irreversible damage to the viscoelastic network. I first tried evaporating test particles onto a cover slip and then raked the sample through the dried bead field, a method unsuccessful due to rapid evaporation of water (solvent) from the specimen. Because this did not work we devised a method that achieved a good number

of beads, evenly distributed throughout the test material, provided the material was pipettable.

To summarize the approach, we place a small amount of bead solution, where the beads are highly concentrated, into the tip of a clean pipette (Fig. 3.1a). The pipette tip is placed in an oven at 80 °C and the buffer surrounding the beads is allowed to dry. The beads become lightly associated with the pipette surface (Fig. 3.1b). Once the tip is dry and cooled to room temperature, the specimen of interest is pulled into the pipette, applying a shear stress of sufficient magnitude to dislodge the beads and disperse them through the specimen (Fig. 3.1c). Delivering the payload inside the pipette to a new container ensures even better mixing. The pipette tips remain viable for 1–2 days in the oven at 80 °C. Storage at cooler temperatures is not advised unless done under dry conditions. As a general note, this method only works well with PEGylated beads. When performed with non-PEG coated beads, a substantial number of large aggregates form inside the rheology sample. For more detail, the protocol is located in Appendix A.3.

3.2.4 Boundary Effects

Experimental conditions for microrheology studies in the 3DFM are subject to two types of boundary effects. “End” effects refer to the change in the expected velocity of a bead as it directly approaches and collides with a wall (See Fig. 3.2(a) for schematic). Knowing when this effect becomes substantial is important especially in the case of our

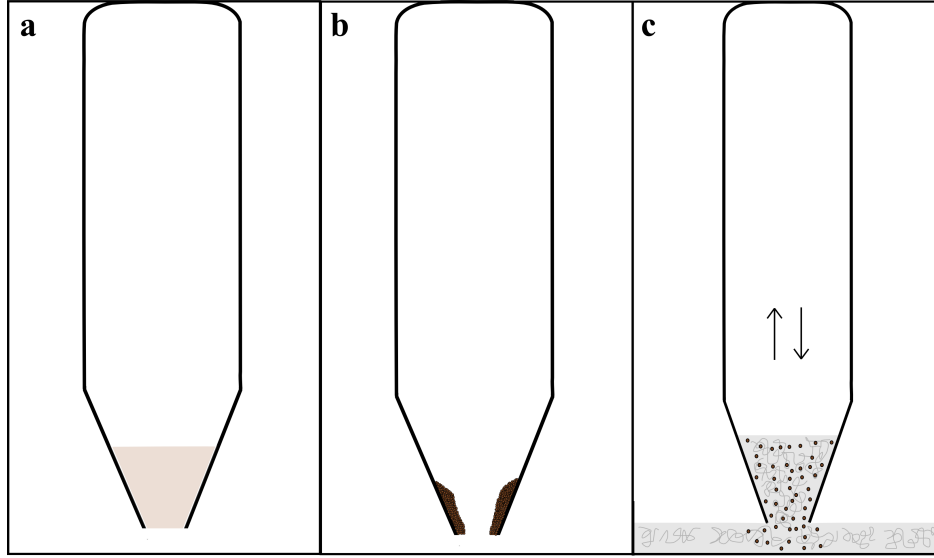


Figure 3.1: a. A 200 μL pipette tip is filled with about 10 μL of 5:1 EtOH:Bead solution. The solution is allowed to dry at 80°Celsius. b. After the 1 μm or 2.8 μm PEGylated beads have dried on the surface of the pipette tip, the beads are dispersed in the sample when this tip is used for transport. c. When the sample is pipetted up and down, the beads are dispersed. The sample is now ready for microbead experiments without having been destroyed.

DMBR experiments because the beads translate towards and directly into the pole tip. Assuming the pole tip is a large, flat wall compared to the bead size, we can account for these end effects by scaling the expected Stokes force, $F_{Stokes} = 6\pi a\eta v$, to a new apparent force “felt” by the bead, F_{end}

$$F_{end} = F_{Stokes} \left(1 + \frac{1.145a}{W_1} + \frac{3a^2}{W_1^2} \right) \left(1 + \frac{1.145a}{W_2} + \frac{3a^2}{W_2^2} \right) \quad (3.1)$$

where W_1 and W_2 are the distances from the bead to the approaching wall and its spatial opposite (King and Macklem, 1977). The typical distance between the pole tip and the flat opposing piece of μ -metal is approximately 550 μm . Any bead in a typical field of view that contains the pole tip will be more than 450 μm from the flat. This

vast distance allows us to ignore the W_2 term as insignificant, resulting in a correction factor of

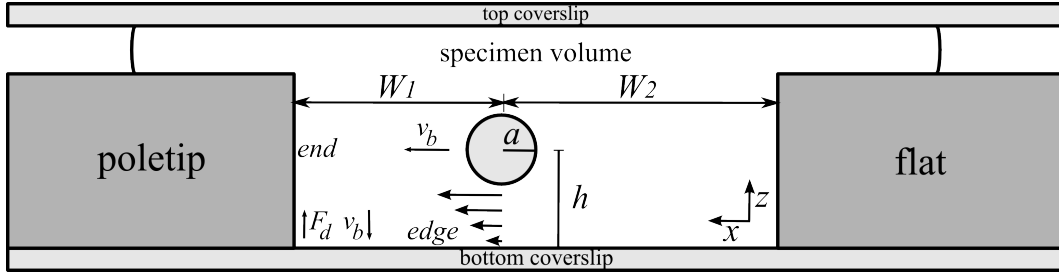
$$F_{end} = F_{Stokes} \left(1 + \frac{1.145a}{W_1} + \frac{3a^2}{W_1^2} \right) \quad (3.2)$$

where W_1 is the distance of the bead from the pole tip surface. Plotting this correction factor results in Figure 3.2(b)

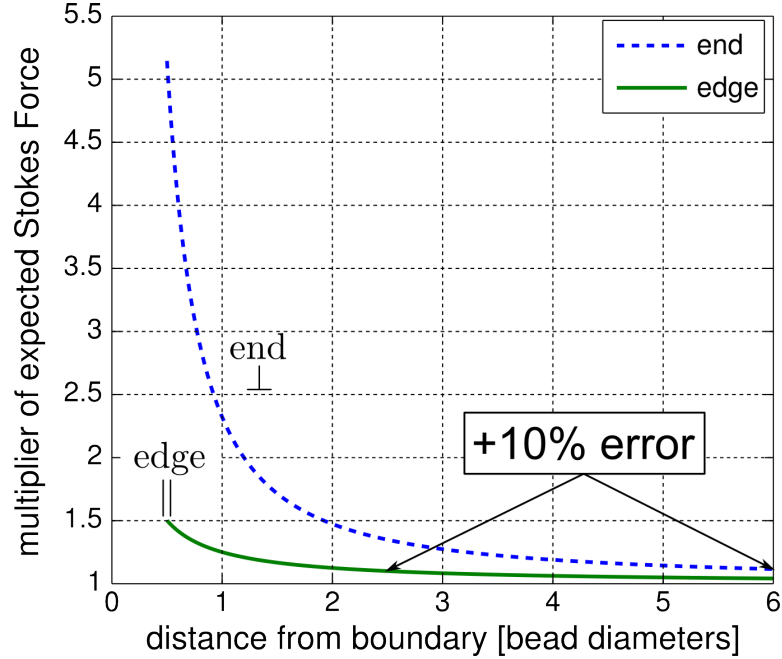
Edge effects where the bead translates in a direction parallel to a close surface make use of the Faxén correction to account for the additional drag (Ferry, 1980):

$$F_{Faxen} = F_{Stokes} \left(1 - \frac{9}{16} \left(\frac{a}{h} \right) + \frac{1}{8} \left(\frac{a}{h} \right)^3 - \frac{45}{256} \left(\frac{a}{h} \right)^4 - \frac{1}{16} \left(\frac{a}{h} \right)^5 \right)^{-1} \quad (3.3)$$

According to these relationships, end effects will cause a 10% systematic error at a distance of 6 bead diameters away while edge effects will cause a similar systematic bias when the bead is 2.5 diameters from the bottom coverslip surface. These biases are easily avoided by choosing beads that are more central to the specimen volume. It is important to note that these corrections are only true for a Newtonian fluid. When moving about in a material with a more complex rheology, these equations provide a limiting and optimistic estimate.



(a) Cross-section of Specimen Chamber



(b) End & Edge Effects

Figure 3.2: In 3.2(a) is a cross-section through the specimen chamber with the $+z$ direction pointed upwards. The bottom coverslip serves as the edge boundary, contributing to drag when the bead is too close. The pole tip defines another boundary as the bead travels towards it, called here an “end”. Both boundaries affect the force required to maintain a constant velocity. Both curves in 3.2(b) illustrate the change in the magnitude for this necessary force. The distance on the x -axis is a measure of bead diameters from the boundary edge to the center of the bead.

3.3 Video Subsystem

Traditional microrheology techniques use either a laser interferometry or a video tracking setup. Laser interferometry uses the incident beam of a laser to generate a

diffraction pattern when a bead is placed in the light path. The diffraction pattern is cast onto a quadrant photodiode and the resulting signals indicate particle motion. The higher bandwidth of laser interferometry can provide information about the microrheology of materials at higher decades of frequency.

While particle tracking using laser interferometry is satisfying because of its high bandwidth and its ability to track particles in three dimensions, tracking with video frames has distinct advantages with regard to microrheology experiments— tracking several to many particles simultaneously, sensitivity to spatial heterogeneity within the field of view, and the benefit of visual context. To that end, we used a fast frame rate camera (120 – 300 Hz), a frame grabber board, and custom-build video capture software as the constituent elements of the 3DFM video subsystem.

The fast frame camera in the 3DFM is a Jai-Pulnix, model PTM-6710CL (www.jaipulnix.com) which can capture full 8-bit progressive-scan frames with 648×484 pixel resolution at 120 frames per second (fps) and smaller regions of interest (100×100 pixels) at 300 fps. At full spatial resolution each frame is 306 kilobytes in size and each minute of video at full frame rate generates over 2 GB of data that must be transferred to disk in real-time due to a lack of on-camera RAM. The camera connects to the frame-grabber board via a CameraLink interface that boasts data transfer rates of 260 MB per second. When this camera is added to the optical path of our microscope (model TE-2000-E, Nikon Instruments, Melville, NY), and is used to image a field of view with a $60\times$ water-immersion objective, the length calibration is $0.152 \mu\text{m}$ per pixel, making

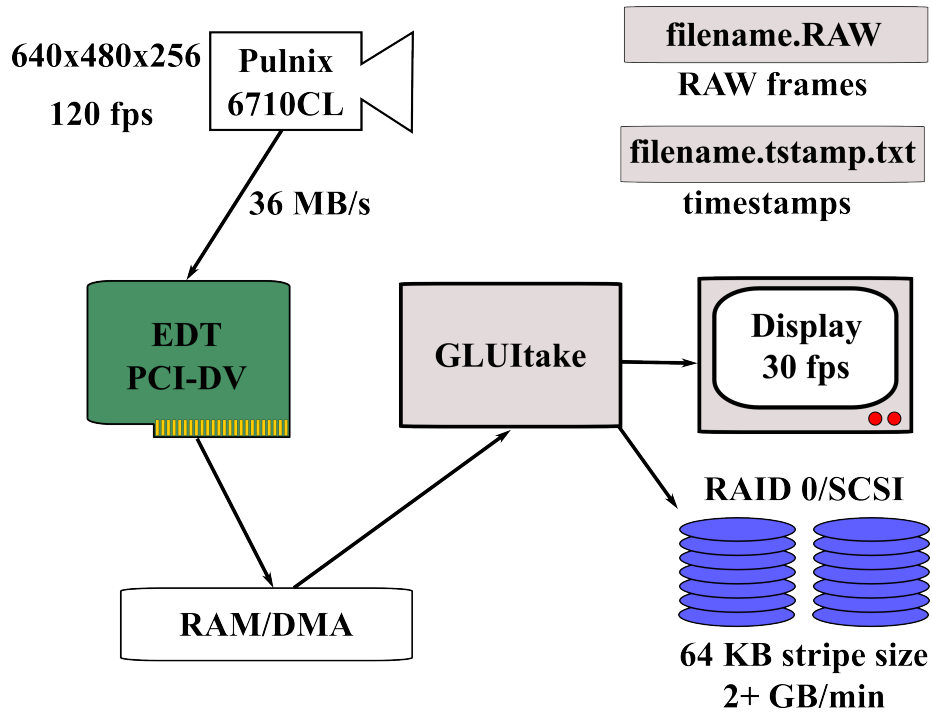


Figure 3.3: Brightfield imaging in the 3DFM systems use a fast 120 fps camera, a frame grabber board, and a RAID array of SCSI disks to acquire and store all video with little to no dropped frames.

the imaged field approximately $100\mu\text{m} \times 75\mu\text{m}$.

3.3.1 Image Acquisition

Once a video frame is read by the Pulnix camera, the frame-grabber card “grabs” the frame and puts it into computer RAM (Random Access Memory) via Direct Memory Access (DMA). From Engineering Design Team (EDT) (www.edt.com), the PCI-DV C-Link PCI is a 33/66 MHz PCI board with sufficient bandwidth that can easily handle the amount of data coming from the Pulnix camera at full frame rate. EDT has a comprehensive and well-designed Application Programming Interface (API) that is available across platforms (Windows, Linux, Mac) and is complete with example code

to aid in software development. By combining this API with other critical components we are capable of grabbing full-sized frames at full frame rate (120 fps) and spin them directly to disk without frame loss. I was able to implement a simple video capture software application named `GLUITake` that has been used in our lab for more than 5 years. For more information, see Section 3.3.3.

3.3.2 Data Collection

In order to capture full video frames ($648 \times 484 \times 256$) at full frame rates (120 fps), the computer used to manage the hardware and process the incoming data must have a memory bus that is fast enough to manage the incoming data stream (easy) as well as a disk controller and drive fast enough to handle the incoming data from the memory bus (harder). Standard IDE drives are not sufficient since they are not capable of handling sustained bit rates of 40 MB per second and the drive's data buffer becomes quickly overrun. To circumvent this issue we use a 320 MB/s RAID (Redundant Array of Inexpensive Disks) controller (Adaptec, PERC 320/DC) and a set of two SCSI (Small Computer System Interface) drives (Seagate, model no. ST373453LW) placed in a striped array (Mode 0), such that roughly one-half of the data is captured by one drive whilst the second drive captures the rest. When configured so that the data stripe size is 64 KB, the RAID array provides sufficient and sustained throughput for our data collection needs. As long as there is little file fragmentation, the drive has sufficient space, and the computer's scheduler is not overbooked, we can collect all necessary data in a non-realtime operating system like Microsoft's Windows XP without dropping any

frames. The collected data from the EDT board are recorded into two separate data files, where the first is a binary file containing every pixel's luminance in sequence and the second being timestamp information saved as simple text (Figure 3.3).

3.3.3 GLUItake Software

GLUItake is a software application I wrote that simultaneously takes full-sized video data at full frame rate and allows the user to see the experiment on the screen *in situ*. Observing the progress of experiments in realtime is important because it reduces the feedback loop between the researcher and the resulting data, allowing one to proceed in research at a faster rate. For example, it is very satisfying to personally observe and know that magnetic particles moved when applying a current to our 3DFM magnetics subsystem *before* all the data are taken.

Aptly named, GLUItake (user interface seen in Figure 3.4) essentially combines the source code found in the example EDT application `take` with example code that uses the GLUI (GLUT User Interface) toolkit. With GLUItake, one can capture frames at 120 fps or any divisor of 120 that results in an integer greater than one, as GLUItake just skips the requisite number of frames to reduce data load. Other parameters in GLUItake include EDT board ID (called "unit"), EDT channel (in the case more than one camera is available in hardware), gain, and video duration.

GLUItake requires the use of two separate threads; the first thread has a higher priority in order to successfully record data while the second and less important thread

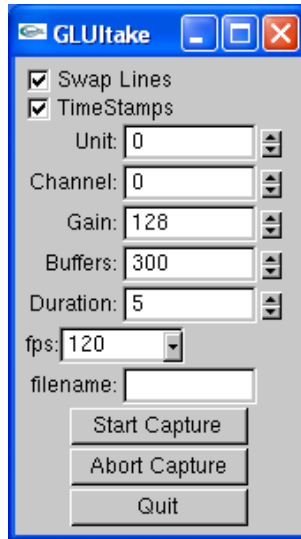


Figure 3.4: GLUTake is a software application that grabs collections of video frames as RAW files with various parameters and allows a scientist to view the progress of an experiment in realtime while collecting video at maximum frame rate (120 fps).

is responsible for updating the image on the display. Even so, there may be several reasons for the processor of a non-realtime operating system to be busy, and to assuage this problem we use a circular, revolving FIFO (first-in first-out) buffer.

Because GLUTake is multi-threaded and needs to function in near realtime, the system requirements for top performance can be high. At minimum one needs a dual core or hyper-threaded machine running at clock speeds in excess of 2 GHz. The GLUTake project exists as a subproject of the CISMM Video software package written and maintained by Russ Taylor. Project dependencies for GLUTake include libraries for the EDT hardware (www.edt.edu), the Virtual Reality Peripheral Network (VRPN) (<http://www.cs.unc.edu/Research/vrpn>), as well as the aforementioned GLUTI toolkit (<http://glui.sourceforge.net/>).

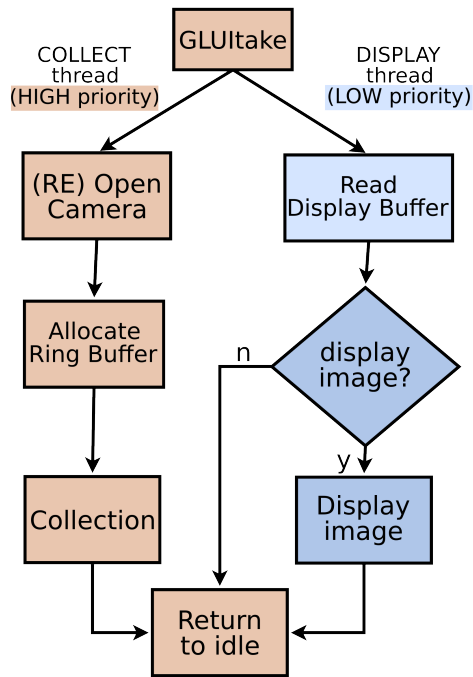


Figure 3.5: GLUTake streams two threads to the processors simultaneously, one high priority thread collects the video frames and writes to disk at a max 120 fps while the low priority thread handles the user interface and the display of the current frame at a constant 30 fps.

3.3.4 Particle Tracking

Also part of the CISMM Video package, the Video Spot Tracker (VST) program effectively tracks objects that are rod-shaped or radially symmetric. VST, at version 5.27 at the time of this writing, offers many features to aid the burdened user who is required to track objects through pervasive visual noise such as dead pixels, background obfuscation, and drifting in and out of the image plane. Using three kernel types, i.e. disk, cone, or radial, a user can hand-select spots that fit these shape/luminance profiles, watch as VST follows the trackers, and save the location information to a vrpn logfile. A tracking heuristic along with a “debug kernel” option provides the user with some

measure of confidence that objects are being tracked with sufficient precision.

Measures are largely implemented or currently in development to reduce the amount of user involvement necessary to track useful objects successfully. Examples of such additional functionality include a tracking integrity heuristic that identifies when a tracker is “lost” and can then delete such a tracker, hover about the area until a viable signal resurfaces, or alert the user to intercede on the software’s behalf. Also in place is a method for automatically identifying potentially trackable objects. The combination of these two algorithms has the potential for making VST completely hands-off and a great tool for high-throughput implementations of the 3DFM (Spero et al., 2008).

3.3.5 Measurement Resolution

Characterizing the noise of VST occurs in two major steps. To determine the accuracy and precision of the algorithm and the robustness of the software, VST is checked against a set of completely reproducible and simulated test images, complete with quantifiable amounts of background noise. In idealized images with little to no noise and optimal contrast, VST can track stationary objects with a mean radial error of ~ 0.001 pixels. For more realistic cases of a moving spot with moderate noise, this is reduced to 1/100th pixel precision (Schubert, 2009).

We can use the same method to test the position detection sensitivity for the video tracking that we used for the laser tracking system (Fisher, 2007). Using the same method will allow us to cleanly compare the noise levels found for each system. We im-

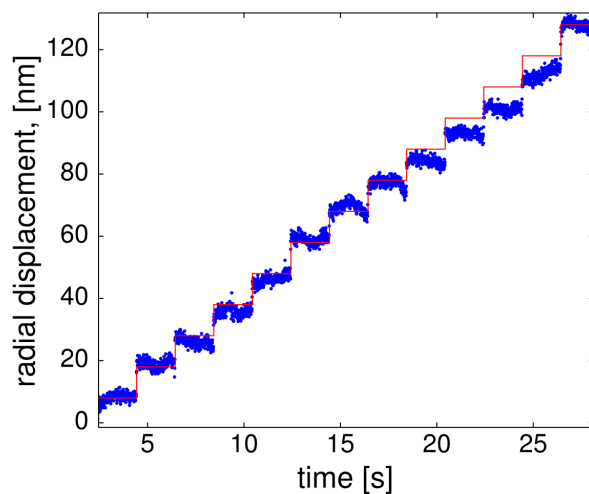


Figure 3.6: Tracking a bead that translates in a staircase shape reveals the sensitivity of the Hercules video tracking system which includes the optics and camera hardware in addition to the algorithms of the Video Spot Tracker software. Tracking ideal spots is about $10\times$ better than actual beads imaged in the microscope.

mobilize $1\ \mu\text{m}$ polystyrene beads (Polysciences, Inc., Warrington, PA) in a 1% solution of agarose. Another method we commonly use (only for video tracking) immobilizes the same type beads by evaporation (1:10 bead solution:ethanol) onto a $24 \times 50\ \#0$ coverslip which are then cured into place with an optical adhesive (Norland No. 81; Norland Products, Cranbury, NJ). For both methods we tracked the bead motion while applying steps with the nanopositioning Mad City Labs (MCL) stage (model Nano-LP 100; Mad City Labs Inc., Madison, WI). We trust the MCL stage as a position reference because it operates on a position feedback loop and has a reported position error of 1 nm, which is more precise than we expect for video tracking.

The laser tracking system for the 3DFM should be more sensitive than the video tracking. When we compare these video tracking sensitivities with those found in for the laser tracking subsystem of the 3DFM (pictured in Figure 3.7), we find our suspicions

true within a factor of four.

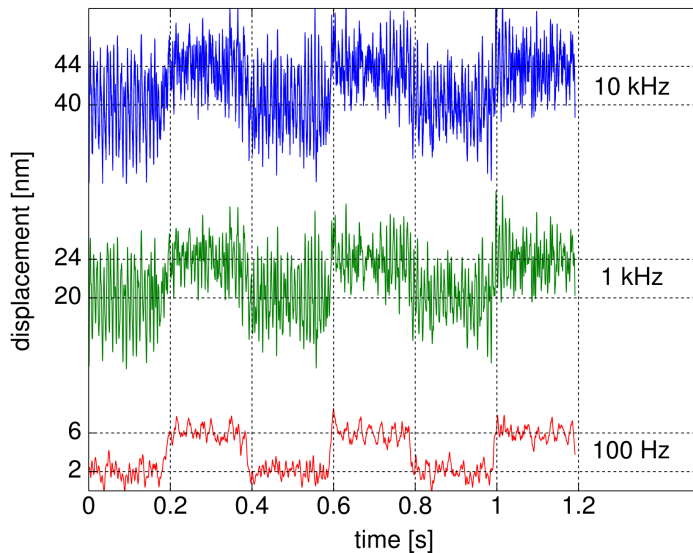


Figure 3.7: The 3DFM laser tracking system is more sensitive (4 nm) to bead position compared to video tracking (16 nm) and can track at much higher bandwidth (100 kHz compared to 120 Hz), but is limited to tracking only spheres which are similar in size or smaller than the beam waist of the laser and to tracking only one sphere at a time. Simultaneously tracking many particles of differing geometries is one of the advantages video tracking algorithms have over similar laser tracking systems.

We get a quantifiable amount of noise in position 1/20th of a pixel for most test cases. For a $60\times$ water-immersion objective, $1.5\times$ multiplier tube ($0.1\ \mu\text{m}/\text{pixel}$), this results in an error of $\sim 5\ \text{nm}$, and $\sim 8\ \text{nm}$ for $1.0\times$ multiplier tube ($0.15\ \mu\text{m}/\text{pixel}$).

3.3.6 Editing Video Tracking Data

Once we collect the video data and track the particle trajectories with VST, we quickly edit the new data, taking care to remove any stray points where the tracker strays from the target as well as subtract out any bulk sample drift that may obfus-

cate results, especially those where true diffusion is necessary. The Edit Video Tracking GUI (`evt_GUI`) is a user-interface constructed using Matlab that helps to quickly manage, browse, and edit video tracking data obtained from the CISMM VST. The VRPNtoMatlab utility must first be used to convert the logfiles from VRPN format to a matlab workspace (`.MAT`). Once the data are loaded and edited, the user can also take advantage of features in `evt_GUI` that plot relationships commonly found in both TMBR and DMBR measurements. All of the figures seen in this dissertation were initially constructed using `evt_GUI` or related software. More information about `evt_GUI` can be found in the user's manual.

3.4 Magnetics Subsystem

Forces within the 3DFM are difficult to predict due to the many variables that affect the magnetic field and field gradient experienced by the sample-embedded probe. System performance depends on both the pole plate assembly and individual experiment parameters. The field and field gradient are sensitive to the pole plate material and microscopic changes to the geometry and tip sharpness. Variation exists between experiments because of changes to the magnet drive current and bead location, as well as the bead type and diameter (O'Brien et al., 2008). In the past, each pole plate required recalibration for every new experimental setup to determine absolute force values. It was also impossible to systematically evaluate many of the variables necessary to optimize pole plate design.

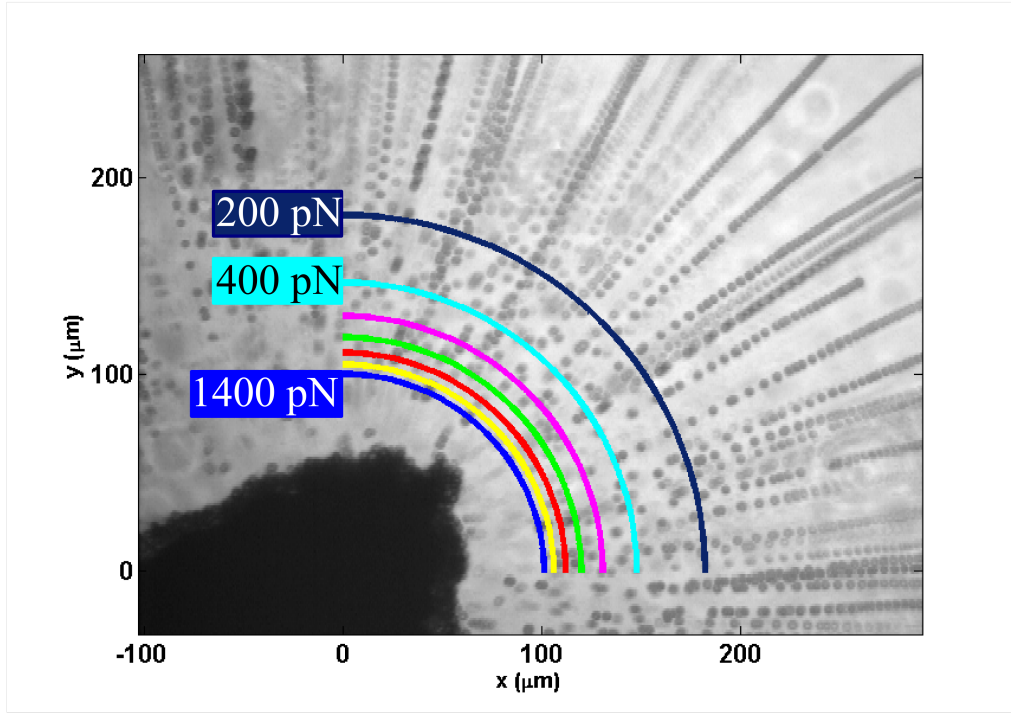


Figure 3.8: Time-lapsed image projection of beads pulled into the magnetized pole-tip located in the bottom left corner. Contour lines indicate the applied force at the appropriate distance.

Variable force calibration (VFC) provides a convenient and accurate way to construct a spatial force map and determine the effects of different construction techniques (Spero et al., 2008). Prime considerations in the design of the VFC protocol are the dependences of $\nabla(B \cdot B)$ on both input current, I and distance, r , from the pole tip. We can use the VFC technique to determine the effect of material, tip geometry, and input current on force magnitude. To accomplish the calibration, I drive the magnets with a repeated sequence of step pulses with ascending amplitude and use video tracking to record the changing position of beads in a Newtonian fluid of known viscosity. To ensure no bead-bead coupling, I use a small enough concentration of beads that the

average bead-to-bead distance is 20 bead diameters or more and exclude any tracks that have bead-bead distances of less than 5 bead diameters. After synchronizing the force and position information with the magnet drive history, I use best linear fits to determine bead velocity and then compute the force on a bead as a function of location and drive current.

3.4.1 The Magnetics Stage

The 3DFM magnetic stage subsystem (Figure 3.9), described previously in Fisher, et al., consists primarily of magnetically permeable material for cores, surrounded by 20+ Amp turns of low-resistance copper wire and supplanted with thin-foil pole tips in one of many different custom geometries (Fisher et al., 2006a). In such experiments, we used top-only magnetic cores coupled with the thin-foil “pole-flat” geometry shown in Figure 3.10. The pole tips, glued to a 24×40 #1½ cover-slip with quick-drying no-sag epoxy, were, in turn, glued to the castellation cores of the magnetics system driving ring via Elmers™ glue (Fisher et al., 2006a). A Newtonian viscosity standard embedded with magnetic microbeads fills the space between the upper and lower cover-slips containing the magnetic pole tips. We minimized fluid drift by encasing the sample inside a silicon grease ring and using sample volumes of 10 μL or less.

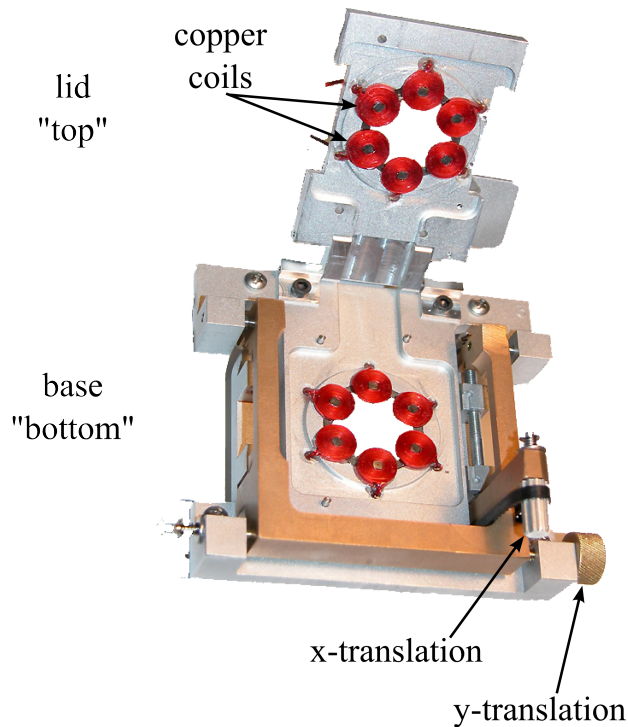


Figure 3.9: The stage lid and base are shown opened, with the magnetically permeable cores showing, each wrapped around with copper wire. For DMBR experiments, we attach a poleflat geometry to the top cores and place a small volume of sample on a coverslip placed on the bottom cores. X and Y positioners handle the translation of the Sample with respect to the magnetic pole tip.

3.4.2 Pole Tips

Magnetic Shield Corporation (<http://www.magnetic-shield.com>) supplied the two soft magnetic foils, Netic and Co-Netic AA, we used to construct the 3DFM pole tips. Table 3.1 summarizes the magnetic properties of both materials.

The high saturation point for the Netic material should result in a higher achievable maximum force than those for the Co-Netic foils. The higher permeability of the Co-

Material	Saturation Induction (Tesla)	Permeability	Coercivity (Oersteds)
Netic	2.1	200	1.0
Co-Netic AA	0.8	30,000	0.015

Table 3.1: Magnetic Materials used for 3DFM pole tips

Netic material should cause a faster rise in force than that found in the Netic material for an equal step increase in drive current. The low Co-Netic coercivity should reduce the remanence experienced after magnetization.

Currently, the pole tips are prepared commercially by FotoFab (<http://www.fotofab.com/>), where acid etches them to their desired geometries via a photolithography process (Fisher, 2007) with minimum diameters (maximum sharpness) of 15-20 μm . We hypothesized that a sharper tip would increase the field gradient and therefore the force applied to a bead. By scraping off the excess material with a #0 glass cover slip and a dissection grade microscope, we sharpened tips manually and attained a minimum tip diameter of 5-6 μm .

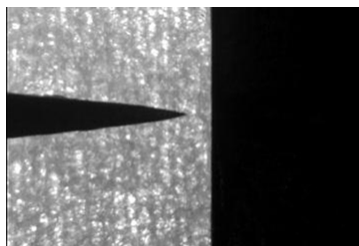


Figure 3.10: The pole flat geometry used in DMBR experiments with the 3DFM.

To mount the tip rigidly to its substrate we glued the tip and its accompanying flat piece to a #0 glass coverslip with a cyanoacrylate glue. In addition to tip diameter, we

Method	CAP-Visc	CAP-Freq	CAP-Creep	TMBR	DMBR
N	7	30	3	12	1
Mean Viscosity (mPa s)	27.6	30.2	28.2	26.2	27.3
Standard Deviation (mPa s)	0.34	0.27	0.7	4.4	0.9
Standard Error (mPa s)	0.13	0.05	0.4	1.3	0.9
Expected Value from Model	23.5	23.5	23.5	23.5	23.5
Percent Error from Model	17%	27%	20%	6.0%	15%

Table 3.2: Newtonian viscosity of 2 M sucrose. Solution temperature is assumed to 23 °C for TMBR and DMBR and is controlled at 23 °C for all rheometer methods. All methods report expected values within acceptable error for viscosity.

believed that the spacing between the tip and flat should affect the field by influencing the flux return path. For trials where we compared multiple pole plates, we fixed the gap between tip and flat at 900 μm in order to minimize the effect of any inaccuracy in tip position.

3.4.3 Calibrating with Newtonian Fluids

In theory, we can use any Newtonian fluid for the VFC protocol provided that its viscosity is well characterized. Large noise values in the viscosity of the calibrator fluid will propagate into the determination of force. For instance, sucrose solutions are good candidates since they are highly water-soluble and have predictable viscosities for any concentration below solubility limits and any temperature below 100 °C by a published model to 1% error (Mathlouthi and Reiser, 1995). In contrast, a disadvantage of these solutions is their relatively low viscosities. Although less fully characterized, we also use Karo™ corn syrup for calibrations that require high forces because of its relatively high viscosity of 3.4 Pa s (see Figure 5.5)

The Mathlouthi model predicts the viscosity of a sucrose solution as a function of the sucrose concentration and the solution's temperature (Mathlouthi and Reiser, 1995). The solution density is determined through a recursion model that repeats the algorithm until the error is below a low tolerance value. The function fails to converge at concentrations that exceed solubility limits of sucrose at the given test temperature. As such, the model is a fourth-order polynomial fit published by Bubnick in (Mathlouthi and Reiser, 1995) that predicts viscosity values to within 1%, provided these solubility and temperature constraints are met.

The expected viscosity for a 2 M sucrose solution at 23 °C is 23.5 mPa s. The percent error for a test solution made using the protocol in Appendix A.1 is systematically high at about 15.4% from the expected value (see Table 3.2). This error could have been introduced during the preparation of the sucrose solution and demonstrates the need to check each Newtonian standard after its manufacture. Less likely, the error may be attributed to evaporative losses around the sample-air interface on the rheometer during testing. Evaporation would contribute to a higher concentration of the test solution and thus a higher viscosity.

Briefly, the model published in (Mathlouthi and Reiser, 1995) computes the viscosity of a sucrose solution when given an input molar concentration and solution temperature. The ability to predict the viscosities of sucrose solutions have proven invaluable when modeling or simulating a rheology experiment, force calibration, or when planning an experiment whose dynamics need to be slowed to meet observation requirements in the instrumentation (Fisher, 2007). Typically sucrose solutions are well tolerated in

biological situations.

Newtonian fluids, such as the 2 M sucrose solution used here, exhibit independence of their viscosities to varying input stress/shear rates. Shear stresses ranging across four orders of magnitude, from 0.01 Pa to 100 Pa, were applied to the standard 2M sucrose solution and resulted in a population of 8 viscosities ranging from 27.0 - 28.1 mPa s. A single-factor analysis of variance shows statistically that varying the input shear rate does not influence sucroses viscosity ($p = 0.58$, where $p < 0.05$ denotes statistical significance). Treating these values as a population of independent observations results in a mean viscosity of 27.6 mPa s with a standard error of 0.13 mPa s.

Solution (units)	Model Viscosity (mPa s)	CAP Viscosity (mPa s)	Temperature (°C)	Force Range (pN)
2M sucrose	23.5	28.2 ± 0.4	23	< 300
2.5M sucrose	122.2	125 ± 1	23	< 1000
Karo	–	3400 ± 100	23	> 1000

Table 3.3: Newtonian Standard Solutions used in VFC

We collected viscosity data for these solutions with either a Bohlin Gemini or a TA Instruments AR-G2 stress-controlled cone and plate rheometers. For the sucrose solutions, we used a 1°/60mm cone and for the corn syrup we used a 1°/40 mm or 4°/40 mm cone. Using the creep compliance test method, we applied step stresses that ranged from 1 Pa to 1000 Pa. When subjected to an input step stress, Newtonian fluids such as these standards result in a constant shear rate. Dividing the applied input stress by this resulting constant shear rate provides the dynamic viscosity of the test solution. Listed in Table 3.3 are the solutions currently used in VFC as well as their predicted

and measured viscosities.

3.4.4 Variable Force Calibration

I developed the VFC software to sample the force field around the pole tip as a function of both distance, r , from the pole tip and the drive current, I . I use VFC with the 3DFM to explore the effect of pole material, drive current, and bead position on force.

A datum of calibration is the bead velocity at each drive current in each pulse sequence. Consider, for instance, a population of n beads, each subjected to p pulse sequences in which each pulse sequence comprises d pulses at specified drive currents. A calibration set then includes npd data, where typical values are $n = 20$, $p = 10$, and $d = 10$. As a consequence of this design, increasing d improves resolution in measuring how force varies with drive current. Increasing n minimizes error due to bead-to-bead variation in force. Finally, shortening the dwell time of each pulse increases p and also moves the beads a shorter distance during each pulse sequence, thereby improving spatial resolution in the force calibration (Spero et al., 2008).

3.4.4.1 Randomization of Magnetic Domains through Degauss

After applying a magnetic field materials suffer hysteretic effects due to residual, internal ordering of the microscopic magnetic domains. Observed as residual magnetic field with zero applied current, these effects induce a net drift velocity for the magnetic probe beads. The remanent magnetization may mask a lower current when first a high

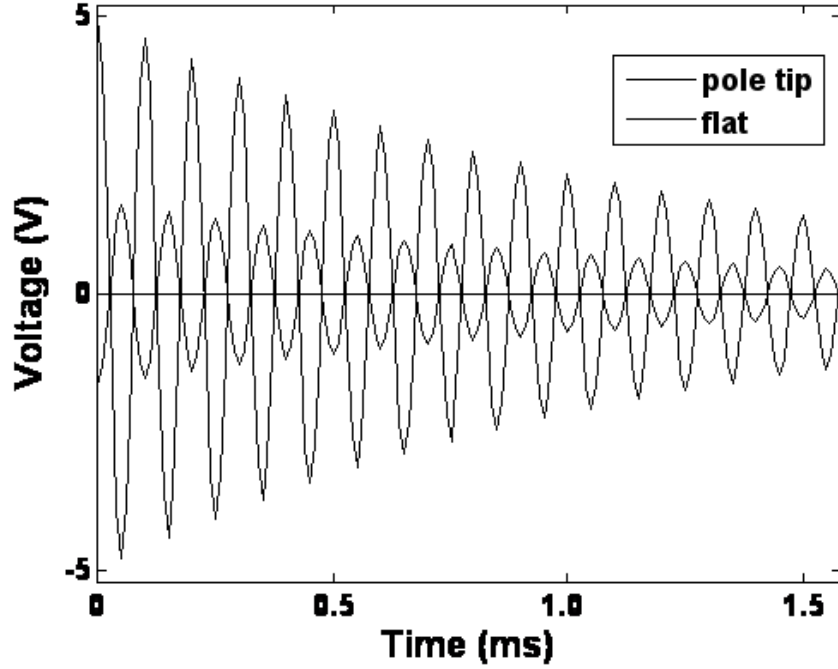


Figure 3.11: I use a decaying sine wave of current to degauss the pole tip and eliminate remanent magnetization.

current is used to drive the system. A degaussing routine reduces the residual field by scrambling the orientations of the magnetic domains. We apply a decaying sine function to the magnetic coils of the form

$$I(t) = I_{max}e^{-t/\tau} \sin(2\pi ft) \quad (3.4)$$

where $I(t)$ is the time-dependent current, I_{max} is the maximum current applied since the last degauss, τ is the decay time constant, and f is the frequency of the incident sinusoid. Our magnetic drive system is capable of driving its full power of 2.5 A at frequencies up to 10 kHz (Vicci, 2005).

Applying a short duration (> 10 ms) degauss pulse successfully eliminates the

remanent magnetization from the pole tips. To degauss the poles, we applied a drive current in the form shown in Equation 3.4. For the 3DFM, the pulse consisted of a decaying 10 kHz sine wave sampled at 100 kHz with a time constant of 1.2 ms, equivalent to a 10% decay in amplitude for each cycle (Fig. 3.11). The first 10 ms of the degauss procedure has an RMS current is 440 mA while during the next 10 ms it is only 0.11 mA. We determined the bead velocities at zero current prior to each degauss pulse in order to estimate the remanent force and after to estimate forces due to bulk fluid flow or instrumental drift.

The degauss routine decimates even the remanence force produced by a Netic pole tip. Figure 3.12 shows a 0.1 s, 2.5 A drive pulse followed by 0.4 s with no actuation, except for the degauss routine occurring at 0.25 s. The force achieved during the initial 5 volt pulse was 72 pN, which dropped to 12 pN when actuation ceased. The degauss further reduced the remanence to less than 0.3 pN, making it nearly indistinguishable from Brownian effects. The high forces initially generated during the degauss procedure have a negligible affect due to their minimal duration and low RMS.

3.4.4.2 Driving the Magnets

Using Matlab, we created a graphical environment where the user constructs a sequence of step currents and drives the magnetics system by repeating these sequences. Each pulse sequence typically uses increasing step functions (Fig. 3.13) to prevent remanent effects during any given sequence. Inserted midway in the zero current pulse is the degauss function that eliminates remanence before beginning the next sequence.

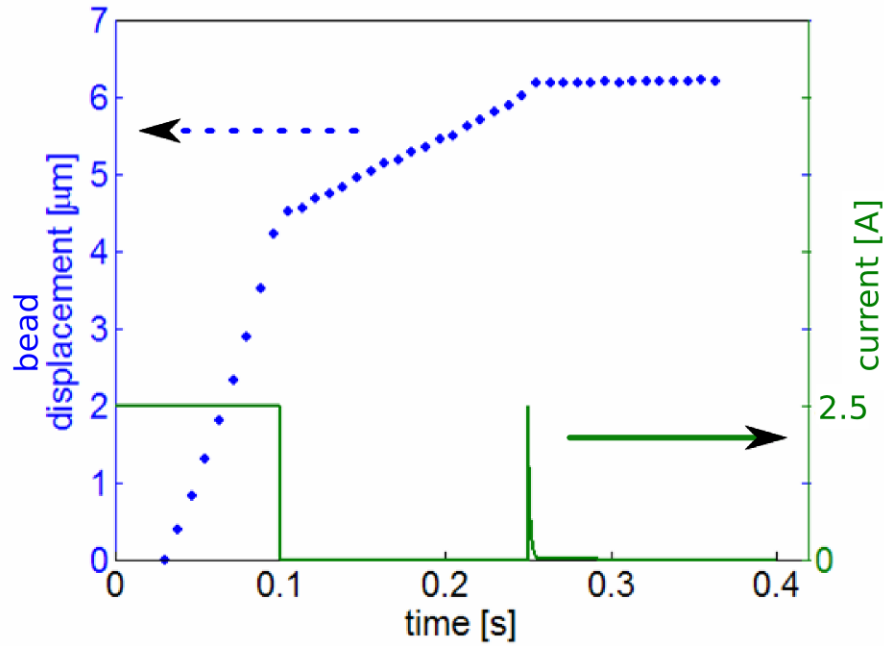


Figure 3.12: Bead displacement during and after applied current and after de-gaussing. The de-gauss pulse is fast enough to be scarcely detected with regard to bead displacement and yet is completely successful in eliminating the poletip’s remanent magnetization.

The user sets the amplitude and duration of each pulse as well as the total number of sequences. Though not strictly necessary, we actuated the three coils driving the flat with $-1/3$ the current powering the pole tip drive coil to provide an active flux return path. A National Instruments PCI-6713 Data Acquisition card provided the voltages used as inputs that controlled the transconductance amplifier (Vicci, 2005) and drive the magnet coils. Matlab stored each experimental protocol as a metadata file that included the sequence parameters as well as the starting time on the DAC clock as well as the DAC board ID.

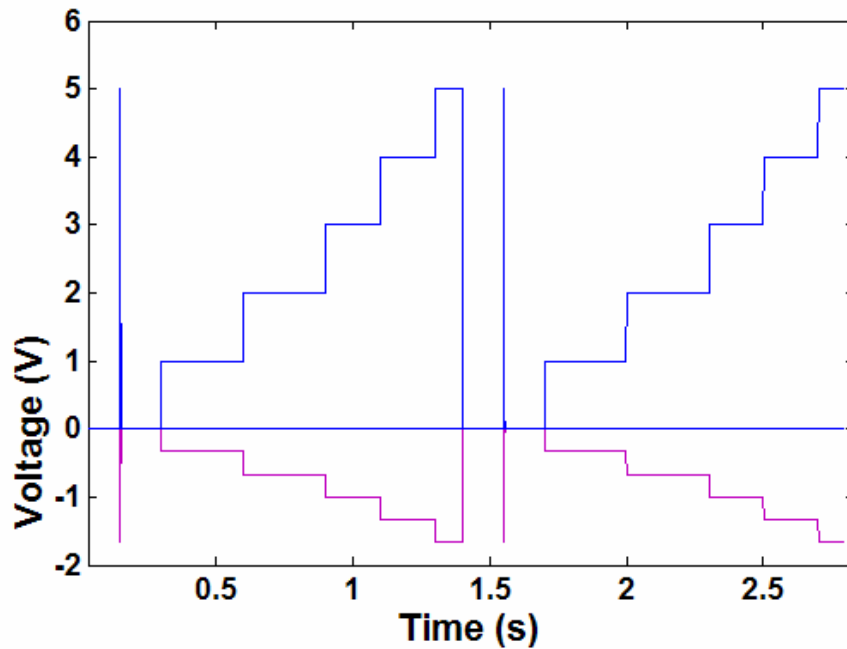


Figure 3.13:

3.4.4.3 Capturing and Processing Video Data

The `GLUITake` program captured and stored video frames in a RAW pixel format ($648 \times 484 \times 256$) at rates up to 120 frames per second (fps) for variable durations that rarely exceeded 180 seconds. Version 5.x of CISMM Video Spot Tracker (<http://cismm.org/downloads>) tracked bead position and recorded the changing XY coordinates of each bead during every frame. The output `vrpn` file was converted to a Matlab workspace using the CISMM `vrpnToMatlab` software package (<http://cismm.org/downloads>). Tracking artifacts and data for beads outside the region of interest were manually removed using `evt_gui`, also available from CISMM.

3.4.4.4 Locating the Pole-tip

To determine the physical location of a particle with respect to a coordinate system, we must locate its origin. To do this, we must find the virtual monopole located somewhere within the pole tip (shown in Figure 3.14). We first measure the radius of the inscribed circle found at the pole tip because placing the monopole at the center of this circle is a good first approximation. To be more precise, we fit the last 40 points of each tracker to a set of parametric equations linear in x and y extending the bead trajectories to a point of common intersection. These line fits roughly intersect at the monopole location because the particle trajectories converge onto the pole tip. We can increase the accuracy of the initial estimate by minimizing the orthogonal distances to the aforementioned fits and place the monopole at the intersection point. After locating the origin of the polar coordinate system, we transform the coordinates of $[x(t), y(t)]$ into this system to find $r(t)$.

3.4.4.5 Analyzing the Processed Data

After we tracked the particle displacements in the video streams, we synchronized and merged them with the magnet drive history to a temporal resolution of approximately 8.6 milliseconds. This synchronization minimized discrepancies between the clocks of different computers running the 3DFM and ensured that a given bead trace was associated with the correct magnet drive current.

During each single magnet pulse, we gave each particle trace a linear fit whose slope

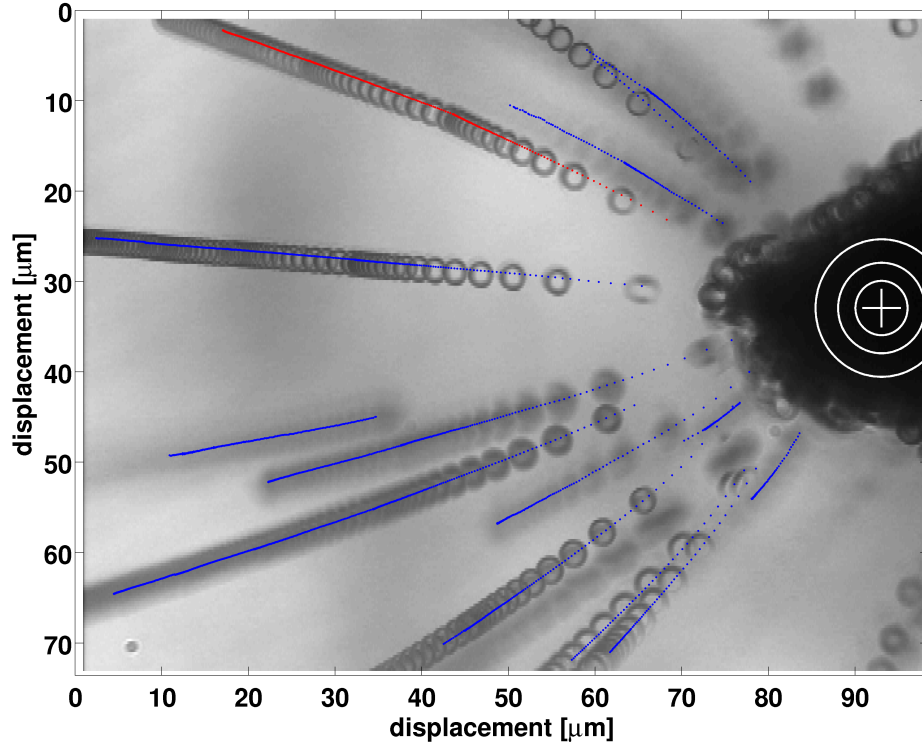


Figure 3.14: Locating Virtual monopole in 3DFM

corresponded to the average bead velocity. The `robustfit` function in Matlab managed these fits. `robustfit` uses an iterative method to find the best fit line, throwing out any outlier it finds according to its protocol. The reported error in forces determined here is not calculated using `robustfit`, i.e. it includes all points including outliers. The velocities were each converted to corresponding forces with Stokes drag for the prescribed particle geometry, described earlier as Equation 2.43. For each pulse, we used the force occurring at the geometric midpoint of the particle path. The line fit approximation is valid because the local magnetic field and gradient remain relatively constant over small bead displacements. To complete the spatial map, we fit the force versus distance data for each current to a line in logarithmic space. This allows one to

interpolate the force at any point (see Figure 3.12) using the expression:

$$F = 10^{m \log(d)+b} \quad (3.5)$$

where d is the distance from the pole tip, F is the force on a bead, and m and b are constants determined by the linear fit. We measured the position radially within the sample plane from the pole tip center minus the tip radius. Because COMSOL modeling showed that field and field gradient are consistent for narrow cone angles at a given radius, we chose to ignore the effect of arc angles less than 30° . Beads found outside the $\pm 30^\circ$ angle from the line of symmetry for the pole geometry were removed from the computation as the force varies significantly outside that angle.

To estimate the error in the calibration of forces, we analyze Eq. 3.5 for propagation of error in m , b , and D , i.e.

$$\delta_F^2 = \left(\frac{\partial F}{\partial m} \delta_m \right)^2 + \left(\frac{\partial F}{\partial b} \delta_b \right)^2 + \left(\frac{\partial F}{\partial d} \delta_d \right)^2 \quad (3.6)$$

where,

$$\frac{\partial F}{\partial m} = \frac{\ln(d)}{\ln(10)} F \cdot \ln(10) \quad (3.7)$$

$$\frac{\partial F}{\partial b} = \frac{m}{d \ln(10)} F \cdot \ln(10) \quad (3.8)$$

$$\frac{\partial F}{\partial d} = F \cdot \ln(10) \quad (3.9)$$

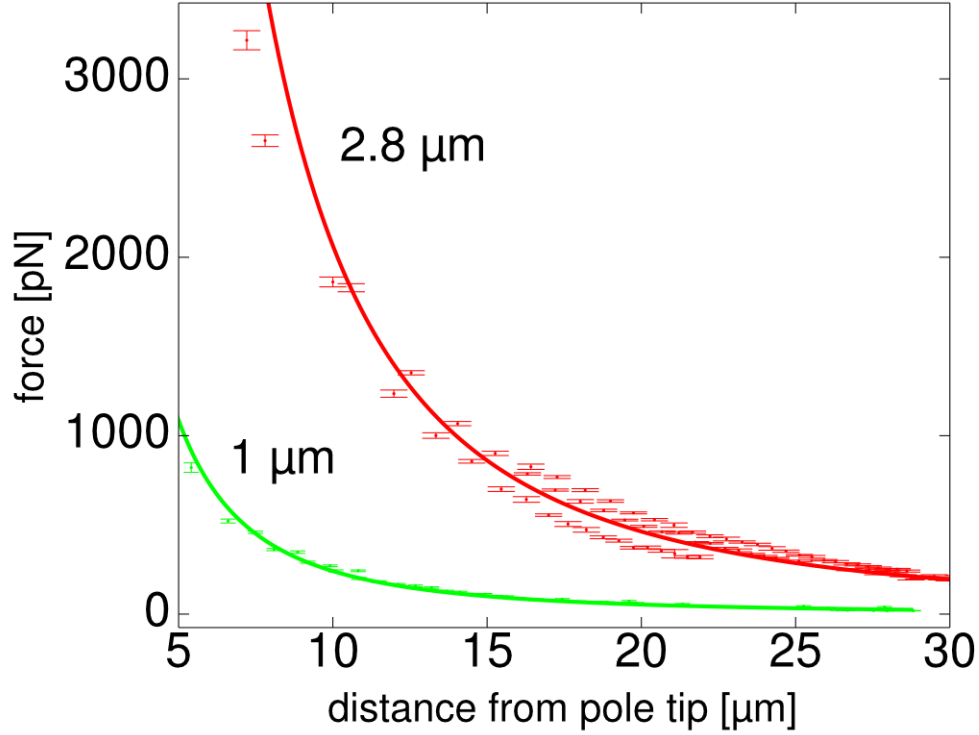


Figure 3.15: Maximum current applied to magnetic system produces maximum force vs displacement curves for 1 and 2.8 μm beads.

Therefore the relative error in F becomes

$$\frac{\delta F}{F} = \sqrt{\left(m \ln d \cdot \frac{\delta_m}{m}\right)^2 + \left(m \cdot \frac{\delta_d}{d}\right)^2 + \left(b \ln 10 \cdot \frac{\delta_b}{b}\right)^2} \quad (3.10)$$

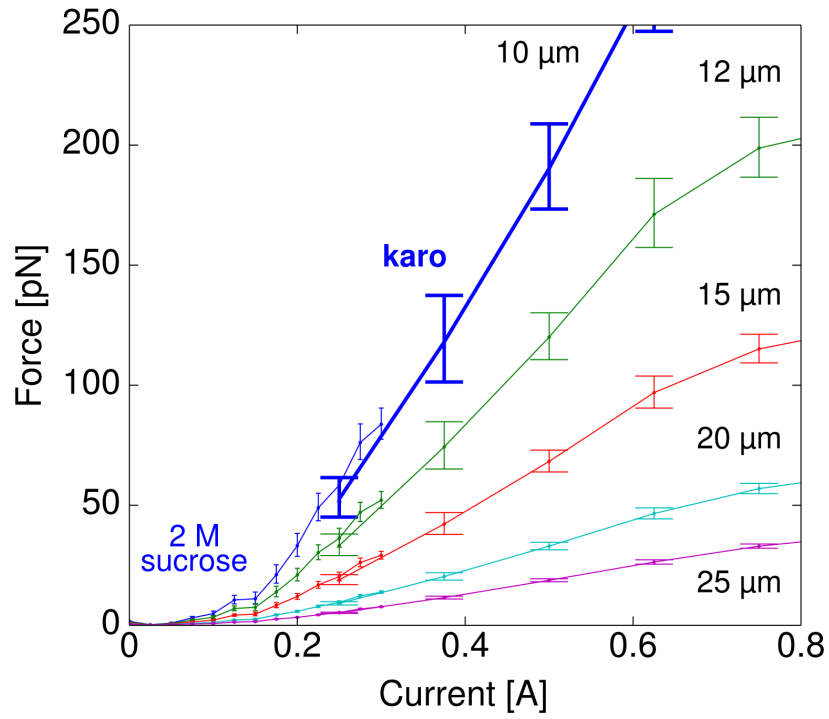
The largest relative error should be that of d , the position of the bead with respect to the poletip. This error should be less than 10% and includes not just the bead's tracked position, but the monopole location as well. The relative error in d must be an order of magnitude larger than relative errors in m and b to contribute equally to the error in F . As such, errors in m and b should be approximately 1% to get a reasonable error in F .

We tested the precision of the VFC technique through repeated experiments with the same pole plate but with different fluid standards. Figure 3.16(a) shows the force on a 1 μm bead located 12 μm from the pole tip as measured with both 2 M sucrose and corn syrup. The results have less than 10% error at currents less than 1.5 A and 20% thereafter (full dataset not shown).

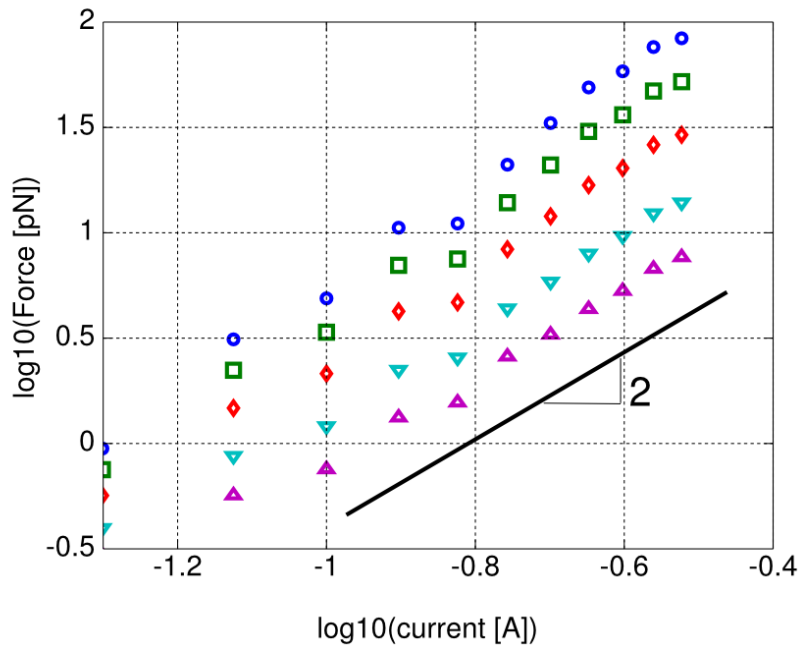
When we used 2.5 M sucrose as the standard fluid we were able to measure forces for all input currents during a single calibration run with moderate and acceptable error. When we took advantage of different calibration fluids for different force ranges we were able to increase the sensitivity to and lower the standard error on our low force measurements. This sensitivity is demonstrated in Figure 3.16(a) where we measured low current pulls using 2 M sucrose and high currents with corn syrup.

3.4.4.6 Bead and Poletip Saturation

We used the new range of easily measurable forces to demonstrate the magnetic saturation of 1 μm Dynal beads at various distances from the pole tip, shown in Figures 3.16(a) and 3.17. Although readily predicted, it is the first time we observed bead saturation solely with the 3DFM. In Section 2.4.1 I reported the magnetic force experienced by a particle as $\vec{F}_m = (\vec{m}_{eff} \cdot \vec{\nabla}) \vec{B}$ (Eq. 2.88) when the incident field behaves approximately as a monopole source at far distances from the poletip. The effective magnetization of the particle, \vec{m}_{eff} , is itself a function of \vec{B} while we assume \vec{B} and $\nabla\vec{B}$ are linearly proportional to the current applied to the electromagnet, I_{app} . This assumption breaks down once the bead and/or the poletip reaches its saturation



(a) linear space- Early quadratic appearance, late linear



(b) log space- power law with slope=2

Figure 3.16: Low applied current shows I_{app}^2 dependence on force because neither beads nor poletip have saturated.

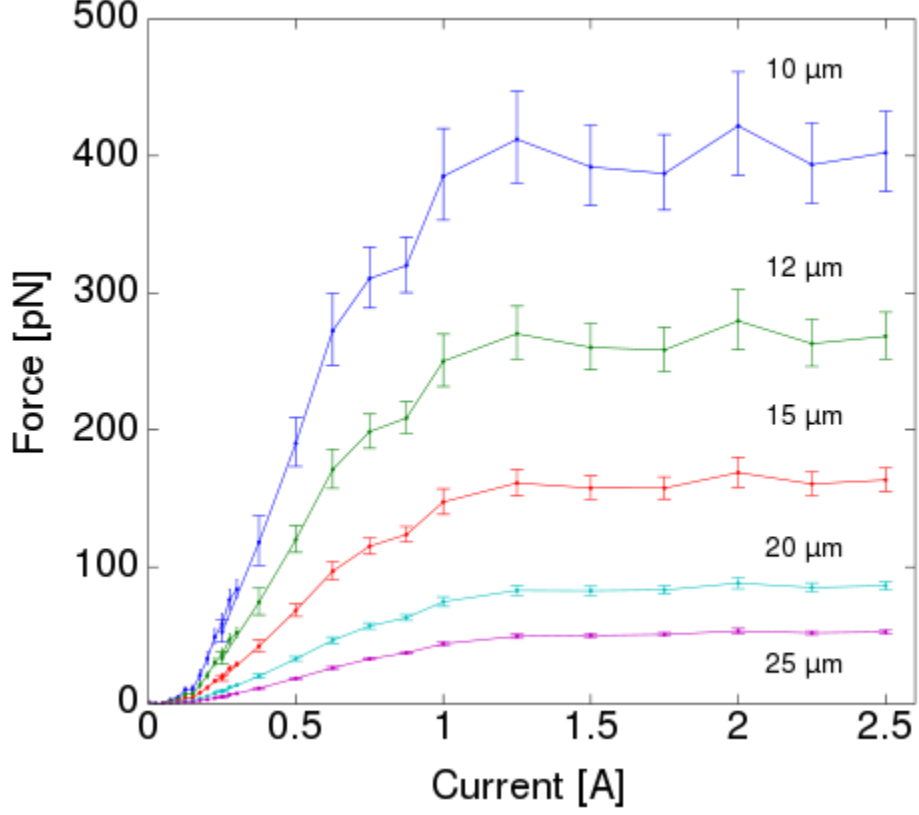


Figure 3.17: Applying high currents shows saturation of poletip as evidenced by the lack of increase in force for any corresponding increase in current.

magnetization. When both the bead and poletip are unsaturated $\vec{F}_m \propto I_{app}^2$. The bead should saturate first, leaving $\vec{F}_m \propto I_{app}$. When both become saturated \vec{F}_m becomes invariant to any additional I_{app} .

Bead and poletip saturation become apparent in the data seen in Figure 3.16. For small input currents the empirical curve possesses the proper theoretical quadratic shape (Fig. 3.16(a)) and a power law value close to 2 (Fig. 3.16(b)) that is consistent with the monopole approximation. As the current increases the bead reaches its saturation limit first, primarily because of its smaller volume and density, making its induced

\vec{B} insensitive to additional I_{app} and reduces the applied force to a linear dependence on current. Further increases in current saturate the poletip and the force-current relationship plateaus to a slope of zero, shown in Figure 3.17.

3.4.4.7 Netic vs. CoNetic Material Response

We calibrated the pole tips with the complete force range and measured the magnetic saturation curves for various pole tip types. Figure 3.18 compares the forces as a function of current for Netic and CoNetic pole tips, 21 and 32 μm respective diameters, experienced by a 1 μm Dynal bead located 10 μm from the pole tip. Although the magnetic properties of both materials are well characterized, never before had we established saturation, primarily because of the unknown field strength and the aforementioned difficulty calibrating at the full range of currents. The calibration curve confirms the theoretical prediction for the materials performances. These data establish the dominant effect of the saturation point over the permeability, revealing a nearly 8-fold increase to the maximum force. The known presence of saturation will improve future instrument designs by relaxing constraints on the minimum field strength.

Although the effect of pole tip geometry has been modeled in COMSOL, nonidealities require that we collect empirical data from the 3DFM. Figure 3.18 also compares the forces produced by photo-etched and manually sharpened pole tips at 21 and 5 μm diameters respectively.

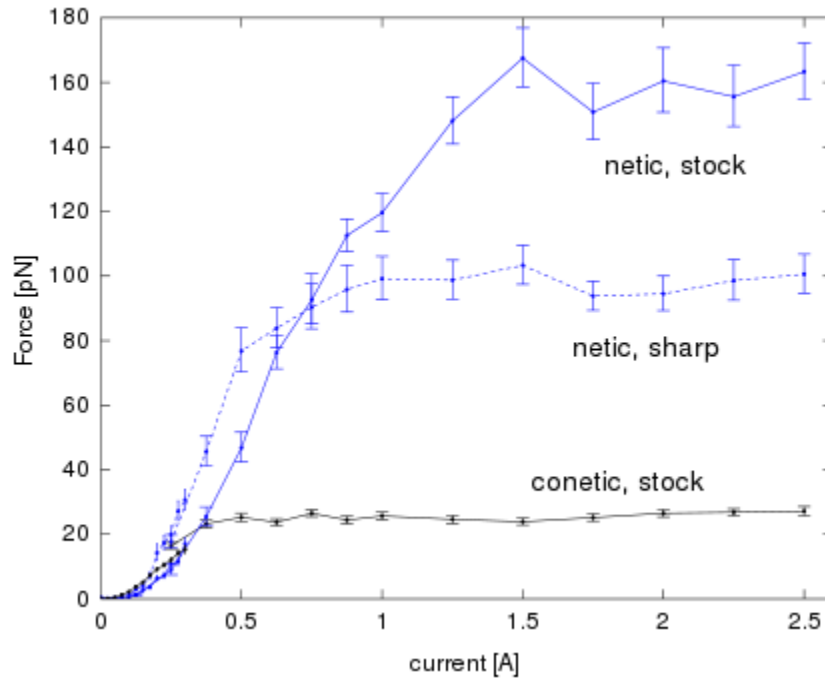


Figure 3.18: Forces on MyOne beads, 10 μm from pole-tip surface

3.5 Limits of measure with 3DFM Rheometry

With the system noise quantified for both our tracking and magnetic manipulation subsystems, we can identify and define our limits for microrheometric measurements in both thermal and driven techniques.

3.5.1 Thermal Methods

Measuring the microrheological properties of any material involves recording images with the video subsystem and tracking the random paths of embedded and diffusing particles. Diffusive measurements sample a bandwidth-limited frequency response of a material, here assumed to follow the Maxwell model with a constant shear modulus, G

and viscosity, η . Three instrumental quantities constrain our measurements of G and η with thermal microbead techniques: maximum video bandwidth, maximum video duration, and video tracking resolution.

The maximum video bandwidth defines the smallest time scale for the MSD measurements. In the 3DFM the maximum frame rate when capturing full-frames is 120 fps, or, a frame every 8.6 ms. Limiting video duration is either storage space for the acquired video data or drift in the instrument or specimen. For 3DFM experiments, drift begins to emulate particle diffusion in the MSD plots at time scales greater than 100 seconds. In Section 3.3.5, we determined a maximum tracking resolution of 5 nm for 1 μm microspheres at full bandwidth, which corresponds to an approximate minimum MSD value of $2 \times 10^{-17} \text{ m}^2$ at 60 Hz.

To predict the maximum G we can measure in the 3DFM system, we assume that the 1 μm bead translates on the order of the noise floor (5 nm) across sufficient data points such that the slope of the MSD, α , is approximately zero. Using Eq. 2.82 this corresponds to $G^*(\omega) = kT/\pi(500\text{nm})(2 \times 10^{-17})\Gamma(1) = 70 \text{ Pa}$.

Similarly, to calculate both limits on η which are intrinsically linked to sampling duration, we would need sufficient data (assumed 10 points, here) to make a good estimate of α with an expected value of 1. To compute the maximum η at our longest sampled time scales we would need 10 points at the lowest sampled decade in τ . For our camera, operating at 120 Hz, this would correspond to close to the entire decade between 10^{-2} and 10^{-1} seconds, making our shortest dataset about 0.1 s with a maximum measurable viscosity of 0.3 Pa s and our longest dataset about 100 s in duration with

a maximum measurable viscosity of 3000 Pa s.

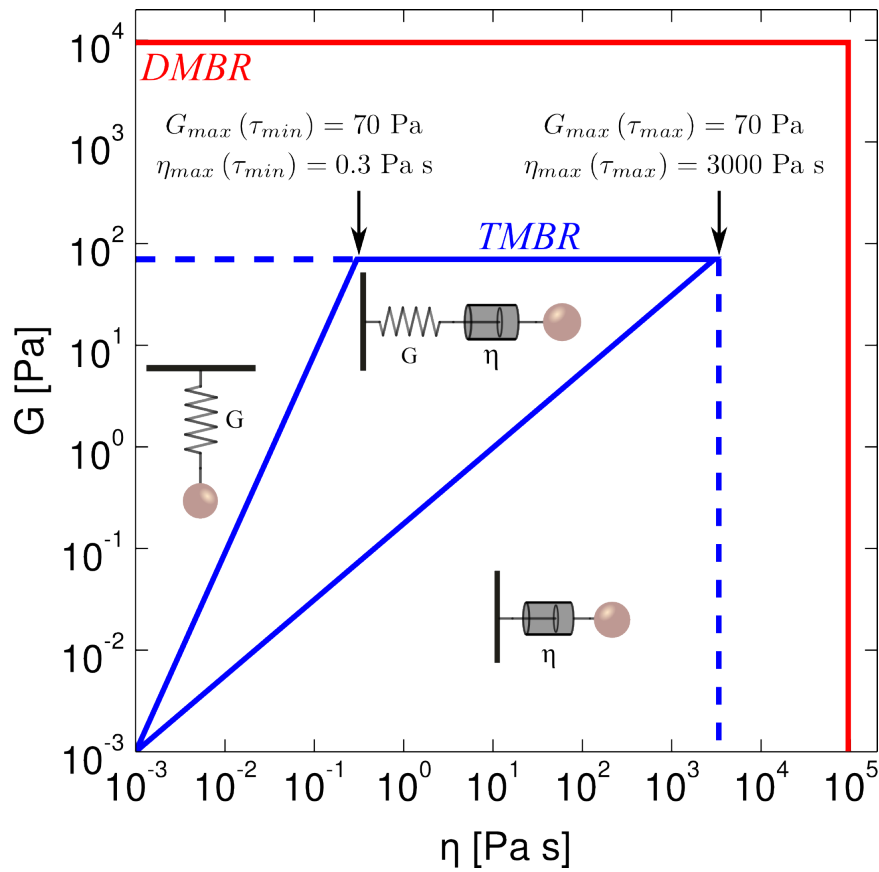


Figure 3.19: Limits of Measure for TMBR

While referring to the limits for TMBR in 3DFM, pictured in Figure 3.19, it is important to note that in the leftmost region we can still measure G . Presumably, if the probed material is a viscoelastic liquid at long time scales, the slope of the MSD would roll up to equal 1 and reveal viscous-only modes, but the 3DFM would be unable to detect it. Similarly, in the bottom-right region of Figure 3.19, the instrument can measure viscosities that range up to 3000 Pa s, but the roll-off for the elastic behavior happens at time scales so short we cannot measure them. Incidentally, there is no lower bound to G and η with respect to diffusion measurements as we can always lower the

magnification in the microscope or increase the probe size, provided the probe remains in the same length-scale regime relative to the polymer solution. In addition, liquids only extend down to $\sim 10^{-4}$ Pa s in viscosity.

3.5.2 Driven Methods

DMBR methods sample a larger range of material parameters, including nonlinear effects through the application of the external force. To determine the limits of measure for DMBR, we use the same video system parameters as for the thermal methods, but add the magnitude of the applied force as well as the time scale that corresponds to the duration the magnets are turned on, applying force to the system here 10 s. We use the Maxwell model, pictured in Figure 2.5(a) along with its strain response, to calculate an idealized viscoelastic fluid response, which responds instantaneously to an applied force followed immediately by a constant velocity. We extract G and η from the instantaneous displacement and constant velocity, respectively.

Our measurement of G is constrained by the minimum elastic displacement we can measure, pulling at maximum force. As stated before, our tracking resolution is ~ 5 nm. The measurement of η is constrained by the minimum detectable bead velocity which corresponds to pulling at maximum force. Our minimum detectable bead velocity is 0.5 nm/s. Assuming a maximum applied force of 2 nN and a 4.5 μm bead, we reach a signal to noise ratio of one with a maximum G of 10 kPa and a maximum η of 100 kPa s. Increasing the range of measurement for G and η would require a lower spatial resolution in acquired video. The upper bound on η could also be enhanced by

increasing the frame rate.

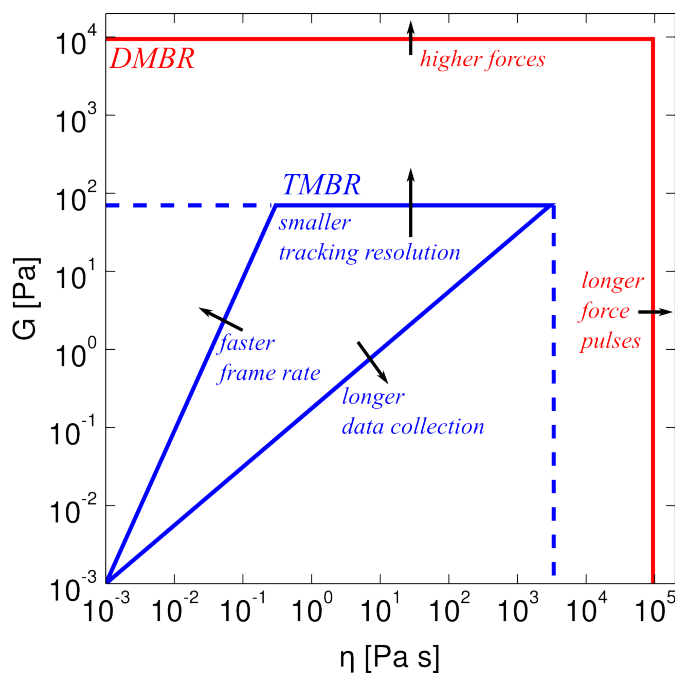


Figure 3.20: Limits of measure for thermal and driven microrheology experiments in the 3DFM

3.5.3 Measurements of Selected Biopolymer Systems

Shown in Figure 3.21 are several microrheology measurements for varying materials, most of which are biopolymer systems. Mechanical properties for cell membranes (b) were measured by (Bausch et al., 1999) with another magnetic tweezers system while (Gardel et al., 2003) measured entangled solutions of actin (a) with 1 & 2 particle thermal methods. Remaining data shown as (c) are all measurements our lab conducted, while the elastin measurements were done at the macroscale by Dana Nettles from Duke (*personal communication*). As a control, Karo syrup was measured successfully

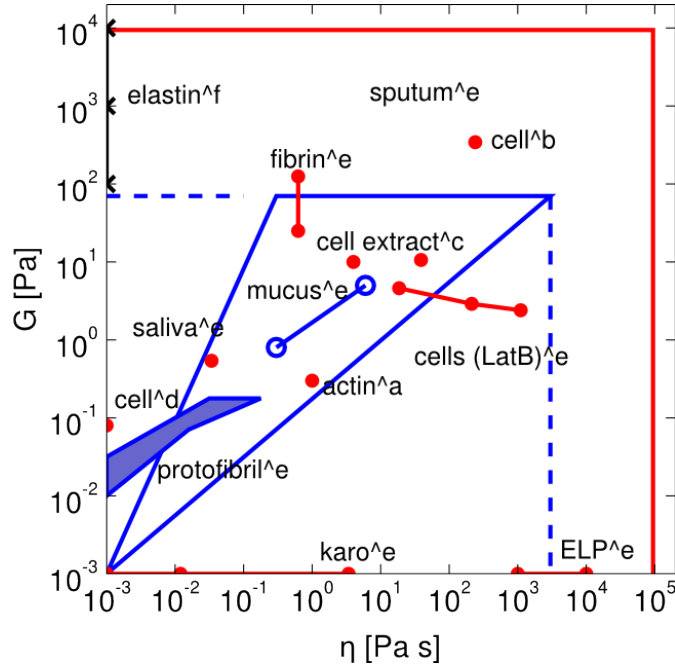


Figure 3.21: Shown is a range of biomaterials measurable with TMBR and/or DMBR. Open, blue circles denote TMBR data/limits while closed, red circles denote DMBR data/limits. The black X's for elastin are data collected by Dana Nettles at Duke with parallel plate rheometry, a common macroscale technique similar to CAP (*personal communication*).

as a Newtonian fluid with viscosity of 3.4 Pa s.

Protofibril samples comprise a solution of polymerizing fibrin before the clot has fully formed. Due to the breadth of parameter space for clotting conditions, protofibril solutions sweep out a wide area of this parameter space, shown shaded in blue. Estimates of fibrin microrheology used a clotted fibrin gel that stiffens over a period of ~ 30 times the clotting time.

Saliva was sampled from one donor. Cells and cellular debris were removed via centrifugation. The measurement shown here was done with DMBR and represents one pull from one specimen. The DMBR data obtained from the sputum sample was collected from a patient at UNC Hospitals afflicted by COPD. HBE Mucus was

concentrated from cell culture washings at 2.5% and 8% and tested via TMBR.

3.6 Predicting Force Requirements

Now that we can measure time, displacement, force, modulus, and viscosity with some reliability, it would be nice to approximate the forces required to observe these quantities for any material by using previous values found in the literature. As explained in Section 2.2.7.2, the drag force on a particle is generalized by $F = \beta\eta v$ where β is a shape prefactor known for specific geometries. For a sphere, the geometric prefactor is $\beta_s = 6\pi r_s$.

In Section 2.2.7.3, I assumed Stokes flow along the surface of a sphere and derived the fluid's shear rate which reaches its maximum 90° from the direction of flow and is equal to $\dot{\gamma} = 3v/\sqrt{2}r_s$ (Eq. 2.47). Substituting this in for the velocity of the sphere, v , results in a force equation that is a function of shear rate:

$$F = \frac{\sqrt{2}\beta_s a \eta \dot{\gamma}}{3} \quad (3.11)$$

For the sphere, substituting in the geometric prefactor $6\pi a$ for β_s gives us a force-viscosity relationship in terms of shear rate:

$$F = 2\sqrt{2}\pi r_s^2 \eta \dot{\gamma} \quad (3.12)$$

Many non-Newtonian fluids experience shear thinning where the fluid viscosity de-

creases with an increase in shear rate. The Carreau model describes a shear thinning fluid whereby the viscosity as a function of shear would be

$$\eta(\dot{\gamma}) = (\eta_0 - \eta_\infty)[1 + (\lambda\dot{\gamma})^m]^{(n-1)/m} + \eta_\infty \quad (3.13)$$

where λ is the thinning time constant, $(n - 1)$ is the power-law slope, and m describes the width of the shear thinning regime.

If one further assumes that the medium surrounding the sphere is a shear thinning fluid (like DNA) and follows the form of a Carreau model, the force-viscosity relationship then depends on the shear rate and is equal to

$$F = 2\sqrt{2}\pi a^2 \eta [(\eta_0 - \eta_\infty)[1 + (\lambda\dot{\gamma})^m]^{(n-1)/m} + \eta_\infty] \quad (3.14)$$

In Section 2.2.8.2 I provided the drag coefficient for a rod moving in the direction of its easy axis as Equation 2.59. The force follows the general form shown above for the sphere, i.e. $F = \beta_c \eta v$ which is linear in η and, as always, still reduces to $F = fv$. The fluid's maximum shear rate along the surface of a rod moving in the axial direction was approximated in Section 2.2.8.3 as

$$|\dot{\gamma}_{top}| = \frac{2\sqrt{2}U}{b(-1 + \ln 4 - 2 \ln p)} \quad (3.15)$$

where p is the aspect ratio, U is the rod velocity, and b is the radius of the rod.

Just as in the sphere example, we assume that the viscosity is shear rate dependent

and the medium experiences shear-thinning at high shear rates

$$F = \frac{\sqrt{2}\pi L r_c \dot{\gamma}_c (1 - \ln 4 + 2 \ln p)}{2 (v_{\parallel} + \ln p)} \eta(\dot{\gamma}) \quad (3.16)$$

and follows the form of a Carreau model, resulting in a final force-viscosity relationship that depends on the shear rate

$$F = \frac{\sqrt{2}\pi L r_c \dot{\gamma}_c (1 - \ln 4 + 2 \ln p)}{2 (v_{\parallel} + \ln p)} \eta(\dot{\gamma}) [(\eta_0 - \eta_{\infty}) [1 + (\lambda \dot{\gamma})^m]^{(n-1)/m} + \eta_{\infty}] \quad (3.17)$$

Shown in Figure 3.22 is a plot that depicts the shear thinning rheology for a 4% PGM solution as measured by CAP. Using the relationships derived here the macroscale rheology information can provide us with expected force requirements at the microscale for a range of bead sizes. Predictions of required forces for the rod geometry are demonstrated in Figure 5.8.

3.7 Conclusions

Here I demonstrated the efficacy of the 3DFM as an instrument for microrheology measurements of biopolymer systems which have different needs than the measurements at the macroscale, but can also provide more insight regarding the interactions between a polymer system with micron-sized length scales and a probe of similar size. We started saying that to make measurements of the noise of our tracking system. In this chapter I demonstrated the 3DFM's ability to measure viscoelastic parameters using both passive

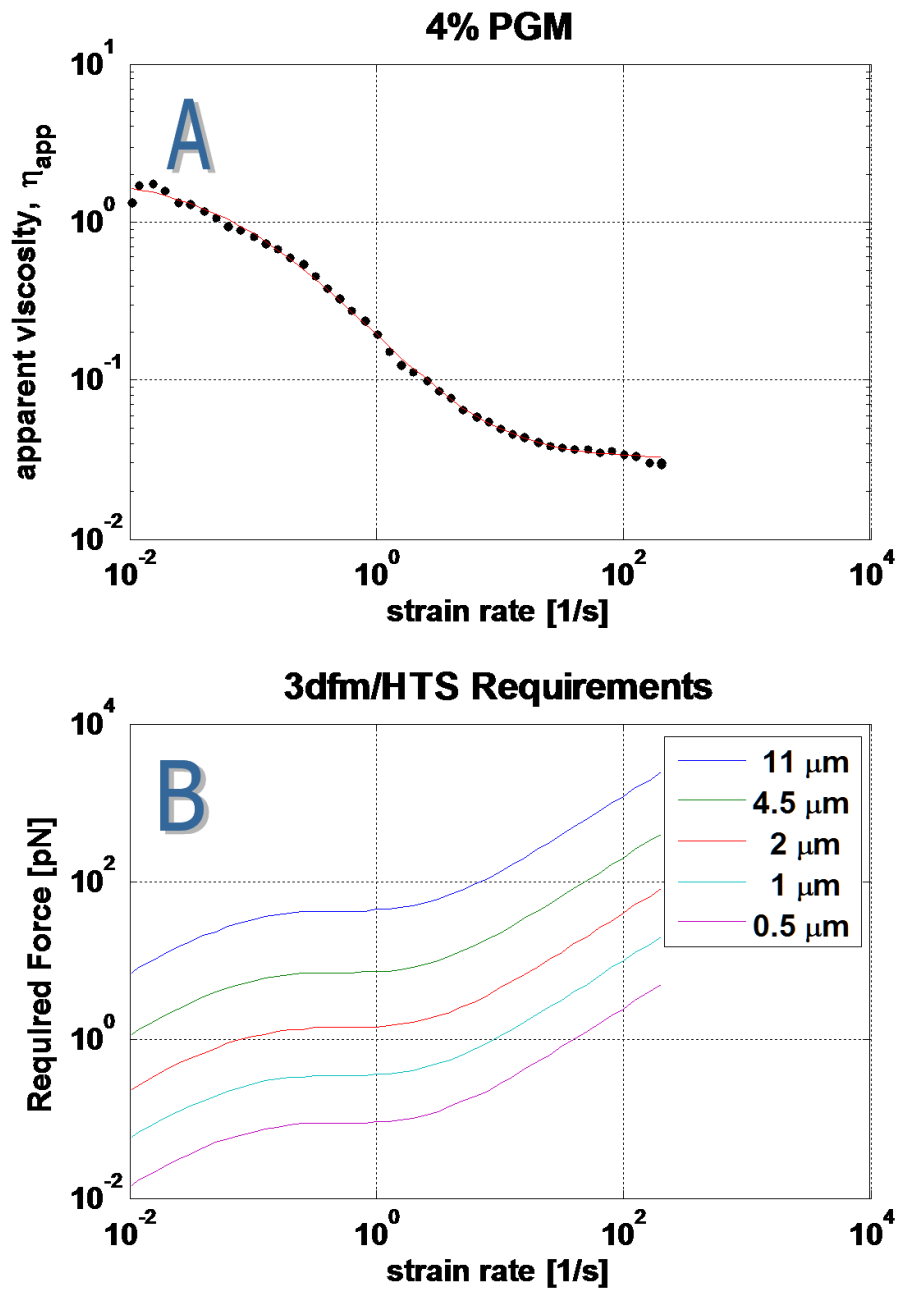


Figure 3.22: Force requirements to pull beads of varying diameter through porcine gastric mucus at any defined strain rate, $\dot{\gamma}$.

and active microrheology techniques.

Chapter 4

Multiscale Rheology of selected biofluids

4.1 Overview

In Chapter 3 I surveyed 3DFM hardware, reviewed the literature, and provided the methodology for TMBR and DMBR experiments. Here I report on my polymer systems of interest, DNA, HA, PGM, and guar as simple solutions and mucus and sputum as solutions of direct biological origin. For each simple polymer system I determine its salient polymer physics parameters and present new macroscale and microscale results that supports great correspondence between the two techniques. I also present similar rheological measurements for mucus and sputum.

Each biofluid I used had been tested in the literature and had its own unique characteristics that made it an interesting choice for testing in microbead rheology. λ -DNA is a monodispersed polyelectrolyte and has the highest persistence length. The rheology of DNA is physiologically relevant to MCC because it is found in high concentrations

in purulent sputum (Rubin, 2006). HA is a softer polyelectrolyte found throughout the body, is homogeneous in reagent form, and is the smallest and shortest of the four. Guar is a neutral molecule of plant origin often used in foods as a thickening agent (Imeson, 1999). It shares similar rigidity to HA but has a much larger degree of polymerization, N , and had early success as a mucus simulant albeit showing limited MCC (King and Macklem, 1977). Finally, the PGM I used should be the simulant closest to a real mucus. Using dynamic light scattering (DLS) I found its molecules quite large and a L_p calculated from the DLS data showed that it shared similar stiffness to the model λ -DNA solution.

In summary, λ -DNA solutions probed with 1 μm and 2.8 μm beads had low apparent viscosities because of shear thinning around the probe at relatively large shear rates, a phenomenon previously unreported for a biological fluid at the microscale. HA solutions show a linear viscoelastic response when tested with 2.8 μm beads resulting in a constant steady-state viscosity of 10 Pa s, consistent with cone and plate. Previously unseen in the literature, measurements of microscale shear thinning are new to the community. PGM and guar specimens also show signs of shear thinning, but with a larger spread in the data, presumably due to solution or polymer system heterogeneities. All solutions show acceptable agreement when their viscoelastic properties are compared with the macroscale cone and plate testing.

4.2 Polymer systems

Four possible states exist for polymer systems: elastic, semicrystalline, glass, and viscous. Elastic polymers are solid-like and typically contain a large number of crosslinks per chain and as a result have high elasticity. Semicrystalline systems are also more solid-like but contain crystalline regions intermixed with amorphous ones. Glasses are amorphous polymer systems utilized at temperatures below the glass transition temperature, T_g , where the chains only move with respect to each other at monomer length scales and no larger (Rubinstein and Colby, 2003).

Three polymer system types are typically interpreted as being solid-like because they exhibit elastic responses when subjected to a stress. When the recovery of the elastic response is complete and instantaneous (within the length-scale and time-scale error of the instrument) that material is considered “solid.” A non-zero time constant indicates viscous modes in the material response, and is a viscoelastic solid (Rubinstein and Colby, 2003). A polymer solution is in its viscous state when its temperature exceeds T_g and no crosslinking exists between strands. Polymer systems in this state exhibit lossy recovery because the viscous element relaxes during the application of stress (Rubinstein and Colby, 2003). All of the polymer systems I examine in detail in this work are in the soft, viscous state.

I prepared HA, PGM, and guar solutions by adding each material in powder form to its appropriate buffer and using vortex addition (See Appendix A.4 for details). All solutions were left to rotate at slow speeds and equilibrate overnight at 4°C before

performing any rheology studies. Polymer physics information for all of these solutions can be found summarized in Tables 4.1 and 4.2. Briefly, all solutions were at concentrations that placed them in the entanglement regime except for HA at 10 mg/mL which instead was semi-dilute, unentangled.

–	units	λ -DNA	HA	PGM	Guar
R_g	nm	500	115	310	425
R_0	nm	1270	282	760	1040
l_p	nm	50	8	36	10
b	nm	100	16	72	20
N_b	–	165	310	111	2700
l_c	μm	16	5	8	54
M_w	MD	32	1.5	56	50
M_b	kD	197	5	500	18
c^*	mg/mL	0.08	0.83	0.75	0.26
ϕ^*	–	9e-5	1.2e-5	3e-4	2.5e-4
τ_0	s	7.8e-5	3.2e-7	2.9e-5	6.2e-7
τ_R	s	2.1	0.012	0.4	4.5

Table 4.1: Summary of intrinsic polymer system modeling parameters.

–	units	λ -DNA	HA	PGM	Guar
c_{work}	mg/mL	1.4	10	40	12
ϕ_{work}	–	0.002	0.001	0.018	0.012
P	–	17.5	12	54	46
regime	–	SD,EN	SD,UN?	SD,EN	SD,EN
Ge	–	0.9	140	1.2	40
Me	MD	3.9	0.14	83	0.9
Ne	–	8	11	1	54
Z	–	20	18	164	50
a	nm	285	54	59	147
$Kn(1\mu\text{m})$	–	0.28	0.05	0.06	0.15

Table 4.2: Summary of extrinsic polymer system modeling parameters.

4.3 DNA

DNA is the biomacromolecule that comprises the genetic code of an organism as a varying sequence of four different nucleotides, adenine (A), cytosine (C), guanine (G), and thymine (T). These nucleotides are the constituent monomers of a DNA polymer strand, classifying DNA as a heteropolymer as it has more than one monomer type. In solution, DNA is a viscous type polymer, because it will, exhibit liquid-like behavior at long time scales ([Rubinstein and Colby, 2003](#)).

In 1953 James Watson and Francis Crick, with the first accurate structure of DNA, reported the axial distance between base pairs in the DNA strand to be 3.4 Å with a strand diameter of 2 nm, resulting in a monomeric cylindrical volume of 1.1 nm³ for each base pair. The molar mass for an average of the available base pairs is 660 g/mol ([Watson and Crick, 1953](#)). The contour length of a polymer strand is simply equal to the number of monomers (bp) multiplied by the axial distance between monomers, or $L_c = L_{ax}N_{bp}$.

I used λ-DNA in these experiments. λ-DNA is derived from the λ-bacteriophage, a virus that injects its genetic code into a host bacterium. It is commercially available in large quantities for relatively low cost. It has 48502 base-pairs (bp) and comes from the manufacturer in a linearized form with 12 unpaired base-pairs at each end. Because each base-pair has an average molar mass of 660 g/mol, the λ-phage DNA strand has a molecular weight of 32 MD. Because it has axial distance between each bp of 3.4 Å, it must have a contour length of 16 μm per strand.

Polymer	L_p	Reference
HA	8 nm	(Buhler and Boue, 2004)
Guar	10 nm	(Morris et al., 2008)
MUC5AC	10 nm	(Round et al., 2002)
DNA	50 nm	(Rubinstein and Colby, 2003)
Fibrin	5 μm	(Guthold et al., 2007)
Actin	15 μm	(Howard, 2001)
Microtubules	6 μm	(Howard, 2001)

Table 4.3: Persistence lengths for several biopolymers.

The measure of stiffness for a polymer is its persistence length, L_p , a function of its flexural rigidity that describes the distance over which the direction of the polymer backbone becomes uncorrelated (Rubinstein and Colby, 2003). The source of the bending in the polymer is thermal forces, making it also dependent on the temperature of the solution. $L_p = EI/kT$, where E is the Young’s modulus and I is the second moment of inertia for a slender rod, or $I = \pi r^4/4$ for a circular cross-section. The persistence lengths for many polymer systems have been measured, with some shown in Table 4.3.

To be predictive for λ -DNA as a polymer solution, we must first determine whether it exists as a neutral molecule or a polyelectrolyte whilst in its TRIS-EDTA buffer (10 mM Tris-HCl (pH 7.4), 5 mM NaCl, 0.1 mM EDTA, and 0.05% Sodium Azide). The pK_a for the phosphate backbone is such that the typical base pair in a 7.4 pH buffer has a net charge of -2 .

Because λ -DNA exists as a polyelectrolyte, we must determine the ionic strength of the solvent and the polymer Debye screening length to determine whether the molecule interacts with itself or adjacent polymers because of the exposed charge. The Bjer-

rum length, L_B , describes the distance where the interaction between two elementary charges, e , would be equal to thermal energy kT in a solvent with a dielectric constant, ϵ (Dobrynin and Rubinstein, 2005). In SI units

$$L_B = \frac{e^2}{4\pi\epsilon_0\epsilon kT} \quad (4.1)$$

where ϵ_0 is the permittivity of free space, equal to $8.85 \times 10^{-12} \text{ C}^2 \text{ N}^{-1} \text{ m}^{-2}$. For the λ -DNA solution described here the L_B is approximately 7 Å. At distances less than L_B the energy of kT is insufficient to stop the recruitment of counterions from the surrounding buffer to charged regions on the polymer molecule.

As stated earlier, the ionic strength, I_c , of the buffer solution also bears great impact on the screening of charge in polyelectrolyte solutions. Equal to

$$I_c = \frac{1}{2} \sum_i c_i z_i^2 \quad (4.2)$$

where i is an index of charged species in the buffer, c is the species concentration, and z its elementary charge. I_c for this DNA buffer is 8 mmol kg⁻¹. Finally, the Debye screening length, L_d , identifies the distance at which a charged species on a macromolecule “sees“ another charged species, and as such uses both L_B and I_c

$$L_d = \sqrt{\frac{1}{8\pi N_A L_B I_c}} \quad (4.3)$$

where N_A is Avogadro’s Number (Dobrynin and Rubinstein, 2005). L_D for the λ -DNA

solution used here is about 4 nm, much smaller than the inherent stiffness of a polymer with an L_p of 50 nm.

Finally, to determine the solvent conditions for λ -DNA in TE buffer, I must calculate the size of the thermal blob, L_T , which is

$$L_T = L_p \left(\frac{L_p^3}{V_x} \right)^2 \quad (4.4)$$

where the excluded volume, V_x , per chain segment, is

$$V_x = L_p^2 L_d \quad (4.5)$$

making L_T finally equivalent to

$$L_T = \frac{L_p^3}{L_d^2} \quad (4.6)$$

For λ -DNA in TE buffer, the thermal blob size is about 10 μm , about two-thirds the size of the chain's L_c . Such a result lies on the boundary between ideal and real chain representations of the λ -DNA strands in solution. For the purposes of the work shown here, I have assumed the λ -DNA chain is not swollen in solution and as such resides as an ideal chain in θ -solvent conditions.

The simplest physical model that describes a polymer system is the Gaussian (or Ideal) chain model, of which there are several types: freely jointed chain (FJC), freely rotating chain (FRC), worm-like chain (WLC), hindered rotation (HR), and rotational isometric state (RIS). In the literature DNA is modeled as a WLC, a good model for

polymers with moderate stiffness. Technically, the WLC is a special case of the FRC model, where the bond angle, θ , is small and the contour length is larger than the polymer's characteristic stiffness (Rubinstein and Colby, 2003).

In Section 2.3, I defined particle diffusion in the context of a temporal random walk. Similarly, the geometry for an ideal polymer chain is a random walk, but in space rather than time, where the characteristic step size is governed by the stiffness of the polymer strand. The convenient value is no longer the RMS displacement as a function of the mean time to escape. Rather, it is now the RMS end-to-end vector of the polymer path, which defines the straight-lined average vector distance from the beginning of a typical polymer to its other terminal end, equal to

$$\langle R_o \rangle = b\sqrt{N} \quad (4.7)$$

where b is the Kuhn length and N corresponds to the number of Kuhn segments that exist in each polymer chain. For the WLC, $b = 2L_p$ and is the length at which successive Kuhn monomers follow a random walk in space (Rubinstein and Colby, 2003).

I chose to use λ -DNA as a model polymer system because its shear rate and frequency dependent rheology profile is well documented in the present body of literature (Teixeira et al., 2007; Heo and Larson, 2005; Mason et al., 1997; Mason and Weitz, 1995). Additionally, λ -DNA is found in prodigious amounts in pathological sputum, its prevalence responsible for altering sputum rheological properties (Rubin, 2006). Lastly, the rheology of entangled $\lambda - DNA$ solutions is easily measured by the magnetically-

driven microbead rheometry capabilities of our magnetic tweezers system, the 3DFM (Fisher et al., 2006b).

To prepare solutions of λ -DNA (Invitrogen, Carlsbad CA), I first had to anneal one of the single-stranded, hanging ends with a complementary 12 base pair oligonucleotide (UNC oligonucleotide synthesis facility, Chapel Hill NC). This step prevented the formation of cyclic DNA and minimized potential solution heterogeneity (Braun et al., 1998). A more detailed version of the protocol used to prepare the λ -DNA solution is in Appendix A.5. A solution of λ -DNA reaches its overlap concentration at 0.07 mg/mL, and its entanglement concentration is roughly 10 times that at 0.7 mg/mL (Zhu et al., 2008). PEGylated beads with 1 μ m or 2.8 μ m diameters were mixed in the DNA storage buffer and used to dilute the λ -DNA to the tested concentrations of 2.4 mg/mL and 1.44 mg/mL. Mixing the beads into the solution was done via short vortex bursts of 2 s over a 2 minute period. λ -DNA solutions were stored at 4 °C and allowed to equilibrate at least overnight before rheology experiments.

I checked for non-specific adsorption of λ -DNA to the particles, which might confound driven transport, by imaging suspensions of particles dispersed in λ -DNA, fluorescently labeled with YOYO-1 (data not shown). Observing no significant increase in fluorescence near these particles indicates little λ -DNA adsorption.

4.3.1 CAP

Extensive CAP measurements on λ -DNA solutions provided useful parameter estimates for subsequent studies. For the stress amplitude sweep shown in Figure 4.1

the CAP oscillates at a single frequency ($\omega = 1$ rad/s) and increases the stress amplitude in steps. The primary reason for performing the stress amplitude sweep is to determine the linear range for the tested material, where an increase in stress results in a corresponding and proportional increase in strain. This region corresponds to a range of strain where the resulting modulus is flat, with zero slope. Once the linear response range is determined for a material at high frequency, one can better choose the strain/stress amplitude and frequency range for the frequency sweep. This practice ensures the collected data for the frequency sweep is in the linear regime.

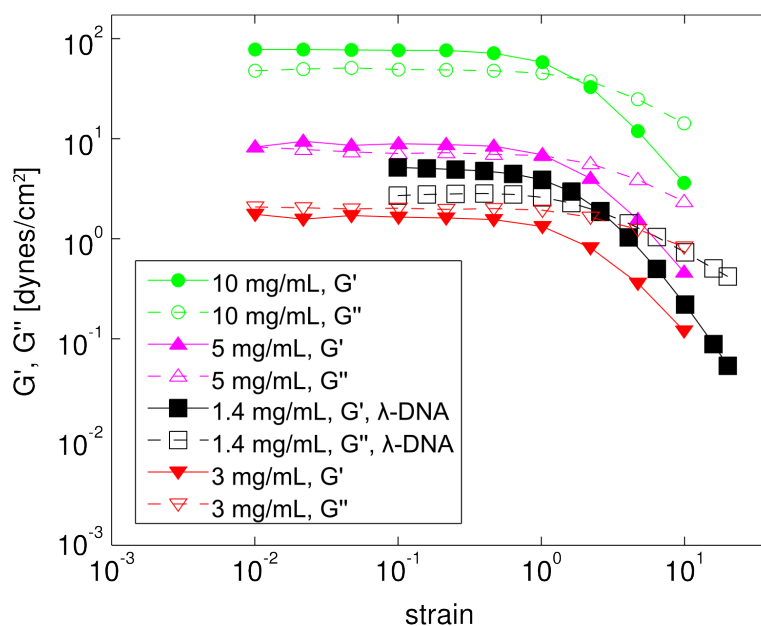


Figure 4.1: Shown here plotted alongside literature values for calf-thymus DNA (Mason et al., 1998) is the strain amplitude response for 1.4 mg/mL λ -DNA ($G'(\omega)$ ■, $G''(\omega)$ □) tested by the AR-G2 CAP controlled-stress rheometer at a constant frequency of $\omega = 1$ rad/s.

All data shown in Figure 4.1 for calf thymus DNA are from (Mason et al., 1998) while the λ -DNA is our formulation. Calf thymus DNA has a shorter contour length

of 4.5 μm compared to λ -DNA at 16 μm . Both DNA solutions used here are in the entangled regime where the dominant length scale is the tube diameter, meaning that G should be independent of both M_w and L_c . As such, I should expect the 1.44 mg/mL λ -DNA solution to have lower shear moduli, with G'' being the greater of the two. This discrepancy in the rheological response occurs due to a confluence of differences in the testing. The calf-thymus DNA was tested at 25 $^{\circ}\text{C}$ while the λ -DNA was tested at 23 $^{\circ}\text{C}$. The calf-thymus DNA was tested at a pH of 7.9 while the λ -DNA was tested at a pH of 7.4. Finally, the ionic strength of the buffer for the calf-thymus DNA was more than 10x the λ -DNA buffer, meaning the calf-thymus chains are easily ideal chains, while, as described in the previous section, the λ -DNA chains are only marginally ideal.

With these caveats in mind, I consider that the resulting rheology values for λ -DNA are consistent with the literature values. Additional stress sweeps were done at 10 Hz with linear strain responses at 10% strain or less (not shown).

Two separate CAP rheometers were used to check the linear frequency response for two different preparations of 1.44 mg/mL λ -DNA. Both instruments showed similar responses with less than 10% difference at frequencies less than 10 Hz (Fig. 4.2) denoting the reliability of the λ -DNA solution preparation and of the CAP protocols I used. Dissimilar responses at frequencies higher than 10 Hz occurred due to instrument inertia. Consistency exists between the amplitude sweep data in Figure 4.1 and the frequency sweep in Figure 4.2. The zero-shear linear viscoelastic response in the amplitude sweep intersects the frequency sweep at the appropriate frequency (labeled as *stars* in Figure 4.2).

Besides a consistency check, the frequency sweep provides information regarding material properties. For entangled solutions, the plateau modulus, G_e , appears as a flat region in $G'(\omega)$ at intermediate frequencies, and corresponds to time scales where the material exhibits a solid-like response. Knowing the plateau modulus allows one to calculate the molar mass of the entanglement strand, M_e ,

$$G_e = \frac{\rho RT}{M_e} \quad (4.8)$$

where R is the universal gas constant, equal to $8.31 \text{ J mol}^{-1} \text{ K}^{-1}$. For the 1.4 mg/mL λ -DNA solution, G_e occurs at $G'(\omega) \sim 0.9$, which corresponds to an M_e of 3.9 MD . To determine the number of Kuhn monomers per entanglement strand, N_e ,

$$N_e = \frac{M_e}{M_b} \quad (4.9)$$

where M_b is the molar mass of a Kuhn monomer. This λ -DNA solution has $N_e \approx 8$. The number of entanglements per strand, Z , is just the ratio of Kuhn monomers in an entire polymer chain compared to the number within an entanglement strand,

$$Z = \frac{N}{N_e} \quad (4.10)$$

For the test solution of λ -DNA, Z results in approximately 20 entanglements per chain.

Finally, the confining tube diameter, a , used in the Doi-Edwards tube model is

$$a = bN_e^{1/2} \quad (4.11)$$

for ideal chains (Rubinstein and Colby, 2003). This relationship results in a tube diameter of 285 nm for the 1.4 mg/mL λ -DNA test solution.

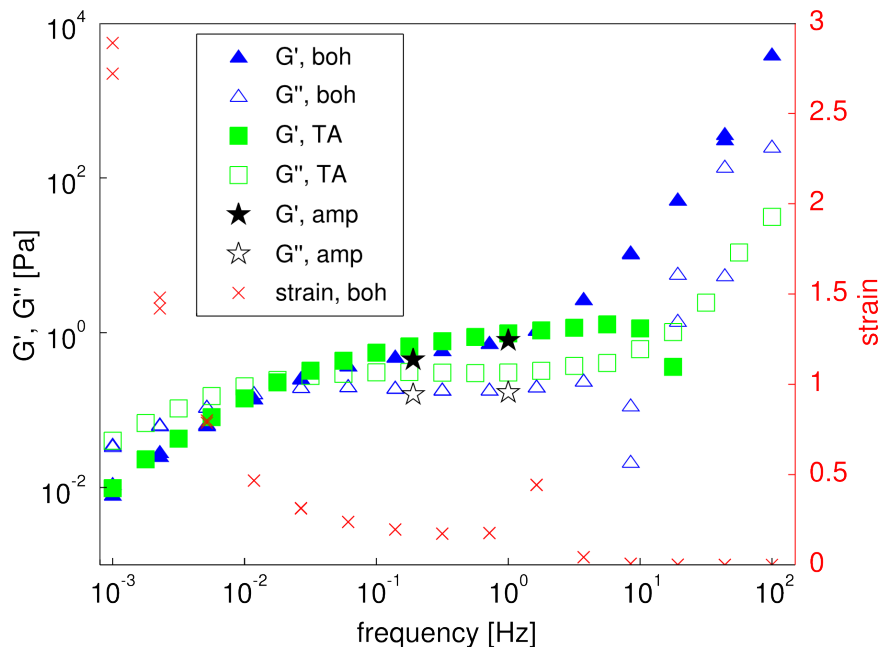


Figure 4.2: I used two different CAP rheometers to test the frequency-dependent modulus of two different formulations of 1.4 mg/mL λ -DNA. The Bohlin Gemini ($\blacktriangle, \triangle$) and the TA AR-G2 (\blacksquare, \square) show very similar responses below 10 Hz. Above 10 Hz, inertia begins to dominate the response, as seen by the sudden loss of measurable strain (\times). Steady state strain amplitude sweep values from Figure 4.1 are shown as \star at the appropriate frequencies and provide supporting evidence the response is linear.

CAP steady-state flow measurements were also performed on λ -DNA specimens, where the unidirectional shear rate increases in steps while the stress is measured. The rheometer waits for a steady shear rate before recording the apparent viscosity value.

Shown in Figure 4.3 are the shear thinning profiles for solutions of λ -DNA at varying concentrations. Data for 0.7 mg/mL and 1.4 mg/mL were my formulations while data for those concentrations less than 0.7 mg/mL were from work done by Heo and Larson (Heo and Larson, 2005). Later, in Chapter 5, I compare these CAP results to shear-thinning data found while driving rod-shaped microparticles in the same solutions.

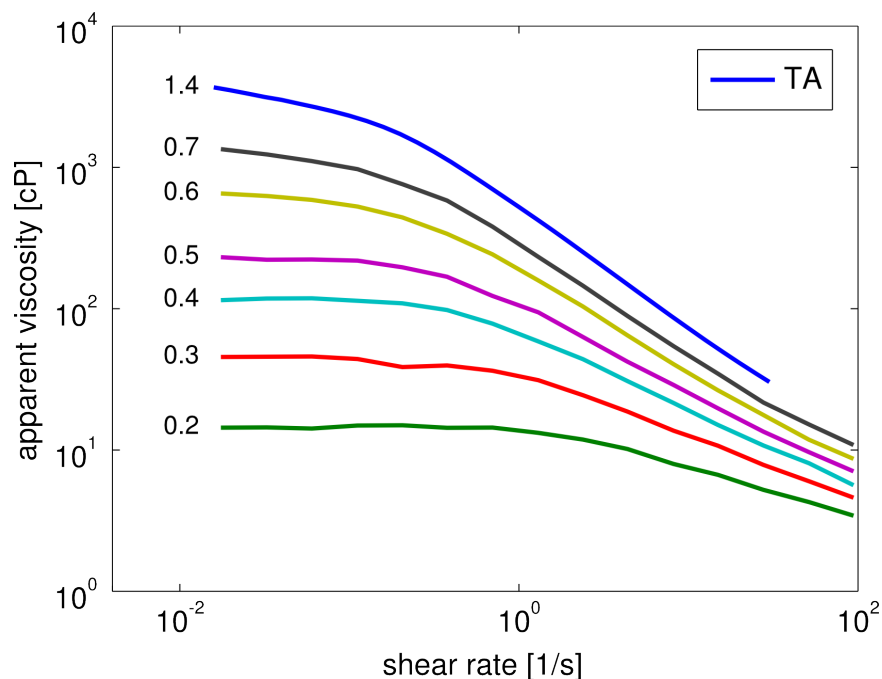


Figure 4.3: λ -DNA solutions shear thin when subjected to sufficient shear rates. Data shown in this figure are CAP taken from (Heo and Larson, 2005) for 0.72 mg/mL and lower concentrations. I obtained data for the 1.4 mg/mL solution with our CAP instrumentation. I also tested the 0.72 mg/mL concentration with the data accumulating less than 8% error from the literature values.

4.3.2 TMBR

My first microscale rheology measurements used Thermal Microbead Rheology (TMBR) to measure the mean square displacement (MSD) of 500 nm and 1 μ m beads

embedded in solutions ranging from buffer to 1.44 mg/mL λ -DNA. The DNA buffer (10 mM TRIS, 5 mM NaCl, 0.1mM EDTA) is a Newtonian fluid with a viscosity of 2–3 cP, slightly higher than that of water under the same conditions. Newtonian fluids present an MSD function that has a constant slope equal to one for all timescales, shown schematically in Figure 2.4, and experimentally in Figure 4.4.

As the concentration of λ -DNA increases, the expected slope of one found in the Newtonian buffer solution begins to decrease to a shallower value at moderate τ . At long τ the MSD for all of the λ -DNA solutions converge to viscous only modes and as such have slopes equal to one.

Chains of λ -DNA have an overlap concentration, c^* , of 0.07 mg/mL. The first λ -DNA solution tested and shown in Figure 4.4 had a concentration of 0.14 mg/mL, or $2c^*$. Even at this semi-dilute concentration, before the chains entangle, there is a slight shift in the linear character in the solution MSD at a τ of 0.3 s. This slight decrease in the slope indicates an increase in the modulus of the solution, due to chains interpenetrating, increasing the free energy of each chain above the background entropic value.

Increasing the concentration of λ -DNA to 0.7 mg/mL corresponds to $10c^*$, which is on the boundary between the unentangled and entangled polymer regimes. The MSD function for this solution, also shown in Figure 4.4, has a distinct decrease in slope from the Newtonian value of one at τ ranging from 0.01 – 3 seconds. These time scales correspond to the beginning signatures of this polymer system’s plateau modulus in the frequency response (not shown).

Increasing the λ -DNA concentration even further to 1.4 mg/mL, or $20c^*$, continues to reduce the MSD slope and expands the time scales at which the system is viscoelastic. The plateau modulus for this solution presents itself in the frequency sweep, explored and discussed in detail in Figure 4.2. Long- τ scales, where the slope converges to one, corresponds to a zero-shear TMBR-obtained viscosity of 2.7 ± 0.2 Pa s, about half of the magnitude at the lowest test frequency, shown in Figure 4.3.

I also tested this solution with smaller, 0.5 μm diameter beads that had the same surface functionalization, obtaining an MSD function that portrayed a long- τ viscosity that was lower by half when compared to the larger 1 μm diameter beads. This discrepancy probably occurs due to solution heterogeneity at bead length scales as because the bead size is close to the solution's tube diameter, approximately 300 nm.

4.3.3 DMBR

For DMBR measurements in λ -DNA, I start with constant, relatively low force, long duration pulls in 1.4 mg/mL λ -DNA where the force was applied for 10 seconds. Plotted in Figure 4.5, the resulting compliance curve reaches the long time, viscous only mode of the polymer system, where the velocity becomes constant. A good fit to the Jeffrey model is overlaid in red and shows the response to be predominately linear, with the exception of small ripples or fluctuations in the bead path, attributed to possible small length-scale heterogeneity in the λ -DNA solution or diffusion of the bead over such long time scales. The recovery distance of the bead is not 100%, which

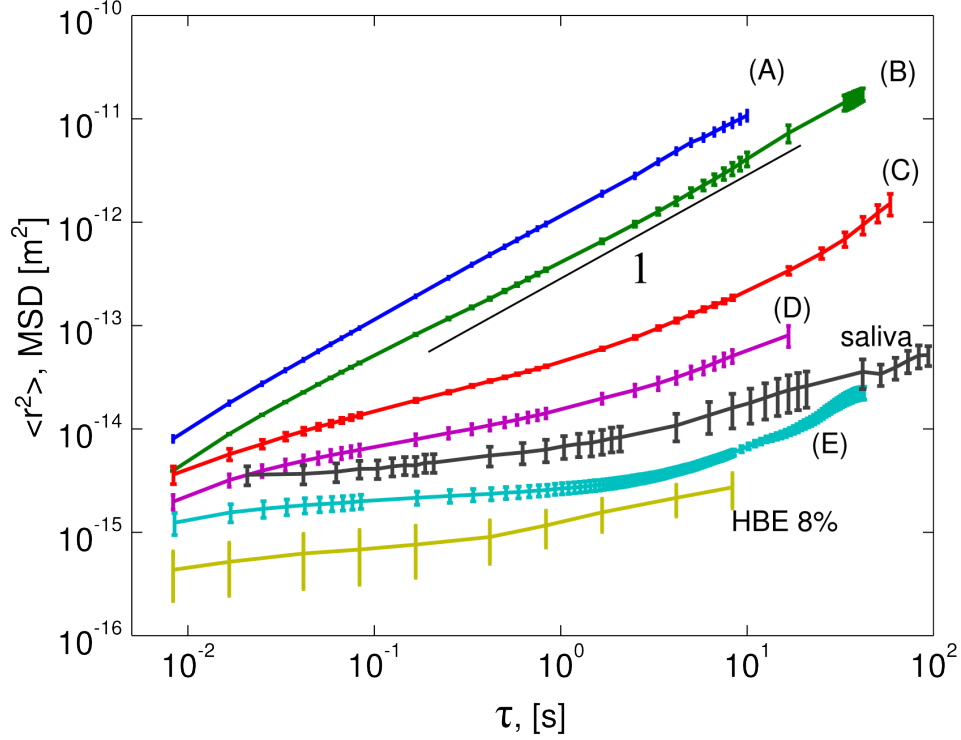


Figure 4.4: Shown here is the dependence of bead mean-square displacement on time and polymer concentration. Beads in buffer show viscous only modes with expected dependence on τ with a power law slope equal to one. Even at 0.14 mg/mL ($2c^*$) there is a slight shift in the primarily linear dependence at $\tau = 0.3s$. As the concentration of λ -DNA increases, the viscoelastic modes become detectable by the diffusing bead. At 1.4 mg/mL, the λ -DNA solution is entangled, with time scales that correspond to a plateau modulus with slope close to zero.

indicates that 1.4 mg/mL λ -DNA is a viscoelastic liquid. With a total relaxation of the imposed stress, the bead reaches a stable and relatively driftless position over time. The suddenness of the elastic response at very early times relative to the pull duration illustrates how the Maxwell model approximation can serve as a limiting case of the Jeffrey model.

Fitting for model parameters during the forced period results in a G of 0.9 Pa and an η_0 of 1.2 Pa s, values that are approximately one-half of the TMBR data and one-

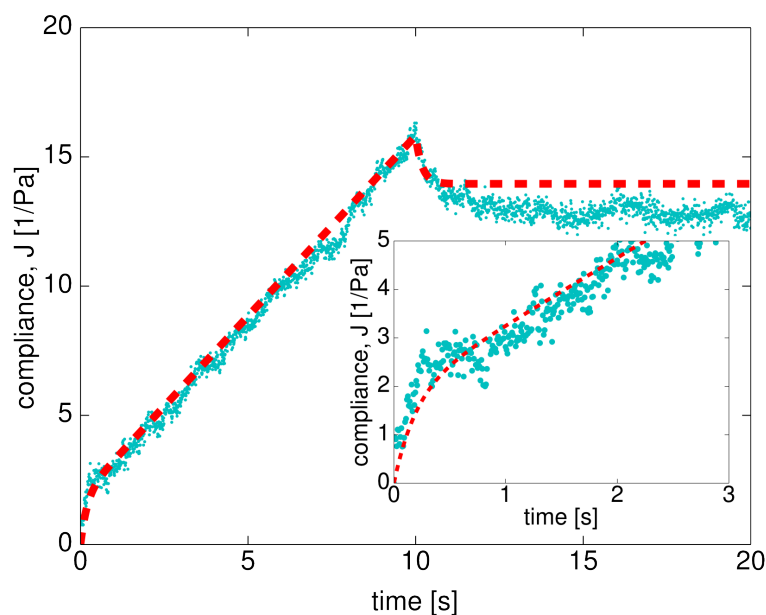


Figure 4.5: Pulling a bead in 1.4 mg/mL λ -DNA with DMBR. Pulling with 2 pN of force, the 1 μm bead reports an η_0 of 1.2 Pa s, and a G of 0.9 Pa, values that agree with the CAP taken and shown in Figure 4.2

quarter of the data collected by the CAP frequency sweep (Fig. 4.2). As described later, the smaller viscosity found in this DMBR experiment is probably due to the higher-shear conditions in the space immediately surrounding the bead. Using the flow measurements seen in Figure 4.3, and the maximum shear rate around the bead for this particular pull (0.05 s^{-1}), the corresponding CAP apparent viscosity is equal to 1.8 Pa s. I also used the Cox-Merz approximation on the TMBR data, setting the shear rate equal to the probed frequency in rad/s, and obtained an apparent viscosity of 1.4 Pa s, within 20% of the DMBR value.

Using these parameters to also model the recovery portion of the data returns a close but not as good fit. Zooming into the early response of the forced period (Figure 4.5, *inset*) reveals an additional systematic deviation from the Jeffrey model. Both of

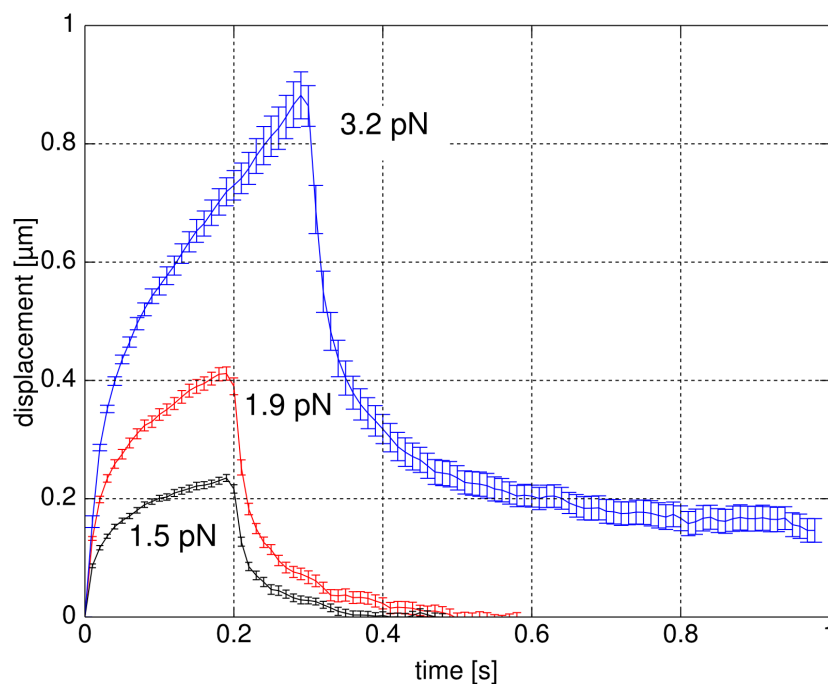


Figure 4.6: Shown with error bars are averaged creep compliance curves taken in 1.44 mg/mL λ -DNA with ≤ 3.2 pN input force where the response appears linear. Data shown input forces of 1.5 pN or 1.9 pN show a linear viscoelastic response with complete recovery. Each curve is an average of multiple sequences, showing good repeatability from pulse to pulse. The 3.2 pN input force data shows a quasi-linear viscoelastic liquid response where the elastic component becomes dominated at long times by a viscous mode equivalent to 0.2 Pa s and does not experience complete recovery upon relaxation.

these deviations indicate that a more complex model, perhaps a Jeffrey model with multiple modes, is required to fit all of the behavior seen in the data.

Figure 4.6 shows the repeatability of successive creep measurements in DMBR when the longest probed time mode is allowed to fully relax. These 1 μ m MyOne superparamagnetic beads were pulled through the 1.4 mg/mL λ -DNA solution under indicated step forces. Quasi-linear creep compliance curves are averages of several pulses of identical parameters. Good control over the DMBR technique combined with a homogeneous, viscoelastic λ -DNA solution produces reproducible results with high signal-to-noise ra-

tio.

When viewed in the context of shear thinning, the viscosities measured by DMBR during forced periods match those generated by CAP and TMBR techniques. Moduli values are also close to CAP and TMBR, provided the duration of the DMBR pull is sufficient to exhaust the “spring” and probe the long-time viscous only mode of the material response. However, these modulus values do not exactly fit data obtained during the recovery period. In addition, the Maxwell and Jeffrey step responses require an incomplete recovery of the rheology probe as seen in the step response equation (Jeffrey shown):

$$J(t) = \frac{1}{G} + \frac{t - t_1}{\eta_2} - \frac{1}{G} \exp\left(\frac{-G(t - t_1)}{\eta_1}\right) \quad (4.12)$$

The second term is nonzero for any $t_1 > 0$ and disappears altogether during the recovery period. This asymmetry in the step response provides a necessary net displacement for any pull duration. In the data shown in Figure 4.6 however, a total recovery with no net displacement is found.

To resolve this contradiction I must concede that Jeffrey or Maxwell models do not accurately describe the DNA response curve seen in Figure 4.6. When pulled with low forces for very short periods of time the bead experiences a full and complete recovery. Is this because there is some inherent difference between the behavior of DNA and the model or is it possible the net displacement is hidden beneath the noise floor of the instrumentation? The pulse duration is 200 ms and the applied force less than 2 pN. The highest viscosity for the 1.4 mg/mL λ -DNA measured by DMBR is 1.2 Pa s. In

these conditions, the net displacement would be approximately 3–4 nm, on the order of the noise level in the tracking software. In these experiments, it appears the reason for the lack of net displacement is indeterminable due to system noise.

An interesting observation about DMBR, and probably concerns all active microrheology techniques, refers to a sensitivity of the probe to specimen history. Shown in Figure 4.7 are the fitted relaxation times for a sequence of constant force DMBR pulls in λ -DNA. Each pull results in an apparent complete recovery of the bead displacement once the external force is removed from the system. As the number of pulls increases, so does the relaxation time of the bead. Even though the bead has returned to its initial position along its previous path, the polymer dynamics become slower, presumably because of the perturbation the bead has imposed on the surrounding material. To compensate for this effect and obtain consistent curve shape and dynamics, the relaxation period must be of sufficient length to relieve the stress still imposed on the strands closest to the bead.

The linear increase in relaxation time does not continue forever, but experiences a sudden drop in magnitude once the bead leaves its initial and immediate environment and probes fresh (not previously probed) material. Such behavior suggests the polymer surrounding the bead has experienced an increase in L_e , generating longer relaxation modes. More discussion about the dynamic properties of this solution can be found in Chapter 6.

Concluding the rheology analysis for λ -DNA solutions is a combination of all three

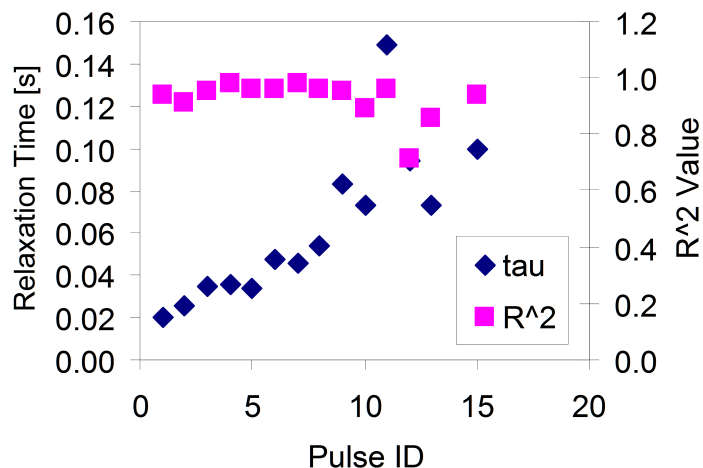


Figure 4.7: Shown as \blacklozenge 's are fitted relaxation times measured for DMBR creep pulls in 1.4 mg/mL λ -DNA. A systematic increase in the relaxation time occurs subsequent to each pull of the bead. Shown in \blacksquare 's are the correlation coefficient (R^2) values. While R^2 is not a conclusive measure of the goodness of fit, most of these values are sufficiently close to one to establish confidence in the trend. Total relaxation occurred for every pulse shown here.

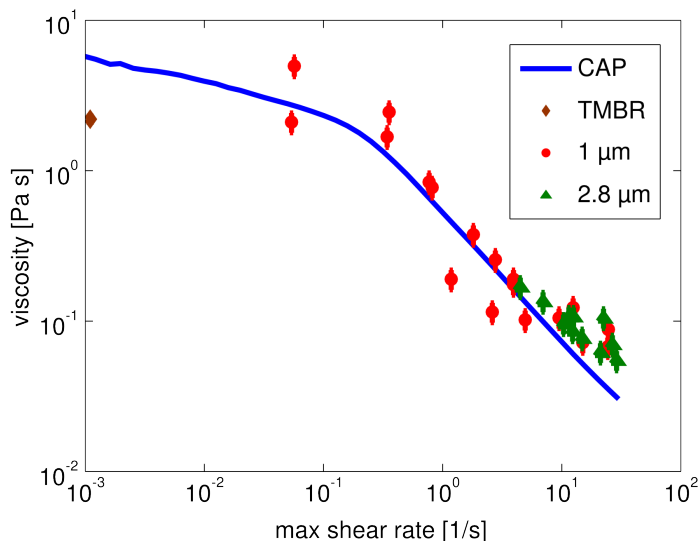


Figure 4.8: λ -DNA solutions tested for rheological response. CAP, TMBR, and DMBR methods are all used and show similar viscosities, even those that show the thinning behavior that depend on input shear rate.

techniques showing repeatability across length scales. Using Equation 2.47, we calculate the maximum shear rate the solution experiences from the moving bead. Viscosity estimates are computed by inverting the slope of the steady state compliance measurements as described in Section 2.4. TMBR estimates the expected zero-shear η from CAP while DMBR replicates steady-state shear thinning also consistent with CAP.

4.4 HA

For HA and the remaining materials, cone and plate measurements were taken using the amplitude sweep, frequency sweep, creep compliance, and steady state flow protocols while only creep data were taken via DMBR. Like the λ -DNA measurements described in the last section, the linear viscoelastic region was determined using the amplitude sweep. Frequency sweeps were acquired with attention placed on the strain amplitude to ensure that testing across frequencies remained within the linear range. Creep compliance testing ensured incomplete recovery with full relaxation upon terminating the test. In viscometric flow tests the minimum applied shear rate either resulted in the zero shear viscosity or was extrapolated using model fits. These shear thinning curves were fit with the Carreau model to produce parameters and generate force requirements as described in Section 3.6. In the interest of space, all figures resulting from this testing are not shown for all materials.

Hyaluronan (HA) is a linear glycosaminoglycan (GAG) that has disaccharides as monomers (mol. wt. 387 g/mol), making it a polyelectrolyte with a surface chemistry

similar to heavily glycosylated mucins. It is practically ubiquitous in the body and can be found in extracellular matrix (ECM), the vitreous humour of the eye, and synovial fluid (Balazs and Gibbs, 1970). Even cell types in the alveolar wall co-produce HA alongside the lung surfactant (Sahu et al., 1980) that eases inflation and optimizes gas exchange (Creuwels et al., 1997). Naturally occurring HA has molecular weights that typically range from 0.1 – 10 MD (Hardingham, 2004) and has a persistence length of approximately 8 nm (Buhler and Boue, 2004).

I used recombinant HA derived from *Streptococcus equi* (Sigma-Aldrich cat# 53747-10G) at a concentration of 10 mg/mL. As packaged, the material had a molecular weight of 1.63 MD. When measured by light scattering, the molecular weight was 1.5 MD and a radius of gyration of 115 nm.

For 10 mg/mL HA, the zero-shear viscosity using CAP was 12.1 ± 0.1 Pa s (Fig. 4.10, inset). DMBR testing used 2.8 μm diameter SPM beads to generate displacement and compliance curves (Fig. 4.9). A total of 29 curves (sequences) from 6 beads were analyzed, fit to Jeffrey model with similar systematic deviation to those found in the previous section for λ -DNA. All of these curves were of sufficient force and duration to present incomplete and non-zero recovery, indicative of a viscoelastic fluid.

Using this HA solution I have successfully demonstrated linear response in terms of compliance at the microscale with DMBR (O'Brien et al., 2008). The compliance response function is computed by normalizing the displacement with the applied magnetic force using Equation 2.86. In Figure 4.10b, the compliance functions for all input

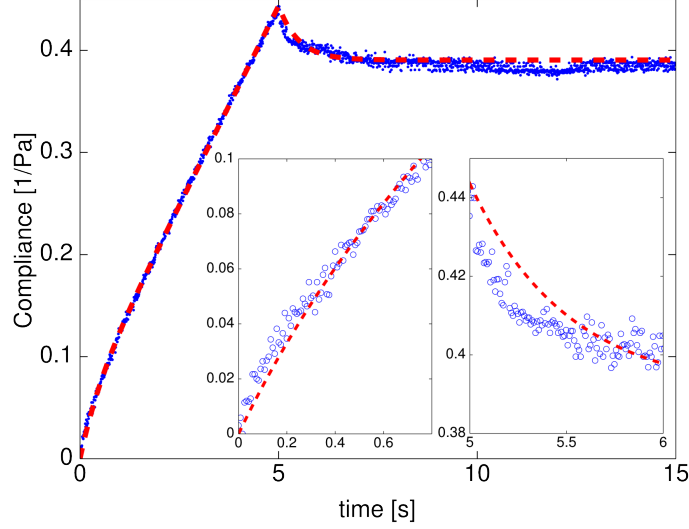


Figure 4.9: 10mg/mL HA solution tested for rheological response using DMBR. $G = 19$, zero-shear viscosity equal to 12.8 Pa s, with an R^2 value of 0.9992. Systematic deviations from model are shown as insets for both forced and relaxation periods.

forces are coincident, implying a linear response. Where the bead displacement in time (shown in Fig. 4.10a) depends on the input force, the compliance curves collapse to a single line which only occurs in the linear regime of the material where vanishingly small input forces result in correspondingly small strains. The high density of monomers in the solution corresponds to a small correlation length, producing a much better collapse in compliance space and showing a well-behaved linear response. The computed steady state viscosity for the HA solution is 12.5 ± 0.2 Pa s using this technique, very close to CAP zero-shear with only 3% difference in their average values.

The relaxation times seen in the λ -DNA experiments in Section 4.3 had different values when comparing the forced versus the relaxed parameters. This difference in parameters may be due to a heterogeneous environment at bead-sized length scales

combined with the decay of the bead motion from a deterministic process to a stochastic one (diminishing signal to constant noise). For HA, the relaxation times for both “off” and “on” periods of the force are equal within standard error, with 0.67 ± 0.04 s for the forced period and 0.78 ± 0.07 s for the relaxation period, denoting similar G values for both periods. The larger error during the relaxation period is probably due to the decay of stored stress as a deterministic process to steady state bead diffusion, a stochastic process. As the stress decays to zero, the signal to noise ratio likewise decays to a value of one. The stochastic nature of bead diffusion does not factor in the mechanical model analogues; it is treated as noise. Both CAP and DMBR data are plotted in Figure 4.11.

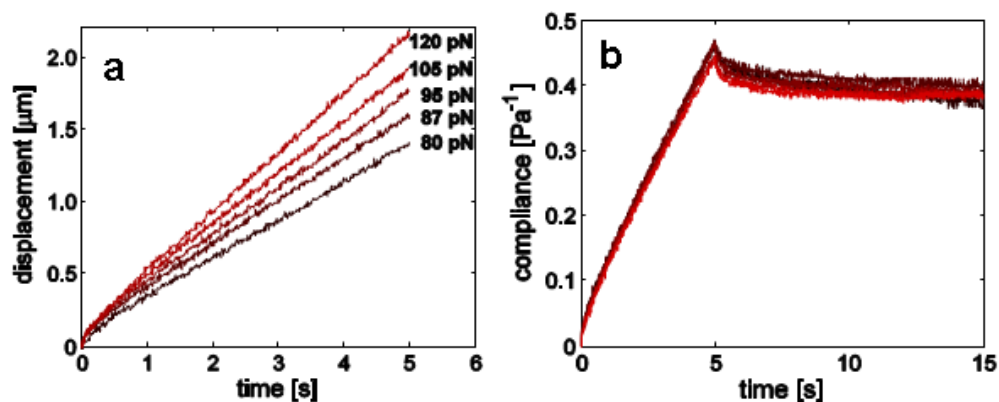


Figure 4.10: DMBR measurements of hyaluronan (HA) using 3DFM tools described in Chapter 3. Panel (a) shows displacement of $2.8 \mu\text{m}$ beads as they are pulled through 10 mg/mL HA solution with forces that range from $80\text{--}120$ pN. Displacement curvature at early time scales indicates elastic behavior, while steady state velocity is related to the zero-shear viscosity, η_0 . Panel (b) shows the reproducibility of the DMBR technique by plotting displacement normalized by the step force, which results in creep compliance. Since this HA solution is a linear viscoelastic material at the probed shear rates, disparate displacement curves in (a) collapse into a single curve when plotted as compliance in (b). Inverting the slope of the steady state compliance is equal to η_0 for HA.

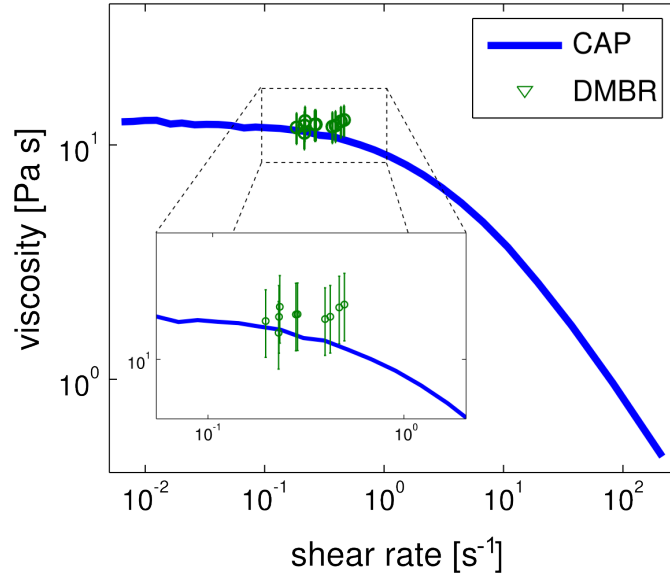


Figure 4.11: The inset plots a collection of these viscosities with HA’s cone and plate (CAP) flow profile, showing that not only is the DMBR technique internally reproducible but is consistent with CAP under specific polymer system conditions.

4.5 Guar

Of the four biopolymer systems tested here guar is the only non-electrolyte. It is a naturally occurring polysaccharide extracted from milled and filtered guar bean (Imeson, 1999). Primarily a linear polymer, guar contains a variable number of galactose (monosaccharide) side chains, has an average monomeric molecular weight of 485 g/mol, and can be found with large molecular weights of 2 MD or higher. The lack of the number of galactose side chains reduces the molecule’s solubility and increases its stiffness (Petkowicz et al., 1998; Gittings et al., 2000). Guar gum has been used with some limited success as a mucus simulant, making it of some interest to these experiments as a test material for refining methodology and quantifying MCC (King

and Macklem, 1977). With a published persistence length of 10 nm (Picout et al., 2001; Morris et al., 2008) the guar gum chains more closely match the physical stiffness of HA but has a molecular weight closer to that of a mucin.

Our light scattering measurements put the molecular weight of the guar gum sample at approximately 54 MD and the R_g at 425 nm. Assuming the guar molecules are ideal chains with this molecular weight would indicate polymer strands with a 54 μm contour length. Rheology measurements of guar show a dependence on shear rate using both CAP and DMBR techniques (Figure 4.12). More of its viscoelastic properties will be discussed in Chapter 6.

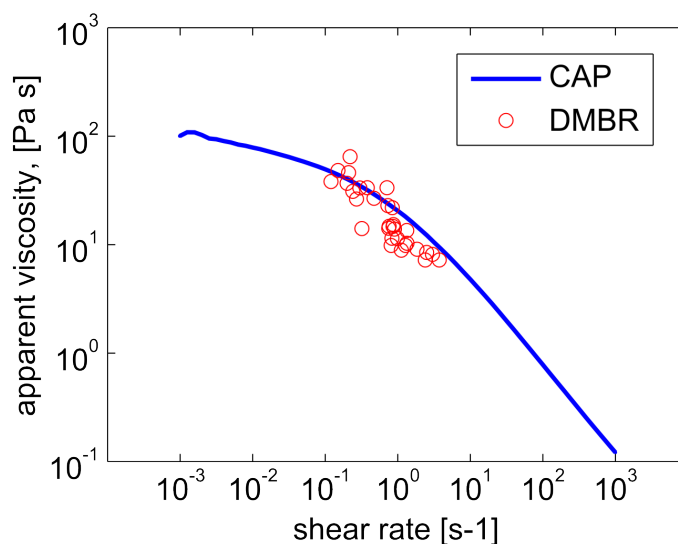


Figure 4.12: Consistency between CAP and DMBR measurements in 1.5% guar solution. Larger spread in data indicates larger heterogeneity than seen in DNA or HA. Error in CAP measurement is less than 5% and in DMBR less than 15%.

4.6 PGM

According to the literature, endogenous porcine gastric mucus (PGM) experiences a transition from liquid-like sol-phase to a more solid-like gel-phase when the pH of the system is reduced from neutral (pH=7) to acidic (pH=2) conditions and the ionic strength is less than the equivalent conductivity of 200 mM NaCl. The PGM used in the Celli study was harvested directly from porcine stomach, purified by chromatographic separation and cesium chloride density centrifugation, and lyophilized. Lastly, these specimens were reconstituted with a phosphate/succinate buffer system tuned to the desired pH (Celli et al., 2007).

An industrial source exists for PGM (Sigma-Aldrich cat#M1778-10g) but its use is largely discouraged by the community. The use of Sigma-PGM (Σ -PGM) is rejected because of Sigma's protease treatment that renders the material into an undesirable state when it destroys mucin integrity; the degraded glycoproteins result in qualitatively different rheological profiles than actual mucus as shown by previous measurements done by Kocevar-Nared in 1997 (Kocevar-Nared et al., 1997). Our light scattering measurements indicate that the majority of molecules in the Σ -PGM are large, averaging at 56 MD in molecular weight, and 310 nm in R_g , and may be related to aggregates of MUC5AC.

I used this polymer system assuming the molecules were qualitatively like mucins, such as being mostly linear in shape and heavily glycosylated. At concentrations greater than 4% this PGM had a physical consistency that by eye, looked qualitatively much

like mucus, and became entangled as expected of any other polymer system. These entanglements are mimics of transient crosslinks albeit with possibly higher zero-shear viscosities. I did attempt to gel Σ -PGM by controlling the conductivity and then acidifying its pH to about 2, but this was unsuccessful, probably because the protease treatment damaged the more vulnerable, non-glycosylated regions of the protein. Gelation is thought to occur due to conformational changes in the protein structure when exposed to low pH (Celli et al., 2007). Shown in Figure 4.13 is the shear rate depen-

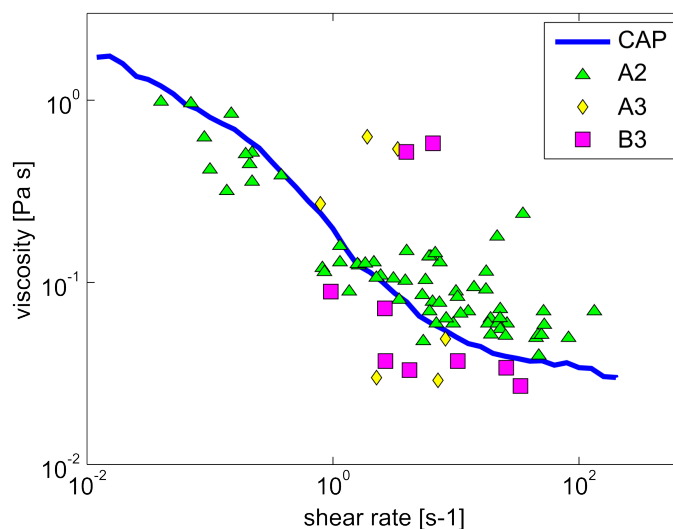


Figure 4.13: Shown as the solid line is the shear thinning response curve for 4% PGM. Overlaid as points are the steady state viscosity values as measured by DMBR in our high-throughput system (Spero et al., 2008). The results shown here originate from three different specimens tested by three different calibrated pole tips. All wells report viscosities similar to one another, implying the spread in the data is due to sample heterogeneity.

dence of PGM viscosity on input shear rate. It is a shear thinning fluid, as expected, with DMBR measurements on $4.5 \mu\text{m}$ beads retrieving on average the correct steady-state viscosity similar to CAP, but with much higher noise between measurements. To

distinguish the noise source I tested three different specimens drawn from one vial of reconstituted PGM with three different calibrated pole tips using our high-throughput DMBR system (Spero et al., 2008). Results are taken from three different wells marked as A2, B3, and A3. Each well contains steady viscosity values from all aggregate values seen in the figure across two orders of magnitude in viscosity. This result with DMBR reveals the degree of heterogeneity in the viscosity of PGM, a property of this solution to which CAP is insensitive.

This section focused primarily on PGM as a mucus simulant and a more comprehensive discussion of mucus as a biologically active biopolymer system

4.7 Mucus

Broadly defined, mucus refers to a family of soft, viscoelastic materials secreted at the cellular and tissue scales by a wide variety of organisms, vertebrates and invertebrates alike. Its persistence through the evolutionary record speaks to its success in coating, protecting, and/or lubricating cells and cell surfaces often found at interfaces with epithelial cells (Desseyn et al., 2000). While one mucus may have drastically different material properties from another, they all share a set of fundamental components: water, electrolytes, and a distribution of macromolecules called mucins (Kesimer et al., 2009). Indeed, mucus function relies heavily on its mucin profile. For example, gastric mucins experience a sol-gel phase transition in the low-pH environment of the stomach to limit diffusion and protect the lining from denaturation (Celli et al., 2007). Every

mucus is intrinsically a polymer system, specially tuned to perform its role within its target environment.

Mucins are typically giant glycoproteins, heavily glycosylated (more than 50% by wt) mostly by O-glycans along the mucin protein core. O-glycosylation is a post-translational modification believed to occur in the Golgi complex whereby glycan chains are constructed one carbohydrate at a time, binding to serine, threonine, hydroxyproline, or hydroxylysine residues. Prevalent negative charge surrounds each polysaccharide, creating a repelling force between O-glycans and thus maximizing the distance among them, as well as increasing the mucin’s hydrophilicity. The mucin swells in the good solvent which increases its pervaded volume, offering the largest possible spatial coverage for protection or lubrication. The end result is a very long and mostly unfolded macromolecule with monomer units that are best modeled as cylinders, each with its own polymer brush (Perez-Vilar and Hill, 1999) where the sum might be mentally visualized as a “fuzzy” and floppy pipe cleaner.

Membrane Bound	MUC1, MUC3A, MUC3B, MUC4, MUC12, MUC13, MUC16
Secretory	MUC2, MUC5AC, MUC5B, MUC6
Unclassified	MUC7, MUC8

Table 4.4: Human Mucin Family

In the airways, mucus serves as the first line of defense against the inhalation of pollutants or pathogens during breathing activity. It lines the upper part of the airways, creating a physical barrier between the epithelium and air interface and providing a

favorable environment where pollutants are readily entrained. Once attached to a healthy mucus network, they are removed from the lung altogether through the tireless beating of millions of cilia lining the airway epithelium in a process called mucociliary clearance. A successful mucus network is defined here as one that a wild-type ciliary system successfully transports. Ultimately, it is this flow profile, i.e. the rheology, of the mucus that dictates successful MCC.

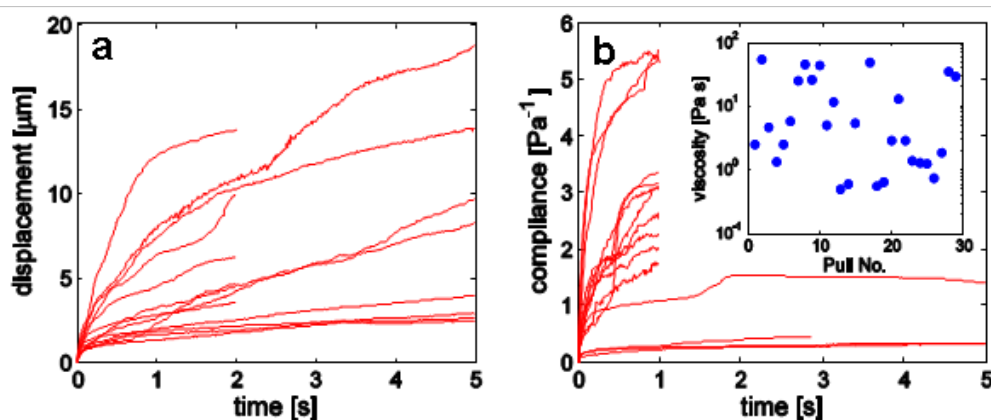


Figure 4.14: DMBR measurements of a small volume sample of human sputum using 3DFM. Panel (a) plots the displacements while Panel (b) plots compliance for successive pulls on three different $1 \mu\text{m}$ beads embedded in human sputum. Displacement curves vary widely and show no tendency to collapse when normalized to creep compliance, implying that sputum could either be non-linear at the shear rates seen immediately surround the bead surface, or that it is highly heterogeneous. Inconsistency in the curve shapes indicate that this is due to spatial heterogeneity in the sputum at length scales on the order of the bead's diameter. The inset shows that the range of computed viscosity felt by the beads in this sputum ranges widely across two orders of magnitude, from $\sim 1 \text{ Pa s}$ up to $\sim 100 \text{ Pa s}$. While not enough volume was present to run CAP on this material, such testing on similar specimen show a non-linear viscoelastic response that is consistent when retested within a short ($< 1 \text{ h}$) time scale.

To understand the origin of physical properties for a cilia-clearing mucus network in the airway, one must first identify its constituent components; i.e. its mucin pro-

file. Identified as contributing the most to the physical properties of human airway mucus *in vitro* are two mucins, MUC5B and MUC5AC. Referred to as the gel-forming mucins, MUC5B and MUC5AC, like other mucins, are heavily glycosylated and are large even for macromolecules, having molecular weights on the order of 1 to 100 MDa. Their primary sequences include cysteine-rich domains responsible for disulfide bonds often found in protein-protein interactions. These domains provide the biochemistry necessary for covalent mucin-mucin associations end to end.

Just as the gastric mucus is tuned for the vagaries of its environment through its mucin profile, so too must the mucus in the airway. That balance can be upset in a number of ways, possibly resulting in pathology. It is generally agreed in the literature that the presence of persistent bacterial lung infections is the most common pathology experienced by Cystic Fibrosis patients. Because of the absent or ill-formed CFTR protein (Cystic Fibrosis Transmembrane conductance Regulator), Na^+ and Cl^- ions are not transported in sufficient quantities to maintain an osmotic balance that would otherwise keep the surface epithelial mucus layer adequately hydrated.

The inadequate hydration of mucus in CF results in a thickened mucus that overwhelms the mucociliary system and impedes mucus clearance. This may be considered as an increase in the concentration of mucins in the mucus. A change in polymer concentration changes the length scale regime that drives diffusion rates, interactions, and dynamics. Increasing the concentration of even non-associating polymers can shift the system to a different regime, e.g. from non-entangled to entangled. It is the concentration of interaction points, whether by entanglements or transient cross-links, that is

responsible for the elastic properties or modulus of the polymer solution (Rubinstein and Colby, 2003). In addition, experiments have shown that low mucin concentrations also reduce the effectiveness of mucus clearance (Shih et al., 1977; Chen and Dulfano, 1978; Puchelle et al., 1980b).

The physical properties of mucus can be drastically altered through the existence of dynamic and adjustable associations between mucins. Up to the entanglement regime, the overall concentration of polymers is responsible for the system's viscosity. It is the concentration of interactions or cross-links that dictates the system's elasticity. Adjustable associations between mucin strands and adjustable water concentration through electrolyte balance work together to modulate the system's rheology.

Physiological relevance becomes an issue when considering macro-scale measurements because the rheological response of polymeric systems is time and length scale dependent. The main task of MCC is to transport micron-sized and smaller particles from the lung. The CAP rheometer can measure the rheological response of mucus for large length scales that correspond to organ sized clearance. While cone and plate techniques successfully even out the smaller heterogeneities found in a mucus network, they do not accurately describe the material environment sampled by a bacterium, a piece of particulate matter, or even a cilia tip responsible for the propulsion of mucus in MCC.

While it is possible for their mucin compositions to be similar, there is a distinction between mucus and sputum. Mucus is the material secreted into the lung and actively transported by the mucociliary system whereas sputum is typically a pathogenic

substance eliminated from the lung by cough (Yeates et al., 1997). Mucus typically contains little to no actin, DNA, or neutrophils while sputum contains all of these in significant quantities (Rubin, 2006). These additional biopolymers would contribute to higher viscosity and shear moduli and thus would lower flow rates. A confocal image I took for HBE mucus obtained from cell culture is shown in Figure 4.15, and it does show the presence of small amounts of actin (red, phalloidin) and DNA (green, YOYO-1) but their concentrations are dwarfed by the amounts seen in (Rubin, 2006). These small amounts of actin and DNA might contribute to heterogeneity in the HBE mucus specimens, but is probably not enough to drastically alter the specimen's large scale rheology.

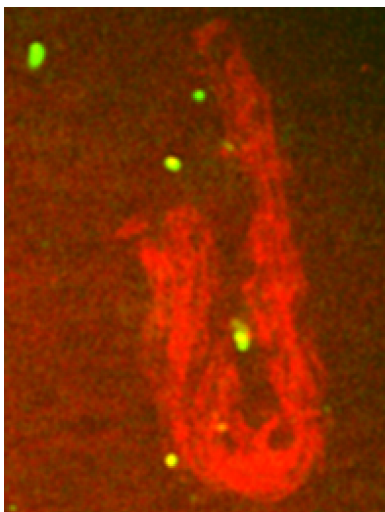


Figure 4.15: Confocal imaging of DNA and actin in a specimen of HBE mucus. DNA and actin are stained with YOYO (green) and phalloidin (red), respectively. This cluster of actin was the only one present in the 3 μL specimen used here.

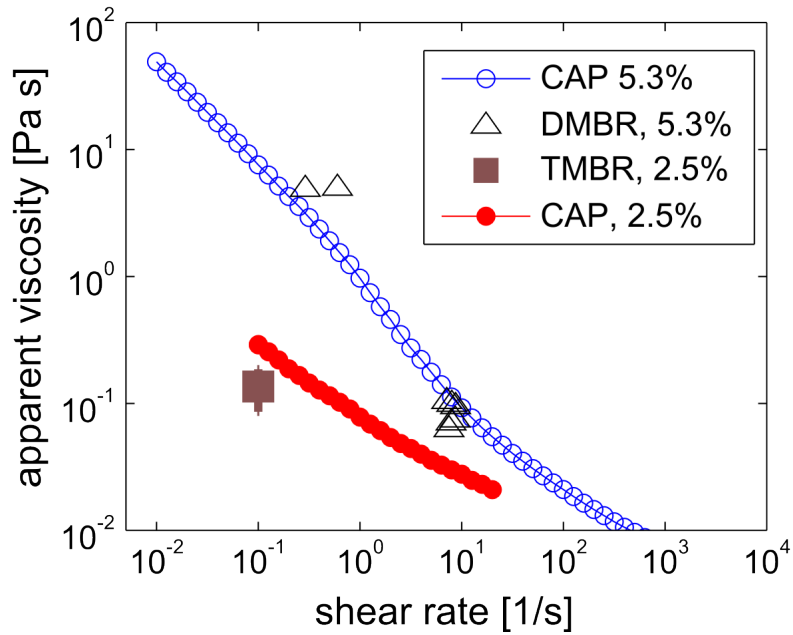


Figure 4.16: Shown as the solid line is the shear thinning response curve for two specimens of HBE mucus. I performed CAP measurements for both the 2.5% (●) and the 5.3% (○) mucus specimen. TMBR measurements (■) for 2.5% mucus are lower than the CAP data by about 50%. DMBR measurements (△) for 5.3% mucus exhibit shear thinning, with error in each measurement being <15%.

4.8 Discussion

Shown here are many cases where the steady state values for DMBR, TMBR, and CAP correspond given a few assumptions. First, the bead is sensitive to rheology of material in its immediate surroundings. The further

In Figure 4.17 I have plotted the zero-shear viscosity against the Maxwell Model approximation for G at infinite frequency. This representation is related to the data shown in Figure 3.20, where each material shown is in the context of measurable quantities using the TMBR and DMBR methodologies. In this figure, the λ -DNA solutions present a fairly linear relationship in log space, with a power law slope of _____. Saliva,

PGM, and 2.5% HBE mucus solutions are relatively close in magnitude to the DNA line, somewhere between 0.7 and 1.4 mg/mL. Guar and HA exhibit rheologies similar to 8% mucus and sputum. This collection of results, combined with its sensitivity to heterogeneity, shows how DMBR can provide useful as well as unique information about polymer solutions.

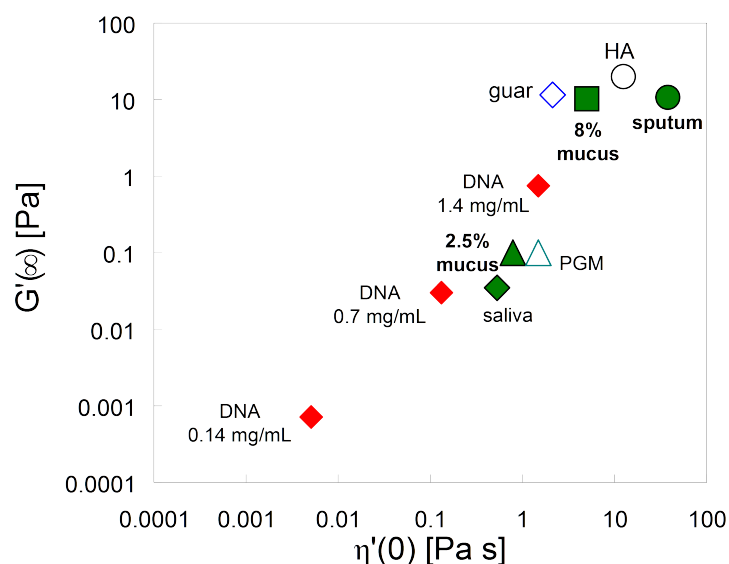


Figure 4.17: Phase plane of Viscoelasticity using the modulus and viscosity elements of the Maxwell Model. Instantaneous shear modulus (infinite frequency) and long-time approximations zero-shear viscosity for the materials studied here. The λ -DNA solutions show a predictable power law response with respect to concentration. The viscoelastic responses of saliva and normal mucus lie somewhere between the 0.7 mg/mL and 1.4 mg/mL λ -DNA.

4.9 Conclusions

Here I presented empirical data where I used several different methods of measuring the rheology of biomaterials. From these measurements we learned that λ -DNA has

viscoelastic material properties that lie in the same order of magnitude as mucus and can be used a quasi-linear viscoelastic standard material.

DMBR and CAP methods result in similar values for the viscosity and elasticity of linear viscoelastic materials. It can also replicate shear-thinning modes in the compliance response for all tested materials. One potential divergence between the methods concerns the timescales over which each method is sensitive. DMBR results differ from CAP results in the time it takes for either method to relax the inputted stress.

Chapter 5

Shape Effects

5.1 Overview

Increasingly, the research community applies magnetophoresis to micro and nanoscale particles for drug delivery applications and the nanoscale rheological characterization of complex biological materials. Of particular interest is the design and transport of these magnetic particles through entangled polymeric fluids commonly found in biological systems. We report the magnetophoretic transport of spherical and rod-shaped particles through viscoelastic, entangled solutions using lambda-phage DNA (λ -DNA) as a model system. To understand and predict the observed phenomena, we fully characterize three fundamental components: the magnetic field and field gradient, the shape and magnetic properties of the probe particles, and the macroscopic rheology of the solution. Particle velocities obtained in Newtonian solutions correspond to macroscale rheology, with forces calculated via Stokes Law. In λ -DNA solutions, nanorod velocities are 100 times larger than predicted by measured zero-shear viscosity. These results are the first published observations of shear thinning in a polymer network induced

by sub-micron sized driven particles. Particles experiencing transport through a shear thinning fluid indicate that magnetically-driven transport in shear thinning fluids may be especially effective and favor narrow diameter, high aspect ratio particles. A complete framework for designing single-particle magnetics-based delivery systems results when we combine a quantified magnetic system with qualified particles embedded in a characterized viscoelastic medium.

5.2 Background

Micron and nanoscale magnetic particles attract much attention in research as active probes of the microrheological properties for biological polymer systems and as potential drug carriers in clinical settings. Because of this, magnetophoresis is becoming more common in diagnostic and analytical devices (Jain, 2003), general research techniques (Amblard et al., 1996b; Gijs, 2004; Lehmann et al., 2006), and clinical applications (Safarik and Safarikova, 2002). This latter area of medical science is developing rapidly, employing magnetophoretic systems for drug delivery (Berry and Curtis, 2003; Okada and Toguchi, 1995; Tartaj et al., 2003), gene transfection (Dobson, 2006), and hyperthermic therapies (Goya et al., 2008; Wust et al., 2002) where particle delivery to a targeted site is critical. Materials encountered in these biomedical applications such as tissue, extracellular matrix (ECM), cytoplasm, and synovial fluid contain complex microstructures that present multiple challenges to particle transport. Confined paths in dense meshes necessitate the use of nanoscale particles, while the flexibility

of the mesh in viscoelastic solids or liquids results in complex rheological behavior and requires the consideration of high shear rate effects. For example, where some biomaterials such as the ECM can be considered viscoelastic solids (gel), synovial fluid is an entangled polymer system that exhibits yield phenomena and shear thinning (Krause et al., 2001). Furthermore, the question of particle shape arises as one balances considerations of drug loading, force generation, and transport (drag) effects. Solving these challenges will open new opportunities for the transport of particles and for applications of magnetophoresis in medical science.

The use of magnetophoresis to manipulate particles predictably in these challenging biological environments demands a quantitative understanding of the forces required to produce transport. Despite the increased use of magnetophoresis over a broad range of fields, limited studies have investigated quantitative microparticle magnetophoresis within the context of a well-characterized system (Amblard et al., 1996b). To date there are no reports in microstructured biological media relevant to practical biomedical applications that establish full characterizations of applied forces, particle and media properties, alongside single particle measurements. Kuhn, et. al. showed effective transport for a solution of magnetic particles with observations at the macroscale where the transport of bulk fluid was measured (Kuhn et al., 2006b). In a later paper Kuhn, et. al. focused on the effects of the particle chemistry and showed increased rates of transport for nanoparticles functionalized with a proteolytic collagenase (Kuhn et al., 2006a). The goal of the current study is to develop a predictive understanding of particle magnetotransport that may be used for the design of drug delivery carriers

in medical applications. To that end, we require well characterized biofluid media, particles and magnetic fields as well as single particle transport measurements.

The concentrated solutions of lambda-phage DNA (λ -DNA) used here function as useful models of entangled networks typically found in biological media and exhibit complex rheological phenomena. DNA has several advantages over other biopolymer systems that might otherwise be suitable models. It contains a highly monodispersed distribution of polymer lengths which is atypical in synthetic polymer systems, allowing for predictable and reproducible rheological properties from one DNA sample to the next. DNA has a persistence length that is intermediate between synovial fluid and the filaments of ECM (collagen) and cytoplasm (actin, microtubules). In addition, it serves as a model for infected mucus which may contain a high percentage of entangled DNA (Rubin, 2006). For our purposes, the measured macroscale rheological properties of the λ -DNA solutions are sufficient to explain our transport data. Using these rheological properties, we can predict the forces required to move a sphere or rod through a shear thinning material like λ -DNA. For probe particles, we used commercial 1 μm diameter spheres and fabricated nanorods with nominal diameters of 200 nm. We characterized the latter with regard to shape and size using scanning electron microscopy, and measured their magnetic properties using SQUID magnetometry. Finally, we implemented a simple magnetics system distinguished here from the 3DFM system (see Chapter 3) with a characterized field and field gradient whose magnitudes are suitable for deployment in medical applications.

For quantitative magnetophoresis and the understanding of particle shape effects,

we first show that calculated and measured transport velocities agree in the transport of the microbeads and the nanorods moving in a Newtonian viscosity standard. Following calibration of the magnetophoretic system, we investigated particle transport in λ -DNA solutions at two concentrations within the entanglement regime. Particles traveled at velocities over 100 times faster than expected based on Stokes Law and the low shear rate viscosity of the λ -DNA solutions. We inferred the viscosities from the calculated forces and measured velocities, and determined that the viscosities seen by the particles decreased with increasing particle velocity. This phenomena is consistent with our measurements of shear thinning in λ -DNA solutions using CAP, and results when an applied shear stress aligns the polymer strands in a semi-dilute or entangled network (Hyun et al., 2002) or disrupts the size and arrangement of aggregate polymer strands in solution (Quemada, 1998). While shear thinning has been measured for λ -DNA using bulk rheological techniques (Heo and Larson, 2005), this is the first report of shear thinning of a polymer network induced by sub-micron sized driven particles. These results have profound implications regarding transport in biomaterials where short delivery times is a common requirement. Such applications often have practical constraints where the magnitude of driving forces is limited. Demonstrating that particles can induce shear thinning at the sub-micron scale reduces the force requirements for a magnetophoresis system or might provide faster transport over greater distances than one might otherwise anticipate.

5.3 Methodology

This chapter describes the motion of magnetic particles under an applied magnetic field. The force balance $F_m = F_d$ describes particle dynamics in low Reynolds number situations where F_m is the applied magnetic force and F_d is the drag force due to the fluid. The former depends on particle magnetic properties and the magnitude and gradient of the magnetic field. The latter depends on the medium properties and the particle geometry. First, I describe particle magnetic properties, followed by a characterization of medium properties and particle geometry. The characterization of these quantities follows thereafter.

5.3.1 Nanoparticles

The particles used here were non-magnetic 1 μm polystyrene control beads (Polysciences, Warrington PA), superparamagnetic 1 μm carboxy-functionalized MyOne[®] microspheres (Invitrogen, Carlsbad CA) and nickel rods fabricated in house. Highly monodispersed, the MyOne bead radius was 525 nm, as reported by the manufacturer and confirmed by our in-house SEM measurements. We used electrochemical deposition to fabricate nickel rods inside 200 nm pores in a commercially available anodized alumina oxide (AAO) template (Whatman, Maidstone UK). The nickel rods varied in length from 5–20 μm . This range in rod length provided us with a range of aspect ratios, none of which were below 15. These large aspect ratios allowed us to approximate a nanorod as a prolate ellipsoid in order to estimate the magnetomotive force induced

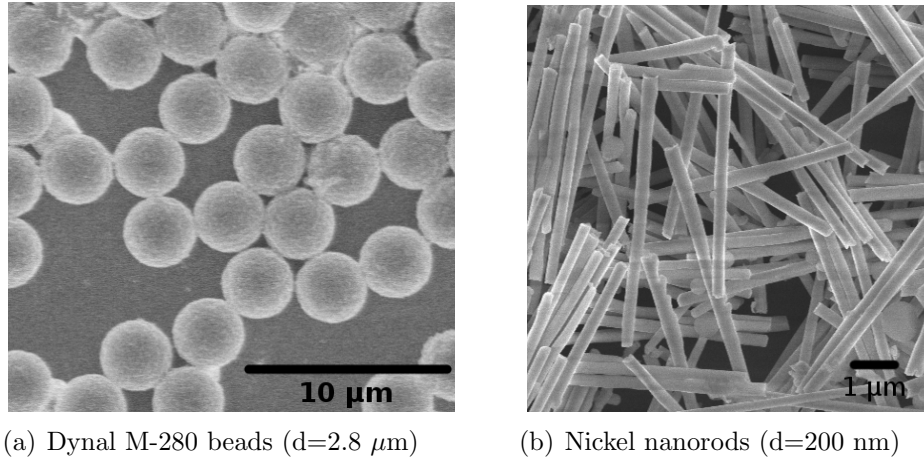


Figure 5.1: Shown are SEM images for $2.8 \mu\text{m}$ in 5.1(a) and nickel nanorods in 5.1(b). Both particles are used in the driven microrheology experiments performed in this dissertation.

by the source magnet and the shear rate along the surface of the rod. We adapted the electrochemical plating bath and deposition parameters from a method devised by Nielsch and co-workers (Nielsch et al., 2000). After dissolving the membrane, ultrasonication suspended the freed rods into a 0.01% SDS solution that we later exposed to a magnetic field in excess of 0.4 T.

5.3.2 Magnetic Characterization of Nanoparticles

A Superconducting Quantum Interference Device (SQUID) magnetometer (Quantum Design, Inc. MPMS-5S) measured the magnetic characteristics of the beads and rods at room temperature. Because their long axis was always parallel to the applied magnetic field during experiments, we characterized the nickel rods as a vertically aligned array while still embedded inside their host template. We measured the physical

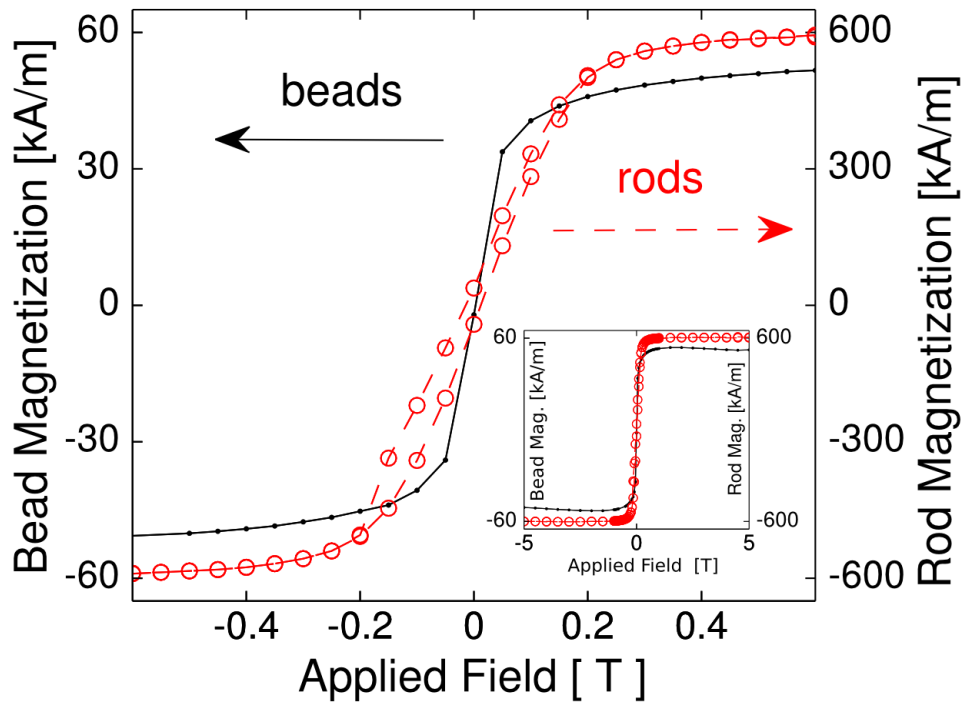


Figure 5.2: Magnetic susceptibility characterization of nanoparticles used in DMBR experiments. Measured magnetization per MyOne bead or nickel nanorod long axis as a function of the applied magnetic field (± 5 T), measured at 290K by SQUID magnetometry. We tested the beads as a dried suspension and the rods as a membrane-bound array. The bead polymer matrix and the sample holder induce a slight diamagnetic background that we removed by normalization. We also normalized the sample magnetization with respect to the number of particles. Beads show an absence of area inside the hysteresis loop, indicating these particles exhibit only paramagnetic behavior whereas rods do show a small amount of remanent magnetization, indicating slight ferromagnetic behavior. We define particle saturation at fields where particle magnetization reaches 95% of its maximum.

dimensions of the particles using electron and optical microscopy.

5.3.3 Newtonian fluid and Viscoelastic λ -DNA solution

Needing a viscous, Newtonian standard to calibrate the magnetophoretic system, we used Light Karo Syrup (ACH Food Companies, Inc.), a commercial product derived from corn. For our viscoelastic polymer system, we prepared entangled solutions of λ -DNA (Invitrogen, Carlsbad CA), first being careful to anneal one of the single-stranded, hanging ends with a complementary 12 base pair oligonucleotide (UNC oligonucleotide synthesis facility, Chapel Hill NC). This prevented the formation of cyclic DNA, and minimized potential solution heterogeneity (Braun et al., 1998). We prepared all λ -DNA solutions from a stock solution of 2.4 mg/mL. Test conditions for nanoparticle experiments included two λ -DNA solutions within the entanglement regime at 0.7 and 2.0 mg/mL. Due to the large quantity of solution needed for cone and plate (CAP) rheometry, we restricted the macroscale viscometry measurements to a solution at 1.4 mg/mL and 0.7 mg/mL. The agreement between our data and literature values and the consistency of the concentration dependent rheology of λ -DNA solutions supported this limited application of CAP. We checked for non-specific adsorption of λ -DNA to the particles, which might confound driven transport, by imaging suspensions of particles dispersed in λ -DNA, fluorescently labeled with YOYO-1 (data not shown). We observed no significant increase in fluorescence near these particles, indicating little λ -DNA adsorption. Non-specific absorption of λ -DNA to the particles was minimal when suspended in a solution labeled with fluorophore. More information and additional

parameters for the DNA polymer solutions used here are given in more detail in Table 4.1 and Table 4.2.

DNA Conc [mg/mL]	0.7	1.4	2.0
η_0 [cP]	1300	3900	17000
η_∞ [cP]	5	8	11
λ [s]	5.7	7.1	16
n	0.15	0.038	0.034
a	1.3	1.0	0.8
testing regime	DMBR	CAP	DMBR

Table 5.1: Carreau Parameters for λ -DNA solutions

5.3.4 Viscometry of transport media

A controlled-stress cone and plate rheometer (TA Instruments, model AR-G2) measured the viscometry of the Newtonian and λ -DNA solutions at 23 °C with a 40 mm, 1° cone across feedback-controlled input shear rates ranging from 1 to 1000 s⁻¹. We fit the viscometry data for the λ -DNA solutions to a Carreau-Yasuda model,

$$\frac{\eta - \eta_\infty}{\eta_0 - \eta_\infty} = [1 + (\lambda\dot{\gamma})^a]^{(n-1)/a} \quad (5.1)$$

where η_0 and η_∞ are the medium viscosities at zero and infinite shear, respectively, λ the thinning time constant, m modulates the width of the thinning regime, and n is the flow-behavior index that leads to the power-law slope equal to $(n - 1)$ (Heo and Larson, 2005). Following the method used by Heo, et al., we tried first to fit our data to a Cross model, which is one-parameter simpler than the Carreau-Yasuda model for

shear thinning. We found that where the Carreau-Yasuda model provided sufficient parameters to fit the observed behavior, the Cross model did not. Also, because we were comparing our data with Heo et al., we chose the Carreau-Yasuda model for consistency.

5.3.5 Microparticle Magnetophoresis Apparatus

For these experiments we chose to use a magnetophoresis apparatus that was separate from the 3DFM magnetics subsystem described in detail in Section 3.4. A goal of this study was to close the loop on magnetophoretic measurements by characterizing the source magnet field and field gradient both empirically and from theoretical model, allowing us to compare expected force values from both approaches.

The microparticle magnetophoresis apparatus used here consisted of a one inch long cylindrical rare earth (NdFeB) permanent magnet (K&J Magnetics, Inc.) mounted on a translation stage and an inverted optical microscope. The sample, enclosed in a transparent microfluidic chamber, contained nanoparticles dispersed in a small volume of test fluid (Fig. 5.3, inset). Adjustments made to the axial position of the magnet with respect to the sample exposed the particles to variable forces during magnetophoresis experiments. We used a digital Gauss/Teslameter Model 5080 (W. Bell, Orlando, FL) to measure the magnitude of the magnetic field applied to the particles as a function of distance from the axial face of the magnet. We determined particle positions by taking time-lapse images of the driven particles using a microscope. The image-acquisition system consisted of a Pulnix camera, model PTM-6710CL (JAI, Inc., San Jose CA),

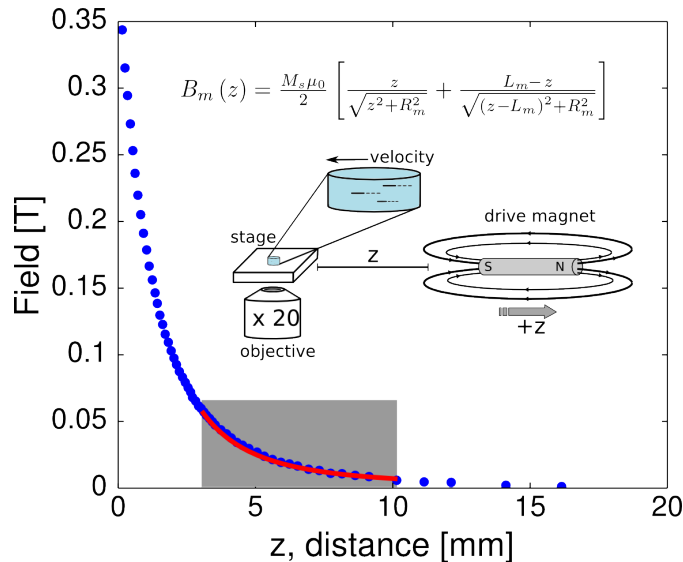


Figure 5.3: Measured magnetic field as a function of distance from the face of the cylindrical permanent source magnet with mathematical fit (red, solid). The shaded box represents the field measurements over the experimentally relevant distance range. Inset: Apparatus. At left is the axially adjustable cylindrical magnet we use to actuate the microparticles. At right is a microscope objective with a sample volume within a PDMS well (top and bottom glass coverslips are not shown). The inset shows the time-lapsed paths of magnetically translating particles as a series of dots.

an EDT-PCI DV (Engineering Design Team, Beaverton OR) frame grabber card, and a PC workstation. The CISMM Video Spot Tracker software (<http://cismm.org/downloads/>) handled particle tracking while MATLAB routines computed velocities. We mounted the entire experimental apparatus onto a floating optics table in order to minimize mechanical vibrations.

A microliter-sized volume chamber contained the sample of particles dispersed in the media. We constructed a sealed sample well from a 50 μm thick sheet of polydimethylsiloxane (PDMS) containing a 1.5 mm round hole and two glass coverslips. The diameter of the sample well was less than the width of the magnet to minimize

lateral variations of the magnetic field within the sample chamber. Before applying any magnetic field and collecting data, the sample rested for at least ten minutes to ensure the sample reached hydrodynamic equilibrium. Each particle suspension contained non-magnetic particles as well as magnetic particles, enabling a quantitative measure of remaining drift. We subtracted the velocities of the control particles to correct magnetically-driven particle velocities.

5.3.6 Modeling and Measuring Field and Field Gradient

Derived from first principles, the magnitude of the magnetic field B_m of a cylindrical source as a function of the axial distance from the face is

$$B_m(z) = \frac{\mu_0 M_0}{2} \left[\frac{L_m - z}{\sqrt{R_m^2 + (z - L_m)^2}} + \frac{z}{\sqrt{R_m^2 + z^2}} \right] \quad (5.2)$$

where M_s is the magnetic saturation of the magnet, z is the axial distance from the face of the magnet, L_m is the length of the magnet, and R_m is the magnet radius (Meehan, 2007). We measured B_m of the permanent magnet as a function of z from the face of the magnet (Fig. 5.3, inset), collecting values from the magnet face to 18 mm away. During magnetophoresis experiments, the nanoparticles were always within a range of 3 to 10 mm from the magnet face (Fig. 5.3).

Using least-squares regression, we fit the magnetic field as a function of distance in the z direction, $B_m(z)$, over the experimentally relevant z range (Eq. 5.2). We calculated the axial distance dependent field gradient of the magnet in the z direction,

∇B_z , by taking the derivative of 5.2 with respect to z (Eq. 5.3) and substituting the variable values obtained through the fit procedure.

$$\frac{dB_m(z)}{dt} = \frac{\mu_0 M_s}{2} \left[\frac{-z^2}{(R_m^2 + z^2)^{3/2}} + \frac{1}{\sqrt{R_m^2 + z^2}} + \frac{(L_m - z)^2}{(R_m^2 + (z - L_m)^2)^{3/2}} - \frac{1}{\sqrt{R_m^2 + (z - L_m)^2}} \right] \quad (5.3)$$

5.3.7 Quantitative Microparticle Magnetophoresis

To describe the magnetic driving forces, \vec{F}_m , I described the force equation for the sphere geometry in Section 2.4.1 and for the rod geometry in Section 2.4.2 for the rod geometry. These relationships were used to compute the force expected for either geometry as a function of field, field gradient, or distance from the axial face of the source magnet.

5.3.8 Stokes Drag Forces

Previously I defined the Stokes drag force for the sphere geometry in Section 2.2.7.2 and for the rod geometry in Section 2.2.8.2. These relationships enable the determination of forces when particles are actuated in a fluid of known viscosity and vice-versa when the applied forces are well understood. In Newtonian fluids the medium viscosity is constant and particle motion lacks inertial effects because of the low Reynolds number ($Re < 10^{-2}$) conditions. Actuating particles under such conditions provides a convenient and simple method for computing the force on a particle when the effects of its geometry are known.

Rod motion was always in the axial direction, because the rods align naturally along their axis length to the field lines that emanate from the drive magnet. The nickel rods had radii between 100 and 175 nm and a range of different lengths due to breakage during processing which required an individual calculation of β_c for each rod. Error analysis indicates this range of rod radii would add 10% variability to the viscosity results.

5.3.9 Validating Particle Transport Experiments

One typically applies Stokes Law in particle transport experiments to deduce the applied force on a particle, with independent coefficients for particle geometry and fluid viscosity. To use Stokes Law to measure fluid viscosity, we need to know the force applied to the particle. We obtain this in two ways and show their agreement. First, we compute $\vec{F}_m(z)$ for the particles based on equations 2.90 and 2.98. Second, we obtain the applied particle force using $\vec{F}_d = \beta\eta v$, with measured values of η of the Newtonian solution, of the geometries of the particles, and of their measured velocities. We can then use the force on the particle as a measured quantity and apply a generalized form of Stokes Law to show that our transport measurements are consistent with the shear rate dependent viscosity of the λ -DNA solutions.

5.3.10 Estimating Shear Thinning

To determine the maximum shear rate on a rod in axisymmetric flow, we approximated the shape as a prolate ellipsoid given that the equations of motion for the case of

cylindrical geometry is not analytically soluble. We modeled the geometries in COMSOL to show the convergence between the two distinct geometries and provide the analytical solutions for the equations of motion. Finally, we compared the shear rate magnitudes for the sphere, the prolate ellipsoid, the rounded cylinder (an intermediate case), and the cylinder using COMSOL models. The analytic solutions for the shear rate magnitudes are compared for the sphere and the prolate spheroid. The simulations confirm the analytical solutions derived for the sphere in Section 2.2.7.3 and for the rod in Section 2.2.8.3;

We used data from the CAP studies of the λ -DNA solution to understand the enhanced transport seen by our nanoparticles. To place our measurements within the shear thinning regime we use the Generalized Newtonian fluid (Morrison, 2001), writing the Stokes equation as $\eta = -\vec{F}_d/\beta v$ and the velocity in terms of the shear rate according to Equation 2.43. Finally, we equate the drag and magnetic forces to obtain a form of Stokes Law that explicitly contains the shear rate:

$$\eta(\dot{\gamma}) = \frac{3F_m}{2r\beta\dot{\gamma}} \quad (5.4)$$

This relationship assumes a Stokes flow field for a non-Newtonian fluid which is not correct and assumes that the bead is mostly sensitive to the material immediately surrounding it. With this equation we can plot our transport data in direct comparison with the Carreau-Yasuda model fits to viscometry data.

5.3.11 Shape Effect Attributes

5.3.11.1 Particle velocity vs. shape

The delivery speed of a carrier particle and the number of deliverable molecules are of paramount significance when one designs a magnetophoretic drug delivery system, where both characteristics depend on particle size and shape. The magnetophoretic velocity results from a combination of driving and drag forces (Eq. 5.4) applied to the particle, which themselves are related to the volume of magnetized material and the drag coefficients respectively. The ratio of the velocities can be written as a product of three ratios:

$$\frac{v_c}{v_s} = \left(\frac{\beta_s}{\beta_c}\right) \cdot \left(\frac{F_c}{F_s}\right) \cdot \left(\frac{\eta_s(\dot{\gamma}_s)}{\eta_c(\dot{\gamma}_c)}\right) \quad (5.5)$$

Attached to the surface of delivery particles and/or loaded internally, the number of deliverable payload molecules is a function of the surface area or volume of the particle.

5.3.11.2 Drag force vs. shape

We can now compare the selection between spherical and cylindrical shapes in the context of nanoparticles transport. Assuming that both particle shapes studied here have equal volume, the relationship between the radius of a sphere and the radius and axial length of a cylinder is

$$r_s = \left(\frac{3L}{4}\right)^{1/3} r_c^{2/3} \quad (5.6)$$

which shows a higher sensitivity to r_c over L . Given a constant particle velocity and Newtonian viscosity, we can now compute the ratio of the geometry coefficients as

$$\frac{\beta_c}{\beta_s} = \left(\frac{81}{16}\right)^{-1/3} p^{2/3} (\ln(p) + v_{\parallel})^{-1} \quad (5.7)$$

where the aspect ratio of the cylinder is $p = L/2r_c$. For $p > 1$, we find that $\beta_c/\beta_s > 1$ resulting in a drag penalty when one switches from a spherical to a cylindrical shape. For our cylinders p ranges from 15-105, corresponding to an increase in drag of up to 65% ($\beta_c/\beta_s \approx 1.65$) for the cylinder over that of the sphere.

5.3.11.3 Magnetic force vs. shape

Given the smaller viscous drag coefficient of a sphere versus a rod of equal volume, a researcher might conclude that a spherical particle would outperform a cylindrical particle of the same volume with regard to particle velocity. However, one must also consider the effect that shape has on the driving force, which does not depend solely on magnetic content. When comparing the forces on a sphere (Eq. 2.91) and cylinder (Eq. 2.98) made of the same material and equal volume, the force ratio is

$$\frac{F_c}{F_s} = \frac{8(\mu_r + 2)}{3} \quad (5.8)$$

which must be greater than 1 when using any magnetic material, implying that for these conditions, $F_c > F_s$. For our nickel nanorods, where $\mu_r = 18.3$, this results in an applied force that is about 50 times higher for a cylinder than for a sphere of the same

volume ($F_s/F_c \approx 50$).

5.3.11.4 Viscosity vs. shear rate

Because the spheres and cylinders experience different shear rates, we must recognize the concomitant change in the shear rate dependent viscosity and compare the viscosity ratio, $\eta_c(\dot{\gamma}_c)/\eta_s(\dot{\gamma}_s)$, via the Carreau-Yasuda model. Because $\eta_0 \gg \eta_\infty$, we can approximate η_∞ as zero, and because we focus on just the high shear rates in the thinning regime, we can further simplify the ratio to

$$\frac{\eta_c(\dot{\gamma}_c)}{\eta_s(\dot{\gamma}_s)} \approx \left(\frac{\dot{\gamma}_c}{\dot{\gamma}_s}\right)^{n-1} \quad (5.9)$$

which incorporates an error of 5% for our experiments. When we combine the effects of magnetic and drag forces (Table 5.2), we can compute the composite ratio of particle velocities within 10% error with

$$\frac{v_c}{v_s} = \frac{3p^{2/3}(\mu_r + 2)}{2(\ln p + v_{\parallel})} \left(\frac{\dot{\gamma}_c}{\dot{\gamma}_s}\right)^{n-1} \quad (5.10)$$

The velocity ratios for the types of particles used in our experiments for the same shear rate show a clear bias for the rod geometry, with approximately 30 times the effective transport rate. The primary contributor to the effectiveness of rod transport is the force ratio, with the drag and viscosity ratios mostly canceling each other out.

5.3.11.5 Shear rate vs. shape

We will find that because a rod has a smaller diameter than a sphere of equal volume, it has the potential to experience greater shear thinning due to a higher driven velocity and therefore shear rate. The $\dot{\gamma}_c/\dot{\gamma}_s$ ratio shows dependence upon the aspect ratio as well as the flow behavior index, n .

$$\dot{\gamma}_c/\dot{\gamma}_s = (3p/2)^{1/3} \quad (5.11)$$

We used the range of aspect ratios found in our experiments to compute ratios that range from 7 to 11. These $\dot{\gamma}_c/\dot{\gamma}_s$ ratios indicate a 7 to 11-fold increase in the shear rate for the cylinder over the sphere. It is important to note that the cylinder's high shear rate advantage vanishes for a Newtonian fluid as its viscosity lacks shear rate dependence. In a shear thinning fluid, however, this increase in the shear rate results in a greater velocity for the rod compared to the sphere. Access to these higher shear rates allows a rod-shaped particle to propagate almost 10 times more effectively through a lower viscosity medium. We note that a rod-shaped particle might have additional advantages over a bead in its ability to penetrate the interstitial spaces and entanglements between polymer molecules in biomaterials, though we do not explore these advantages here.

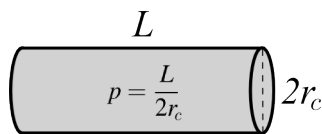


Figure 5.4: The aspect ratio, p , is the ratio between the axial length and the diameter of a rod.

5.4 Results

5.4.1 Solution Viscometry

The Newtonian solution used in this investigation had a zero-shear viscosity of 3.38 ± 0.04 Pa s and was constant at shear rates below 100 s^{-1} (Fig. 5.5). The particles driven in this solution had $\dot{\gamma}$ values less than 100 s^{-1} . In contrast, CAP rheometry of a 1.4 mg/mL λ -DNA solution revealed significant shear thinning at shear rates greater than 0.14 s^{-1} , which corresponds to a λ of 7 s. The thinning regime extended to the highest shear rates tested, i.e. 20 s^{-1} . The power-law slope for the thinning regime was -0.96 , leaving $n = 0.04$. Both of these values for the Carreau-Yasuda model parameters agree well when compared to data published in Heo and Larson (Heo and Larson, 2005). Our data from CAP rheometry of 0.7 mg/mL λ -DNA solution showed less than 8% average variability when compared to the data published in Heo and Larson (Heo and Larson, 2005). In light of the agreement of our CAP study with published values and because of the expense of λ -DNA at the required concentrations and volumes, we fit power-law slopes to the tested concentrations in Heo and Larson (Heo and Larson, 2005) and extrapolated to a slope for our microscale tested concentration at 2 mg/mL.

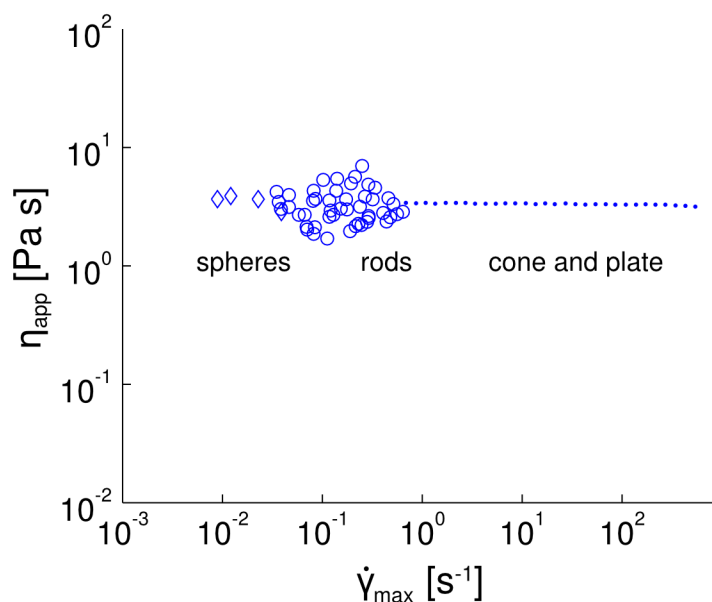


Figure 5.5: The viscosity (η_{app}) of the Newtonian standard solution as a function of the applied shear rate ($\dot{\gamma}$) measured by CAP rheometry (\bullet) and driven particle velocitometry (MyOne beads \diamond , nickel rods \circ). The viscosity is constant as a function of the applied shear rate indicative of Newtonian behavior. The CAP rheometer and microparticle probes both measure the same average viscosity.

5.4.2 Nanoparticle Magnetic Properties

Under experimental conditions, the maximum magnetic field experienced by the particles in our magnetophoresis system was less than 0.06 T, as determined by measurements with a Hall probe in our permanent magnet system. We obtained excellent fits for the expected position dependence of the magnetic field for the permanent cylindrical magnet (Fig. 5.3). This value sets the relevant range of magnetic fields for the magnetometry measurements of the microbeads and nanorods. We measured the magnetic characteristics of the particles to enable the calculation of the magnetic driving forces applied during magnetophoresis experiments. Using the SQUID magnetometry

data we determined that, at low fields, the volumetric susceptibility of MyOne beads was 0.86 ± 0.02 (Fig. 5.2). From these measurements, the MyOne beads magnetically saturated at an applied field of 0.5 T and had a saturation magnetization M_{sat} of 53 ± 1 kA/m.

For the nickel nanorods we found the volumetric susceptibility was 18.3 ± 0.3 based on magnetometry measurements and the pore density of the membrane (Fig. 5.2). This value incorporates a normalization factor (Meehan, 2007) derived from reports of the magnetic characterization of similar rods by other researchers (Ciureanu et al., 2005; Encinas-Oropesa et al., 2001; Hultgren et al., 2003; Li and Lodder, 1990) and accounts for the influence of the rod packing density on the measured magnetization. In addition to the magnetization induced by the applied field, the rods showed some ferromagnetic character which resulted in a remanent magnetization of 39 ± 2 kA/m. The rods saturated at an applied field of 0.4 T and had a M_{sat} value of 590 ± 30 kA/m.

5.4.3 Magnetic Forces on Particles

Since the magnetic particles did not saturate in our transport measurements, we calculated \vec{F}_m using the magnetic characteristics of the particles (Eq. 2.91 and 2.98) and the applied magnetic field (Eq. 5.2 and 5.3). Because \vec{F}_m and \vec{F}_d for the rods should be proportional to L , we normalized the force values for each rod by dividing out L , enabling comparisons between individual rods. The predicted and experimental values of $\vec{F}_m(z)$ for both the MyOne beads and the rods agreed well within the experimental uncertainties as shown in Figure 5.6, which lends confidence to our ability to calculate

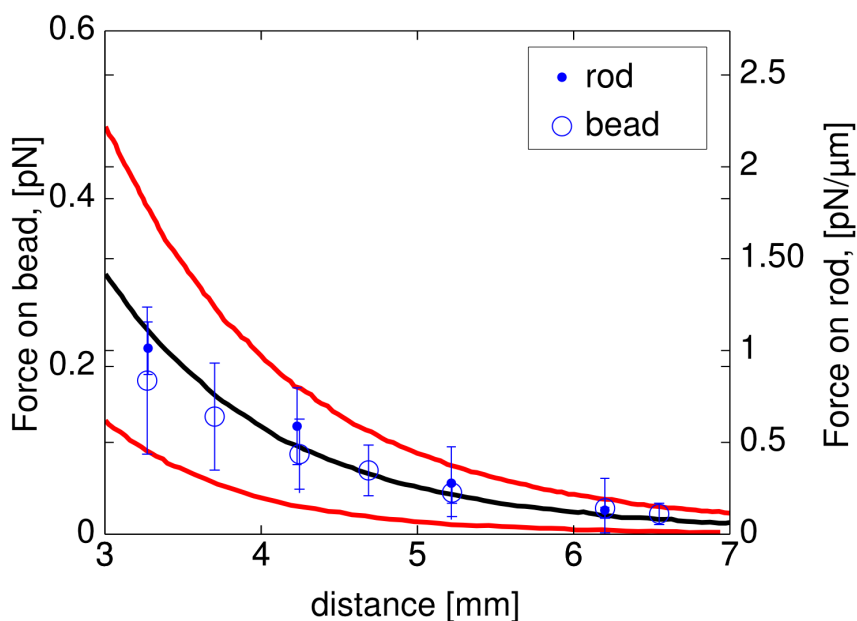


Figure 5.6: The average magnetophoretic force applied to MyOne beads (●) and length-normalized nickel nanorods (○) plotted as functions of the distance from the permanent magnet. The bars on these data indicate the standard deviation of force as calculated based on the velocities of individual nanoparticles in the Newtonian standard solution. The black solid line plots the theoretical force imposed on the beads based on the measured field and measured magnetic properties of the nanoparticles. The red lines indicate the upper and lower bounds on the uncertainty of the theoretical force.

viscosities of λ -DNA solutions by solving for the η term using Stokes drag.

5.4.4 Driven particle transport in complex fluids

To understand the nature of driven particle transport in biological fluids, we applied magnetic forces and drove MyOne beads and rods through λ -DNA solutions at 0.7 and 2.0 mg/mL. Particles experience two different shape dependent forces, one imparted by particle magnetization and is proportional to volume, and the other by drag and is proportional to cross-sectional radius and apparent viscosity, which is also geometry

dependent. To separate the effects of these two forces on transport, we first plot the particle velocity normalized by the shape dependence of the drag coefficient versus $B(z)\vec{\nabla}B(z)$, the quantity responsible for the driving force (Fig. 5.7). If the particles experienced only the shape dependent effects on their drag, and experienced the same viscosity, then their curves in the same fluid should lie on top of each other. This is approximately the case for the beads and rods in the Newtonian standard. As expected, particle velocities increase as the magnetic field and field gradient increase. Focusing on the particle transport in the Newtonian standard, we see that the nanorods achieve higher normalized velocities than the microbeads in part due to their higher magnetizations in the same applied fields. We present no data for MyOne beads in 2.0 mg/mL λ -DNA because we found no measurable displacement on experimental timescales.

Compared to Newtonian solutions, the relative transport properties of particles are dramatically different when the medium is a viscoelastic λ -DNA solution. Figure 5.7 shows that, relative to the velocity of the particles in a Newtonian fluid, the beads experience slower velocities while the nanorods experience faster velocities in λ -DNA. In λ -DNA solutions, nanorods move with more than 100 times the bead velocity compared to a five-fold increase when using the Newtonian standard. We interpret the relative differences in the driven velocities as a change in the apparent media viscosity η_{app} experienced by the particles. These differences result from the responses of the media to the shear stresses applied by the driven motion of the particles.

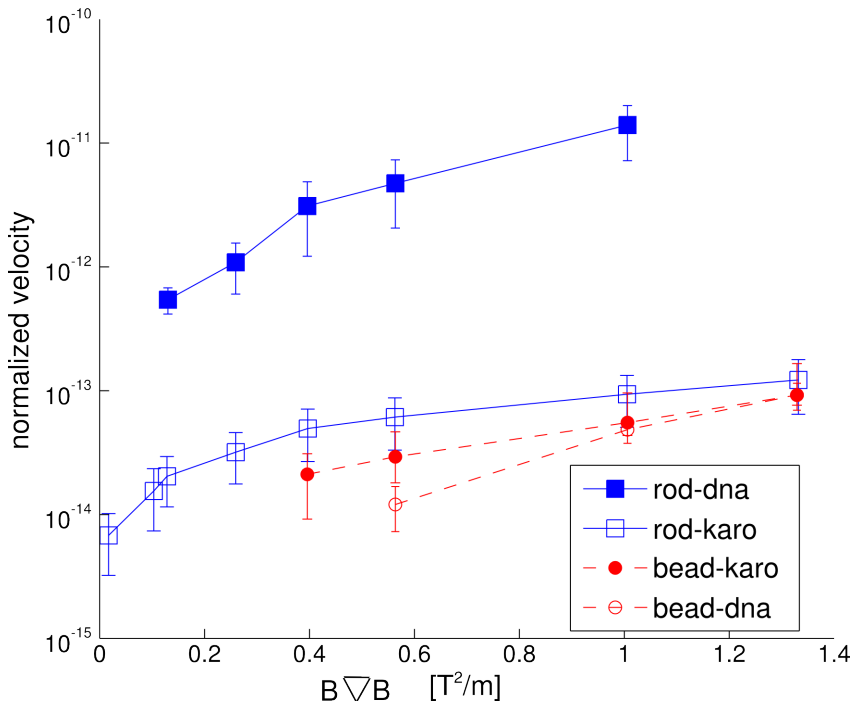


Figure 5.7: Normalized mobilities of rods (■,□) and MyOne beads (●,○) in the Newtonian solution (open symbols) and 0.7 mg/mL DNA solutions (closed symbols) as functions of the magnetic force proportionality $B \nabla B$. We normalized the particle mobilities with respect to their geometry-dependent drag and further normalized the rods with respect to their lengths in microns. The units of the normalized velocities for the rods and the beads are m^2/s per μm length of the rod and m^2/s respectively. The bars on the data points represent the range of particle velocity and do not indicate measurement error.

To investigate the driven particle induced shear thinning of the λ -DNA solutions, we plot in Figure 5.8 the apparent viscosity, η_{app} , as measured by the particles as a function of the maximum shear rate, $\dot{\gamma}_{max}$. The CAP measurements (shown as red solid lines) reveal the λ -DNA solution as a shear thinning material at shear rates greater than 10^{-1} s^{-1} . The nanoparticles (shown as discrete points) roughly reproduce the apparent solution viscosity measured by the CAP. In conjunction with the maximum shear rate, we plot the measured rod velocity normalized by length (indicated by green axis and arrows).

In contrast to the behavior of the particle motion in the Newtonian standard, the apparent viscosity of the λ -DNA solution, as derived from particle motion, indicates a power-law dependence that corresponds to shear thinning of the matrix, where fits revealed exponents of -0.8 for rods (both concentrations) and -0.6 for beads (0.7 mg/mL). These power-law exponents are consistent with those measured for λ -DNA by bulk rheological techniques. As expected in all cases, the values of η_{app} of the λ -DNA solutions are greater than the viscosity of pure buffer (10^{-3} Pa s).

p	15	105
$\beta_c/\beta_s = \left(\frac{81}{16}\right)^{-1/3} p^{2/3} (\ln(p) + v_{\parallel})^{-1}$	1.4	2.9
$F_c/F_s = \frac{8(\mu_r+2)}{3}$	56	56
$\dot{\gamma}_c/\dot{\gamma}_s = (3p/2)^{1/3}$	7.2	11.1
$\eta_c(\dot{\gamma}_c)/\eta_s(\dot{\gamma}_s) = \left(\frac{\dot{\gamma}_c}{\dot{\gamma}_s}\right)^{n-1}$	0.15	0.1
$v_c/v_s = \left(\frac{\beta_s}{\beta_c}\right) \cdot \left(\frac{F_c}{F_s}\right) \cdot \left(\frac{\eta_s(\dot{\gamma}_s)}{\eta_c(\dot{\gamma}_c)}\right)$	265	196

Table 5.2: Ratios of Particle Velocity

5.5 Discussion

With a quantitative understanding of magnetic particle transport in hand, I now relate these measurements to a set of force requirements given particle size and shape.

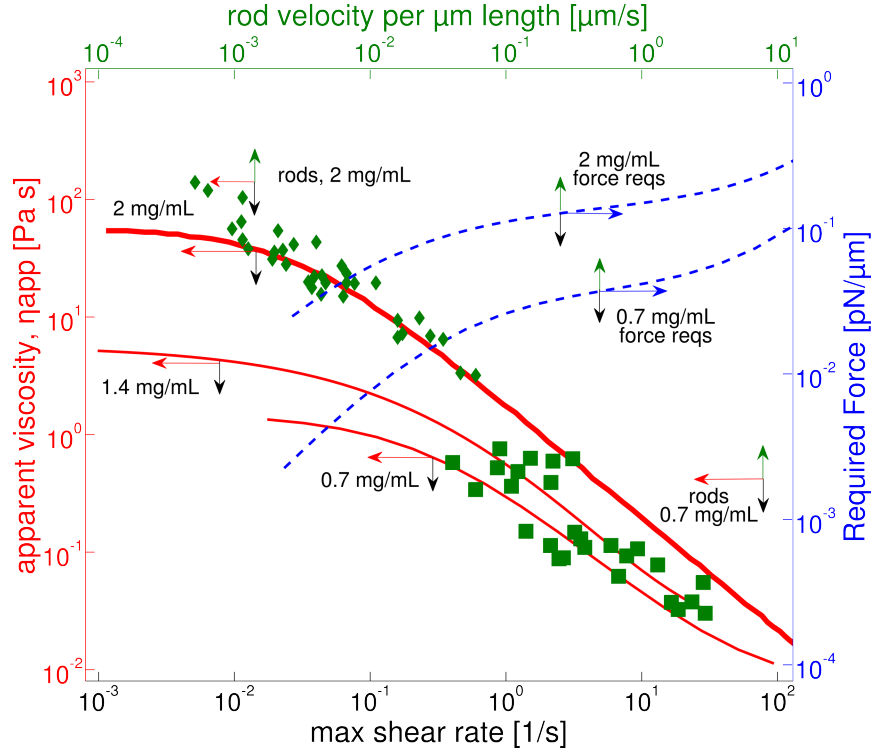


Figure 5.8: Apparent viscosity (η_{app}) as a function of the maximum applied shear rate ($\dot{\gamma}_{max}$) in λ -DNA solutions. The data shown for 0.7 mg/mL as the solid, red line are macroscale measurements from Heo and Larson (Heo and Larson, 2005). Corresponding lines for 1.4 mg/mL and 2 mg/mL concentrations are CAP measurements by our lab and extrapolated values, respectively. Shown as discrete data points is η_{app} as experienced by magnetophoretically driven rods (\square, \blacklozenge) in 0.7 mg/mL and 2 mg/mL solutions. The decrease in η_{app} with increasing $\dot{\gamma}_{max}$ indicates shear thinning. Also shown are force requirements (blue lines) for translating a 1 μm long rod with a 100 nm diameter through 0.72 and 1.44 mg/mL DNA solutions as a function of shear rate. Because the DNA solution shear thins, small increments in force yield much higher particle velocities than expected because of the shear thinning effect.

In Figure 5.8, I show the generated force requirements for a 1 μm long rod, driven through 0.7 and 2 mg/mL λ -DNA solutions (shown in blue, dashed lines), alongside the plotted viscosities and their dependence on velocity and shear rate (shown in red). These lines indicate the force necessary to achieve a shear rate or velocity (black/green) when one expects a given shear dependent viscosity (red). For example, to deliver a

rod within the shear thinning region of λ -DNA at 2.0 mg/mL with a 10 μm rod at 1 s^{-1} , find the shear rate along the x-axis and locate the expected viscosity; for this example, the viscosity is 1 Pa s, well within the shear thinning regime for this material. At this shear rate, also note the force requirement for each concentration. For 2 mg/mL λ -DNA, one applies approximately 3 pN/ μm to achieve the desired shear rate, whereas 0.7 mg/mL λ -DNA requires on 0.3 pN.

There are a variety of physiological contexts where shear thinning particle delivery may be useful. Here we discuss three: extracellular matrix, mucus barriers and synovial fluid. In the context of particle delivery through tissue, Lai et al. used canonical CAP methods to measure bovine-hide collagen viscosities as high as 400 Pa s (Lai et al., 2008). Kong and Vazquez measured the viscoelastic properties of gelled collagen used as an extracellular matrix simulant and found shear thinning at 0.05 s^{-1} with a zero-shear viscosity at 1 Pa s (Kong and Vazquez, 2008). Particle delivery through mucus is important for pulmonary or cervical delivery of drugs. Besseris and Yeates utilized rotating magnetic micron-sized particles to measure a zero-shear viscosity for canine tracheal mucus that lies between 10 - 7500 Pa s (Besseris and Yeates, 2007) and measurements by Powell et al. (Powell et al., 1974) showed that mucus can thin at shear rates greater than 1 s^{-1} . Our measurements in solutions of DNA are relevant to measurements of mucus rheology because large amounts of DNA are found in pathological (i.e. CF) sputum (Rubin, 2006). Heo and Larson demonstrated that the application of shear stress results in shear thinning in λ -DNA at the macro-scale where the measured viscosities are diminished by an order of magnitude or more (Heo and

Larson, 2005). Delivery of drugs to or through cartilaginous tissue requires particle transport through synovial fluid and corresponding measurements by Jay et al. (Jay et al., 2007) in bovine synovial fluid found thinning at shear rates greater than 0.1 s^{-1} . For the purposes of determining a proper applied force regime, the materials we first consider the zero-shear viscosity limit. Initially, to achieve a 100 nm/s velocity, a 200 nm diameter rod would require forces ranging from 0.4 to $300 \text{ pN}/\mu\text{m}$. This velocity would correspond to a shear rate of 1.5 s^{-1} , and would be sufficient to engage shear thinning in any of the biomaterials enumerated above. A bead with the same volume (and thus equal payload) and made from the same magnetically-permeable material would require 3 to 5 times more force to achieve similar shear rates. To achieve this same magnetomotive force, $(B \cdot \nabla) B$ would need to be 75 times higher (assuming no saturation), and therefore require a larger or closer permanent magnet. Choosing rod-shaped particles as drug carriers becomes obvious when one considers the impact of the lower required magnetic fields and field gradients.

A functioning apparatus may not require very large and unwieldy magnets positioned uncomfortably close to the patient's body. In this report, we used a rare-earth permanent source magnet that was relatively small, (2 mm diameter, 1 inch length) which generated a shear thinning flow for rods at distances as far away as 5 mm in a fluid with rheological properties comparable to healthy mucus. In terms of source magnet design, the force generated varies minimally with respect to changes in aspect ratio of the magnet. However, increasing the radius of the magnet leads to an increased force and increased penetration depth of the force. In fact, to achieve maximum force at

a given depth, a magnet with a radius of about twice the desired depth is required, but the maximum force for a given depth is not necessarily required to achieve significant shear thinning. As the magnetomotive force depends on the product of the field and field gradient, the force generated by a cylindrical magnet scales as z^{-2} at distances larger than twice the diameter, where z is the distance from the face of the magnet. Our calculations indicate that shear thinning in 2 mg/mL λ -DNA can be achieved at depths typically seen in the lung (~ 1 in) (Seddon and Snashall, 1989) with a NdFeB source magnet as small as 20.5 mm in diameter and 20.5 mm long. We used the magnetization value of our experimental source magnet to calculate that a magnet with these specifications and using our nickel rods with a radius of $0.1 \mu\text{m}$ and $1.5 \mu\text{m}$ in length would produce about 0.11 pN of force. As shown in Figure 5.8, the force produced would lead to a 100 fold decrease in viscosity in 2 mg/mL λ -DNA, a relevant model for infected mucus (Rubin, 2006). In the context of a drug delivery system, the velocity of the rod shaped particles would be on the order of $1 \mu\text{m/s}$ and can therefore traverse the approximate length of the mucus layer of the lung epithelia in seconds and the typical length of a mucus plug in a matter of minutes. If the material did not shear thin and instead exhibited only the zero shear viscosity, the same particle would travel 1000 fold slower, and therefore take 1000 times longer to reach the desired displacement.

Shear thinning of mucus by these micro-particles opens up a myriad of possibilities in drug delivery, specifically inhalation delivery. Two main pathways exist for the clearance of particles transported through the respiratory epithelium: the mucociliary clearance system and alveolar macrophages (Groneberg et al., 2003). The

internalization of carrier particles by alveolar macrophages has been shown to be heavily dependent upon particle size. In fact, using carrier particles smaller than $0.26\ \mu\text{m}$ in diameter, which are within the parameters of the experiments described here, avoids macrophageal phagocytosis altogether (Holma, 1967). By designing a drug delivery system that takes advantage of the shear thinning of mucus to increase particle transport rate, the problems arising from mucociliary clearance can be obviated, increasing bioavailability of the drug in the lungs. However, in order to get net transport, the particle motion through the mucus layer to the epithelium would need to compete with the mucociliary clearance rate, which in a normal human trachea is $200\ \mu\text{m/s}$ (Yager et al., 1978). Magnetic driven transport in this case may tilt the balance toward effective transfection.

5.6 Conclusions

By using solutions of λ -DNA within the entanglement range, we demonstrated that the transport of magnetically driven nanoparticles can induce shear thinning of a polymer network, indicating that driven particles experience viscosities in biological materials that are significantly less than the bulk material viscosities as measured under zero-shear conditions. Consequently, predictions based on zero-shear viscosity assumptions alone overestimate the force required to obtain sufficient particle transport. This finding has practical implications for a host of biomedical applications ranging from drug delivery to hyperthermic therapies, where the rapid particle transport with mini-

mal driving force is essential.

We fully characterized the magnetophoretic system used in this study, calibrated it using a Newtonian fluid standard, and confirmed our calibration with SQUID measurements. This enabled us to predict and quantify magnetic driving forces and viscous drag forces on individual particles. We found that magnetic fields and field gradients required to transport a rod-shaped geometry are reasonable in that large magnetic systems are not necessary to impart sufficient force. Our source was a widely available rare earth (NdFeB) permanent magnet and the distance between particles and magnet was in the millimeter to centimeter range, a relevant scale of driving forces considered practical for biomedical applications. The combination of a magnetically-driven system, fully characterized probe particles, and a non-Newtonian medium comprises a generic framework for performing drug-delivery studies.

Chapter 6

Strain Thickening

6.1 Overview

In vivo, it is the constant beating of cilia that drives the mucus flow responsible for maintaining sterility in the lung. The interaction between the rapidly moving cilia tip and the viscoelastic mucus layer is largely unknown yet is critical for understanding the role of viscoelasticity in mucus clearance including the failure of clearance when mucus becomes excessively dehydrated. In this chapter I study related phenomena using driven microbead rheology (DMBR). By placing a magnetic micron(s)-diameter bead into polymeric solutions and applying forces, I can generate shear rates representative of cilia. In these data, we will find that sometimes under a constant force a spherical bead in a shear thinning entangled polymer solution experiences a sudden and substantial (> 200%) increase in velocity. The first and slower quasi-steady state behavior corresponds in compliance space to a linear viscoelastic model such as a Jeffrey model. The bead then experiences an acceleration presumably due to viscosity changes in the vicinity of the bead surface. I present this velocity increase as associated with known experimental

work on transient viscosity overshoots (i.e. strain thickening) in polymer solutions during the startup of shear flow. The increase in viscosity for the work mentioned is about a factor of two and occurs at a constant material strain (Hur et al., 2001). I use a Stokes flow continuum approach to model and characterize the instantaneous shear velocity in the field around the bead as it moves through an incompressible liquid. This velocity allows us to calculate the Weissenburg number (Wi) for a field around the bead. The bead must satisfy two criteria to exhibit this sudden increase in velocity: Wi needs to be above a critical value (~ 10), and the total strain experienced in the local neighborhood of the bead (calculated from integrating the local shear rate over time in the sphere of influence surrounding the bead) needs to exceed another critical value ($\sim 3 - 4$). I then determine the dynamic viscosity field and model the expected properties of the surrounding polymer solution.

To show the generality of this phenomenon empirically, I used DMBR to measure the rheological properties of several biopolymer solutions. In Chapter 4 I presented DMBR measurements on 10 mg/mL HA with 2.8 μm beads, where the response indicated a linear viscoelastic fluid with a steady-state viscosity of 10 Pa s, a value equivalent to CAP (Figure 4.10b, *inset*). λ -DNA solutions probed with 2.8 μm beads exhibited a quasilinear response for small input forces that can be interpreted as traditional shear thinning behavior between pulls (Figure 4.8). However, when tested with 1 μm beads, a non-linear increase in bead velocity occurs which I propose is from the bead overcoming a local strain-thickening field.

Finally, I consider cilia as a physiological system where this dynamic strain thick-

ening phenomenon may be responsible for successful mucus transport. This dynamic strain-thickening phenomenon has been observed in several of our test solutions: DNA, guar, porcine gastric mucus (PGM), human sputum, and human bronchial epithelium (HBE) mucus. Additionally, strain-thickening could also have beneficial implications in magnetophoretic drug delivery as well.

6.2 Introduction

The driven microrheology technique can measure the viscoelastic properties of polymer systems, with much of today's interest placed on systems of biological origin or relevance. Many questions regarding the responses of these soft materials to active or driven microrheology techniques have yet to be answered. Typical approaches attempt to quantify rheological parameters and compare them to macroscale techniques such as cone and plate for validation (Schmidt et al., 2000; Mason et al., 1997; Mason et al., 1998; Schnurr et al., 1997). While this may not be the best approach, it works so long as the probe diameter is larger than the dominating length scale, correlation length, in the polymer system (Gittes and MacKintosh, 1998). Measurements using thermal diffusion track particle displacements as a function of time without any externally applied force and as such are limited to probing only the linear properties of the polymer system. Alternatively, experiments that take advantage of applied forces (like DMBR) have the potential to measure linear and nonlinear material properties and are not always expected to follow from macro-scale to smaller, microscale measurements

(Squires, 2008). Understanding the results of experiments such as these requires understanding the phenomenological, continuum-based interpretation commonly found in macroscale measurements as well as the polymer physics, molecular-based approaches found in microscale measurements.

6.3 Background

A material's rheological profile depends on the time and length scales inherent in the material itself in addition to those which correspond to the measuring probe (Gittes et al., 1997). When measuring macroscale properties, such as those obtained with regard to cone and plate (CAP) rheometry, this distinction is largely unimportant because of the vast difference between the time-length scales of the probe compared to those of the test material. Once these time-length scales converge, the properties measured by the probe diverge from the properties of the macroscale material, as documented in many places in the current literature (Gittes et al., 1997; Waigh, 2005).

The community often implicates this discrepancy between the large and small scale measurements as a constraint, limiting the ability to measure material properties to a predefined volume and/or geometry. This constraint will certainly be true when considering the length scale over which heterogeneity in the material presents itself. Indeed, the microrheologist must consider the probe itself when making any measurement in order to discern an accurate response for that particular time-length scale. Two significant length scales for the lung are the length scales of cilia (200 nm, 10 Hz) and those

of invading bacteria (1-2 μm , $\sim 50 \mu\text{m/s}$) (Schneider and Doetsch, 1974).

Not only are there discrepancies between passive measurements, but several are documented in the literature for active microrheology techniques (Squires, 2008). Because the time-length scales traversed by the bead are longer than for diffusion, and because of the similarities in driving functions, the response of particles in DMBR are expected by and large to converge and correspond to macroscale techniques, which is true in many cases (Mason et al., 1997; Ter-Oganessian et al., 2005; Wilking and Mason, 2008; Waigh, 2005).

In this work I document an example of a dynamic nonlinearity in DMBR and define its origin as a strain-thickening response of the medium to the particle's motion. This non-linearity is expected to be ubiquitous in polymer systems at or above the entanglement concentration, c_e , i.e. the semi-dilute, entangled regime.

I start with an exploration of the empirical DMBR data and then diagram the typical response of the dynamic strain thickening event (DSTE) as probed by the magnetic bead. Next, I explore the environment immediately surrounding the bead and derive the expected apparent viscosity field as a function of Weissenburg number, with the longest time scale of the material, λ , first determined by CAP rheometry. Using this approach I model the strain-thickening phenomenon surrounding the bead and explain how the material response the bead “sees” is not necessarily the same response reported as the macroscopic scale.

6.4 Nonlinear active microrheology

Active microrheology experiments have a rich history with the earliest known documented work taking place in the 1920s (Gardel et al., 2005). Most work done in the past 15 years have used actin solutions (Ziemann et al., 1994) or was performed directly on cells (Bausch et al., 1998). Some of the latest work done on polymerized actin networks interprets results as an osmotic pressure effect (Uhde et al., 2005a). Nonlinear behavior in microrheology experiments has been previously shown in colloidal suspensions, where a shear thinning phenomenon created an almost 50% reduction of zero-shear rate viscosity (Meyer et al., 2006). More recently, a non-linear effect was interpreted as a yield strain for well-entangled collagen solutions that matched macroscale results, previously unreported in the literature (Wilking and Mason, 2008). Challenges arise in interpreting DMBR results and reconciling them with CAP measurements because of the heterogeneous and unsolved nature of fluid flow around driven spheres, and/or determining if they are probing qualities of their environment that may not be resolvable by macroscale techniques. (Squires, 2008).

In Chapter 4 I found shear thinning to carry over into soft biopolymer solutions and in Chapter 5 I reported on the effects of shape for perceived viscosity in the context of drug delivery.

6.5 Materials and Methods

I obtained the non-linear compliance response functions of entangled biopolymer solutions including λ -DNA, Hyaluronic Acid (HA), commercially available Porcine Gastric Mucus (PGM), and guar using DMBR. Described in detail in Section 2.4, I applied to 1 μm and 2.8 μm beads repeated rectangular force pulse trains with 0.2 s to 15 s durations and amplitudes ranging from 1.5 to 200 pN. Bead displacements varied from a typical linear viscoelastic response to grossly non-linear behavior in the form of shear thinning and strain thickening as the bead probes the entangled polymer solutions and perhaps travels into new material. Using steady state bead velocities I can replicate in driven microbead techniques the power law dependence of viscosity as a function of shear rate as seen in macroscale cone and plate techniques. Using a fluid dynamics approach I also modeled the fluid immediately surrounding the sphere with the Rolie-Poly model (Likhtman and Graham, 2003; Teixeira et al., 2007). The RP model qualitatively reproduces the increase in viscosity, and its quantitative results depend on the interpretation of time scales found in either CAP or DMBR.

6.5.1 Probes

The magnetic particles used in this study were monodispersed, superparamagnetic (SPM) microspheres (Invitrogen, Carlsbad CA) that had diameters of 1 μm (MyOne[®]) or 2.8 μm (M-270). Bead size was confirmed by in-house SEM measurements as in other studies (Figure 5.1(a)). Both bead sizes were originally surface-coated with terminal

carboxyl groups by the manufacturer and were either used in this form, or were PEGylated in-house (for the PEGylation protocol, see Appendix A.2) to reduce bead-polymer interaction as well as bead-bead aggregation.

6.5.2 Solutions

The preparation of all solutions as functioning polymer systems is documented in detail in Sections 4.3 through 4.5. The UNC CF Center graciously donated samples of HBE mucus specimens which were obtained by collecting the washings from HBE cell culture over a period of several weeks and concentrating the resultant fluid by methods explained by Matsui, et al. (Matsui et al., 2006). The final material usually has concentrations between 2.5% (considered “normal”) and 8% (considered “CF-like”) solids as measured by dried weight. Specimens of induced or expectorated human sputum come directly from patients following HIPAA standards and stored at 4°C.

6.5.3 Light Scattering

The results of light scattering measurements were described in detail in Sections 4.3 through 4.6 and were performed using a Dawn multi-angle laser light scattering apparatus (MALLS) coupled in line to an Optilab refractometer (Wyatt Corp.). For all polymer solutions save DNA, the light scattering measurements allowed for the computation of their respective physical properties, with that data presented here in Table 6.1. For the λ -DNA data shown in Table 6.1, the M_w is from the package insert and the R_g computed using 50 nm as the persistence length (Rubinstein and Colby,

2003) and WLC model assumptions.

	units	λ -DNA	HA	guar	PGM
M_w	MD	32	0.29 ± 0.01	13.7 ± 0.2	56 ± 2
R_g	nm	520	104 ± 3	190 ± 10	310 ± 30

Table 6.1: Measurements of Molecular Weight and Radius of Gyration.

6.5.4 CAP Methods

In shear thinning materials, the apparent viscosity depends on applied shear rates that exceed a time constant. To test for this behavior a flow curve or viscometry test is performed where a steady state strain rate is measured for a given input stress. The apparent viscosity for samples of λ -DNA at 0.7 and 1.4 mg/mL were measured as a function of shear strain rate. Measurements similar to these were made by Larson in 2005; the data from that paper are also plotted here, showing good agreement.

With the 40 mm cone in position on the TA Instruments AR-G2 stress-controlled rheometer, 330 μ L of sample was loaded onto the peltier plate set at 23 °C. The peak hold protocol was used with a feedback-controlled shear rate and measurements were made by enabling the fast sampling mode. The instantaneous viscosity was measured as a function of time/strain. A Newtonian solution would exhibit a constant viscosity for any shear rate, however, we find that for certain viscoelastic materials, the instantaneous viscosity exhibits an overshoot and then subsequently settles down to a steady state value.

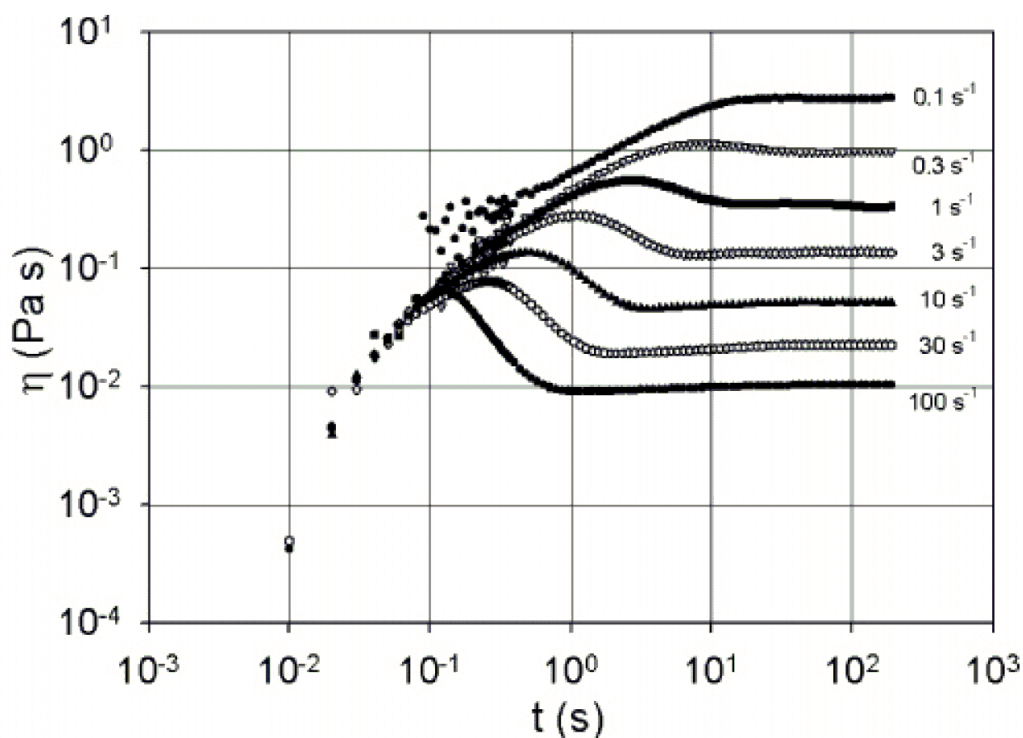


Figure 6.1: Viscosity overshoots in 1.5 mg/mL λ -DNA from Teixeira, 2007. The cone is turned at constant shear rates with a strain-controlled rheometer for a range of strain rates from 0.1 to 100 s^{-1} . In time, the maximum viscosity occurs at different times, but at approximately constant strain. For a $\dot{\gamma} = 0.1 \text{ s}^{-1}$ the overshoot is minuscule, barely detectable by the instrumentation. The overshoot in η occurs due to the stretching of chains at high Wi number. Steady state viscosities are consistent with our 1.4 mg/mL λ -DNA solution tested with CAP, DMBR, and TMBR.

6.5.5 DMBR Methods

I used force pulsed microrheometry (Ziemann et al., 1994) to measure the creep response curves for λ -DNA solutions from 0.2 s to 15 s in time. To do this, the magnetics subsystem of the 3D force microscope (3DFM) was used in conjunction with a Nikon TE-2000E microscope with a 60 \times water-immersion objective (Fisher et al., 2006a). Magnetomotive force actuates the displacement of magnetic particles embedded in the

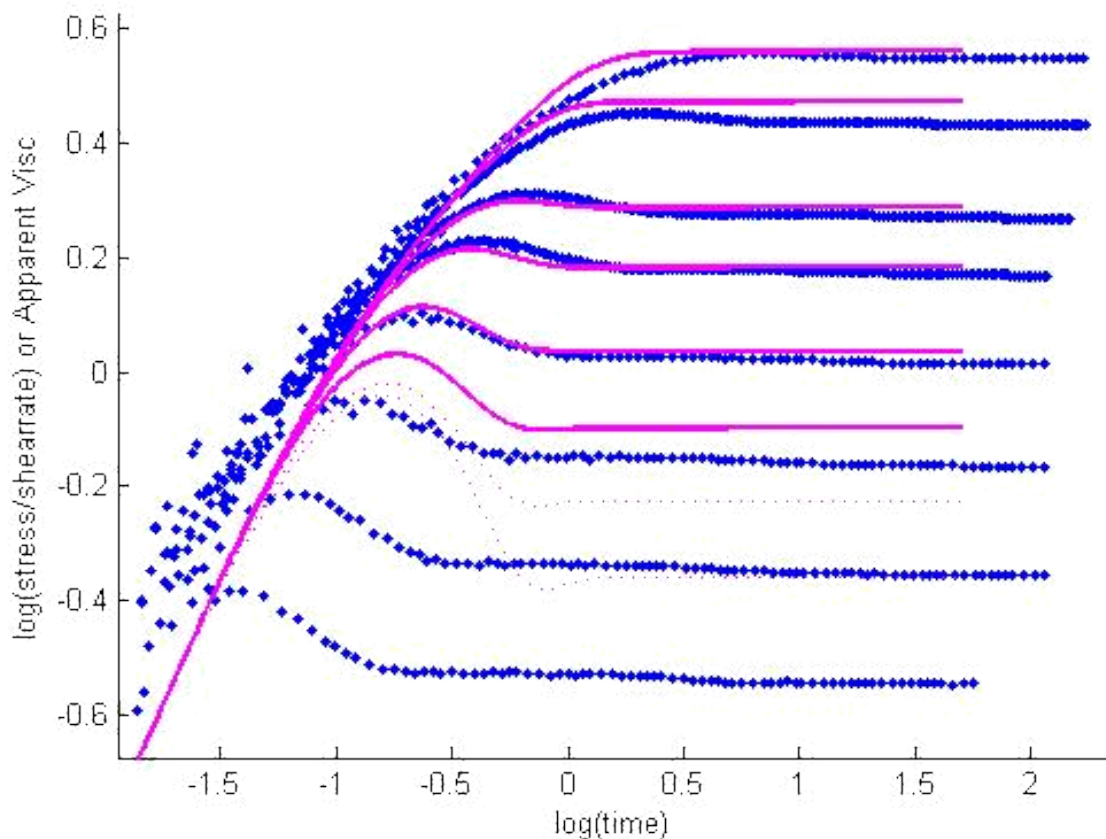


Figure 6.2: Transient viscosity overshoots in 1% guar using our TA AR-G2 stress-controlled CAP rheometer which applies step strain rates using feedback. Overshoots in viscosity occur at different times which correspond roughly to constant strain. Empirical data are indicated as blue points. Overlaid as pink lines are fits to the Rolie-Poly model.

test material. The geometry for the DMBR technique described here consists of a sharp tip opposing a flat plate with a gap distance of $550 \mu\text{m}$ mounted on a #0 ($100 \mu\text{m}$) thickness 24×40 glass coverslip (Figure 3.10). The $100 \mu\text{m}$ thick tip has a cylindrical radius that averages about $10 \mu\text{m}$ at the pole tip. A small volume of specimen ($\sim 1 - 3 \mu\text{L}$) is placed between the pole tip and plate, surrounded by silicone grease to dissuade sample drift and evaporation, and mounted inside the magnetic stage. With the 3DFM I can generate forces ranging from 1 to ~ 1000 pN on a $1 \mu\text{m}$ bead (Fisher et al., 2006a).

More detailed information about the magnetics system can be found in Section 3.4.4).

For video, I used a Jai-Pulnix PTM-6710CL progressive scan camera and a PCI-DV EDT frame grabber board which provided a video temporal resolution of 8 ms (120 frames per second). Experiments generally lasted from 10 - 600 seconds, with all images spun directly to disk. The video system is discussed in more detail in Section 3.3. For the particle tracking of microbeads I used version 5.x+ of the CISMM video spot tracker which, combined with our optics system, has a step spatial resolution of approximately 10 nm sized steps at full frame rate (Section 3.3.5).

6.5.6 Force Actuation and Extraction of VE parameters

When a step current is applied to the coils of the magnetics system, a step force, F , is generated over small excursions, $x(t)$, of the bead ($\leq 5 \mu\text{m}$) in the sampling space. The applied force to the bead incurs a drag force in the opposite direction with a geometric coefficient of $6\pi r_s$, where r_s is the bead radius. The displacement of the bead as a function of time can be converted to compliance by normalizing for the geometry and the input force amplitude, resulting in Equation 2.86 and repeated here (Ziemann et al., 1994).

$$J = 1/G = \frac{6\pi r_s x(t)}{F} \quad (6.1)$$

The linear viscoelastic properties of a viscoelastic liquid can be extracted from the creep compliance function via a fit to a Jeffrey model step response. The long-time, zero-shear viscosity is equal to the inverse of the asymptotic slope while the elastic modulus

can be approximated via the Maxwell model approximation, using the intercept of this terminal slope fit. These two estimated values are made more precise by providing them as initial guesses and calculating the least-squares fit to the Jeffrey model response function (Morrison, 2001).

I derived the maximum shear rate imparted on the fluid by the bead by taking the derivative of the Stokes flow field around a bead and computed the magnitude of the strain rate tensor at the bead surface at an angle of $\theta=90^\circ$, resulting in Equation 2.47 (repeated here):

$$\dot{\gamma}_{max}(t) = \frac{3v_d(t)}{\sqrt{2}r_s} \quad (6.2)$$

where $v_d(t)$ is the time-dependent velocity of the bead (Squires, 2008). The derivation can be found in detail in Section 2.2.7.3.

6.6 Results

I measured creep compliance by monitoring bead displacements during a succession of constant force pulses each held for a known duration of time, complete with an introductory drift estimate period. Early pulses showed little evidence of the thickening phenomenon with zero net displacement. Later pulses presented the DSTE and, after relaxation, showed a net displacement of the bead through its environment. Figure 6.3 shows an expansion of two of these pulses after the viscous mode of the material was probed. This particular pulse shows a reduction of the bead velocity (inset) to almost

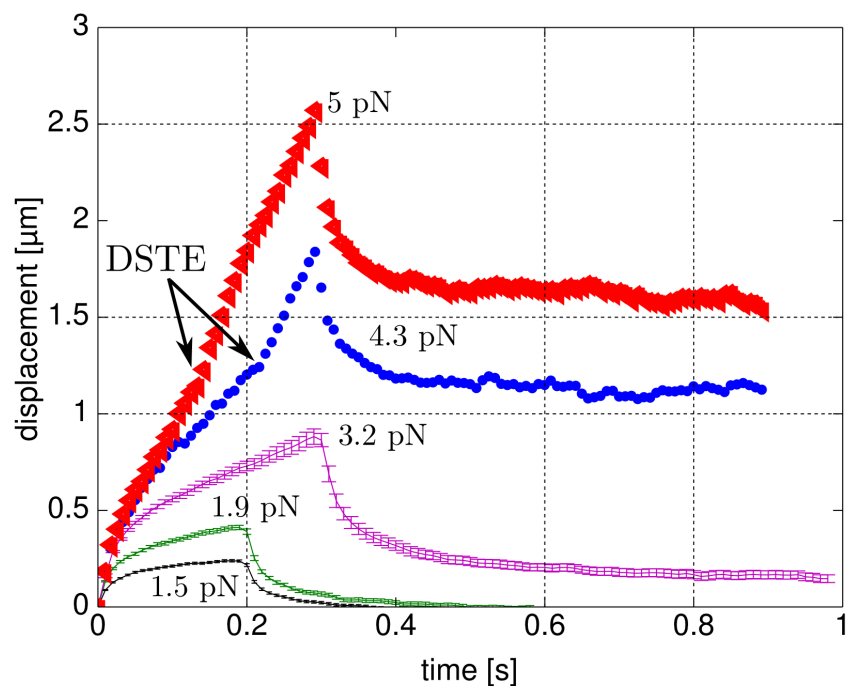


Figure 6.3: Plotted on top of data first shown in Figure 4.6 are two examples of the DSTE in 1.4 mg/mL λ -DNA. Where the previously shown quasilinear data used lower forces, these DSTE occur when higher forces, and thus higher Wi , are applied to beads. The reproducibility at lower applied forces for the same solution, indicated by error bars, shows that DSTE do not occur due to solution heterogeneity.

zero as the mechanisms of stretch and orientation in the polymer respond to bead displacement. Looking at the DSTE schematic plot shown in Figure 6.4, two phases of motion appear during the application of the input force pulse. At early times, the bead begins by moving quickly. Later, the bead slows to almost zero velocity. Next, there is a moment during the pulse where the velocity suddenly shifts from slow to fast and appears to migrate through the DNA at a constant velocity, implying a Newtonian material response to an input force. After the pulse force is completed, the bead relaxes along its original path and experiences incomplete recovery, the canonical response of

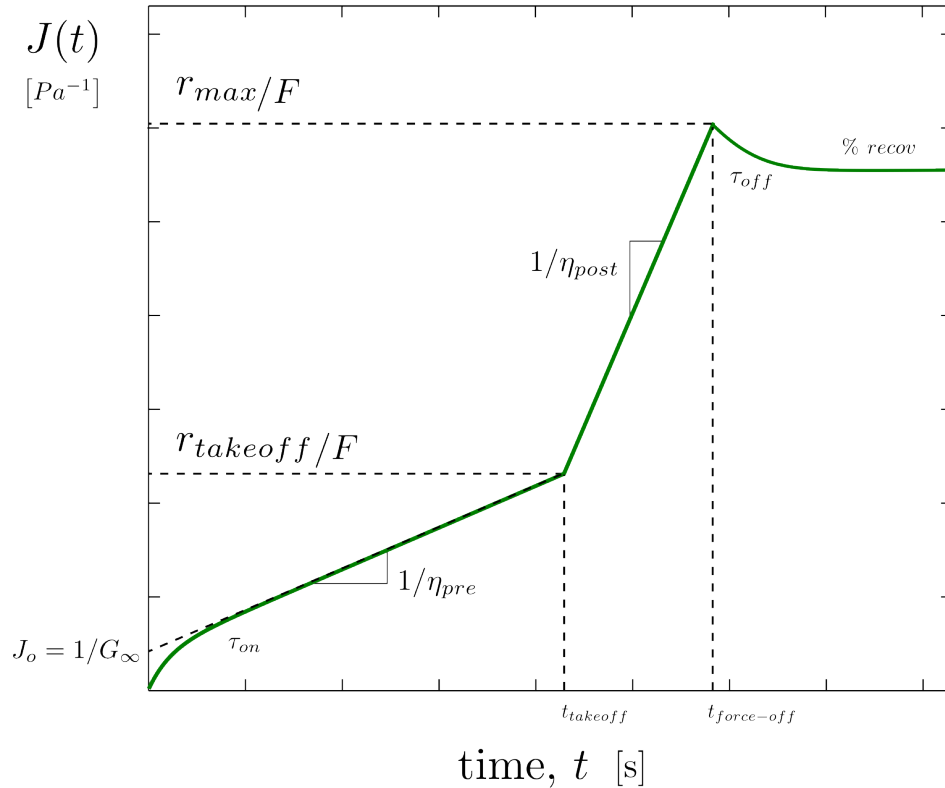


Figure 6.4: A schematic for the dynamic strain thickening event (DSTE). Early behavior is qualitatively similar to the Maxwell model step response with a zero shear compliance, J_o , equal to the projected intercept, where the slope is equal to the inverse viscosity at long times. After the DSTE, the velocity of the bead is mostly constant with an estimated viscosity again equal to the inverted slope. The time constant for the forced period, τ_{on} , is approximately equal to the relaxation time constant, τ_{off} . Recovery is never complete in datasets such as these.

a viscoelastic fluid. The relaxation time of the recovery period is approximately the same as the forced period, regardless of whether the bead samples a well-trod location or a completely new space.

Changes in slope were distinct and easy to see within the displacement data. The new velocity, established as steady state, corresponds to a viscosity and a shear rate found in the macroscopic cone and plate data (See Figure 4.8). The possibility of

the shift in velocity being system noise is rejected by the fact that immobilized beads (Figure 3.6) or beads moving in Newtonian fluids (Figure 3.12) show no sign of the DSTE.

6.7 What the DSTE is NOT

In this section I present a set of phenomena that at first glance might explain the DSTE. For each I show through experiment or modeling why these proposed explanations are incorrect.

6.7.1 Edge Effects

The first and easiest explanation for the DSTE assumes that the bead interacts with the boundary of the sample cell, where zero-velocity boundary conditions apply. If the bead begins its journey near a side wall and induces a compression by moving towards the wall, the bead is expected to slow until it hits the wall, because it must push the intervening dna strands out of its path. No reason for a sudden increase in velocity such as those seen in these data is known. Moving away from the wall might result in an increase in velocity, but this should be a smooth transition, whereas the DSTE often has a sharp transition. If the bead is close to the upper or lower specimen surface, and the bead moves appreciably in the z direction away from the surface, one might see a net increase in bead velocity, but again this should be a smooth transition.

Experimentally, these concerns are easily remedied by only choosing to actuate

beads that are more than 10 bead diameters away from any surface. All beads tracked in these experiments are 10 to 50 bead diameters away from any edge. Therefore, these DSTE do not occur as a result of edge effects.

6.7.2 Local Concentration Inhomogeneities

Local DNA concentration inhomogeneity is possibly an explanation for some of the data collected in these experiments. If these spatial inhomogeneities are larger than the size of the bead, the bead could move into a volume element where there is no polymer; it would “snap” from its polymer-laden volume into a free space, much like a rabbit might escape from a particularly dense brier patch and into a meadow. Free to move through solvent, the bead would move at a constant velocity. Eventually, however, the bead should encounter another volume element containing polymer (and the rabbit another brier patch) and initiate another viscoelastic response. If the spatial inhomogeneities are smaller than the size of the bead, there should be an oscillatory signal on top of the gross viscoelastic response as the bead passes through regions of relatively high and low polymer concentration. This type of expected behavior can be seen when using DMBR on a visually heterogeneous sputum sample found in Figure 4.14c&d. Not only do the curves not collapse when in compliance space, they appear to have large swings in their velocity from slow to fast, as seen in DSTE but with substantial slowing thereafter. Beads moving at high velocity can also suddenly slow. Both of these events happen at length scales much larger than the bead size, denoting great spatial heterogeneity between pulls.

What concentration inhomogeneities cannot explain is a recovery response inside an empty pocket, where only solvent touches the bead. In every response there is a recovery; if the force on the bead was removed while the bead was in a solvent pocket, no recovery should be seen. If there is a lower concentration of polymer inside the new pocket, the relaxation times should slow, but the opposite tends to occur when the DSTE begins to manifest itself. Because of these reasons it is probably safe to assume that local concentration inhomogeneities are not responsible for the DSTE.

6.7.3 DNA Sticks to Bead

Another possible reason for the DSTE is electrostatic interactions between the polymer and probe surface. Such an association might increase the apparent hydrodynamic radius of the probe when the polymer arranges itself into a surrounding semi-ordered structure. Alternatively, there may be a strong dissociation between polymer and probe, creating a polymer depletion region around the probe. For the molecules I have tested and for all the probes I have used here, the surface charge is always negative or neutral, implying the tendency for the development of a depletion region. To avoid this I PEGylate the surface of the probe [A.2](#). Even so, experiments with λ -DNA show no preference or change in the DSTE when testing with PEGylated or non-PEGylated probes. For these reasons, surface interactions do not cause the DSTE.

6.7.4 Dynamic Instability

If the model were simplified such that the DNA strands in solution were viewed as a continuum viscoelastic material subjected to shear, the takeoff phenomenon could be explained by a dynamic instability. The maximum shear rate experienced by material at the bead surface is defined as Equation 2.47. Rearranging the equation for velocity and substituting into Stokes equation results in

$$F = 6\pi r_s \eta v = 2\sqrt{2}\pi r_s^2 \dot{\gamma} \quad (6.3)$$

Solving for viscosity:

$$\eta(\dot{\gamma}) = \frac{F}{4\pi r_s^2 \dot{\gamma}} \quad (6.4)$$

A canonical curve used to describe shear thinning is plotted in Figure 6.5 and shows the dependence of the materials apparent viscosity on the applied shear rate. For a Newtonian fluid where there is no shear thinning, the result would be a constant viscosity. For non-Newtonian materials, this results in a curve with three linear regions in log space. The initial flat regime is the zero-shear regime; here the polymers in the material have not been subjected to enough energy to stretch the entropic springs and/or align themselves in the direction of the flow field and thus remain in randomized configurations. Once the shear rate reaches the time constant of the material, the polymers begin to align in the direction of flow and the apparent viscosity decreases. This begins the shear thinning regime whose quasilinear slope corresponds to the power

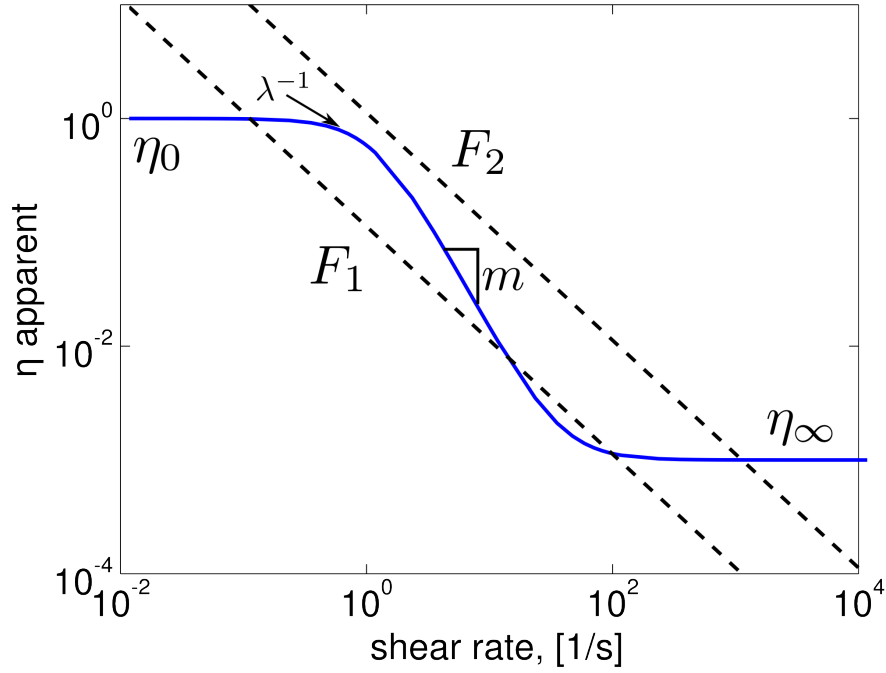


Figure 6.5: Dynamic Instability

law dependence for the material (Colby et al., 2007; Hackley and Ferraris, 2001). Once all the polymer strands are aligned in the direction of flow, the viscosity is at its minimum and does not change for any increase in shear rate; this is the third regime.

$$\frac{\eta - \eta_{\infty}}{\eta_0 - \eta_{\infty}} = \frac{1}{(1 + \lambda\dot{\gamma})^m} \quad (6.5)$$

Shown in Equation 6.5 is the Cross model which attempts to describe the shear thinning dependence on shear rate where the power-law dependence $m \leq 1$.

For the microbead experiments, a given force results in a line of force in flow space (see Figure 6.5) with an inherent slope of -1. Each force line describes measured viscosities as the result of a known shear rate (velocity, force).

The data to support a model such as this are shown in Figure 4.8. The force exerted on the bead is predetermined by calibration, so any change in shear rate (velocity) is due to a change in viscosity. The pink data points show the measured viscosity via 1 μm beads. Some of the data are shown in pairs, where a pair is measured viscosity before and after a takeoff event. Prior to the takeoff, the shear rate around the bead is relatively low, resulting in a higher viscosity. The power law slope matches the cone and plate data (shown in blue). Shown in yellow are the data reported in (Heo and Larson, 2005) for 0.72 mg/mL λ -DNA.

The slope of the Cross model is defined as a “dimensionless constant with a typical range between 2/3 and 1” (Hackley and Ferraris, 2001); because of this, the force line and apparent viscosity functions will intersect no more than once. However, if the apparent viscosity slope approaches that of the force line falloff, there may be an ambiguity in viscosity due to heterogeneities or concentration gradients on probe-sized length scales. The shear rate is proportional to bead velocity; if the bead encounters a spatial region containing only solvent, whose viscosity is low, the bead velocity will increase for a given force. When the bead re-encounters a polymer strand, initially it will be under high shear rate (velocity) conditions, possibly aligning polymer strands and lowering the apparent viscosity (high velocity).

If changes in concentration were responsible for the sudden increase in bead velocity, then the power law slope should exceed the same regime slope for a single concentration. If the slope remains the same, it may be explained by the stretching of λ -DNA chains by the bead. Therefore, these DSTE do not occur as a result of this type of dynamic

instability.

6.8 Rolie-Poly model

The Rolie-Poly model is a tube model for entangled polymer solutions. Its derivation is complicated but can be summarized and explained physically as the follows (Likhman and Graham, 2003). Stress in the polymer accumulates due to velocity gradients in the fluid (flow). Polymer strands relax stress in the polymer through different type of strand-strand interactions, three of which are capturable by the Rolie-Poly model. The first interaction describes reptation of the entire tube as a diffusive phenomenon that releases entanglements because the chain ends have higher degrees of freedom. Secondly, the polymer may retract inside its primitive tube in a process called contour length fluctuations (CLF). Last is the process of convective constraint release, where the polymer wriggles loose from entanglements during external flow. The general form of the Rolie-Poly constitutive law is

$$\frac{d\underline{\underline{\sigma}}}{dt} = \underline{\underline{\kappa}} \cdot \underline{\underline{\sigma}} + \underline{\underline{\sigma}} \cdot \underline{\underline{\kappa}}^T - \frac{1}{\tau_d} (\underline{\underline{\sigma}} - \underline{\underline{I}}) - f_{retr} (tr \underline{\underline{\sigma}}) \underline{\underline{\sigma}} - f_{ccr} (tr \underline{\underline{\sigma}}) (\underline{\underline{\sigma}} - \underline{\underline{I}}) \quad (6.6)$$

where f_{ccr} and f_{retr} are defined by (Likhman and Graham, 2003) as

$$f_{retr}(tr \sigma) = \begin{cases} \frac{2(tr \sigma) - 3}{\tau_R}, & tr \sigma - 3 \ll 1 \\ \frac{2}{\tau_R}, & tr \sigma - 3 \gg 1 \end{cases} \quad (6.7)$$

$$f_{ccr}(tr \sigma) = \begin{cases} \frac{2\beta(tr \sigma)-3}{\tau_R}, & tr \sigma - 3 \ll 1 \\ \frac{2\beta(tr \sigma)/3)^\delta}{\tau_R}, & tr \sigma - 3 \gg 1 \end{cases} \quad (6.8)$$

All three of these mechanisms should behave as functions of accumulated strain in the polymer and on different time scales. The behavior of stress in the asymptotic limits follow logically. When the rate of deformation is much faster than τ_d and much slower than τ_R the stress should behave accordingly. Interpolating between these asymptotes yields the overall form for the equation. While this model can be made more complicated by adding temporal modes (Likhman and Graham, 2003), we assume here that the true physical behavior is dominated by one mode and can at least qualitatively predict the behavior.

6.9 Modeling a Rolie-Poly fluid around a moving sphere

In this model I take a continuum approach to the surrounding polymer solution. I make the assumption that the polymer contribution to the stress does not significantly affect the flow field in the neighborhood of the bead ($\nabla \cdot \vec{\sigma} \neq 0$). This assumption is obviously incorrect and not without flaw.

I apply a spatially well-defined Stokes solution to creeping flow of an incompressible viscous fluid and generate a flow field in space. We assume this field develops instantaneously with the beads velocity. At any point in the polymer solution, I imagine a

single volume element as a continuum, and can track its strain history as it evolves in space and time around the bead.

I then assume that each infinitesimal polymer element contributes to the apparent viscosity of the overall fluid element as defined by fits and parameterizations of the empirical data observed for this solution in simple rheological flows at different flow rates (Hur et al., 2001; Likhtman and Graham, 2003; Woo et al., 2004; Teixeira et al., 2007). Coarsely fitting experimental data and the Rolie-Poly fits is motivated by the underlying polymer physics at play (CCR, reptation, stretch, etc). I now have a field of continuous (to the resolution of our grid or interpolation) strain history, strain rate (governed by flow) and through the framework of our fits, viscosity. From this I can calculate the Weissenburg number as well as revert back to the incompressible Newtonian assumption and calculate the apparent viscosity the bead sees by summing the shear and pressure terms over the surface of the bead. Once this apparent viscosity is calculated, the velocity of the bead is assumed to update instantaneously along with the flow field and the process is repeated.

The primary goal is to model the viscoelastic environment immediately surrounding the probe. I can interpolate the material's properties in the continuum sense in an effort to replicate the empirical evidence of a strain thickening material. I used the parameters from the Carreau model to initialize values of η_0 . The infinite shear viscosity, η_∞ , defines the minimum viscosity attainable when a solution of monomers size b interact individually as hard spheres with the solvent (Colby et al., 2007; Silbert et al., 1999). I used η_∞ from the Carreau model to evaluate the first value of fluid velocity in the

domain that immediately surrounds the bead. The strain rate follows explicitly from the velocity gradient in closed form.

6.9.1 Parameters for Rolie-Poly simulations

Models were run with parameters determined from both CAP and DMBR techniques. The three material parameters used in the Rolie-Poly modeling were the plateau modulus, G_e , the retraction time, τ_R , the time scale for dissipative reptation, τ_d .

–	units	λ -DNA	guar	PGM
τ_d	s	0.28	0.74	0.91
τ_R	s	0.015	0.055	0.08

Table 6.2: RP parameters for different polymer systems.

6.10 Results

Modeling bead motion through a Rolie-Poly (RP) fluid (Fig. 6.6) results in paths qualitatively similar to the schematic in Figure 6.4 and the λ -DNA data presented in Figure 6.3. Beads pulled at very low force never experienced a DSTE, asymptoting instead to a steady-state, or constant, velocity. As the force used to pull the bead increases, the DSTE begins to manifest itself as a subtle change in the curve’s concavity. These inflection points mark the apex of the strain thickened state, the time at which the viscosity is its greatest. Post-DSTE, the bead velocity converges to a constant value.

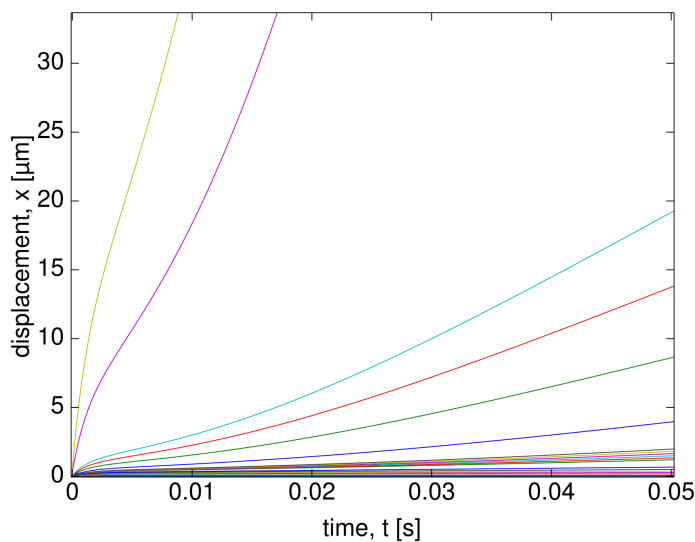


Figure 6.6: Shown in this figure are modeled displacements for a $1 \mu\text{m}$ bead in a Rolie-Poly fluid. Beads were subjected to forces ranging from 0.1 to 100 pN. The DSTE is present in pulls with forces greater than 2.5 pN. The material parameters for the Rolie-Poly fluid were chosen to closely match experimental values for the 1.4 mg/mL λ -DNA solution, listed in Table 4.2.

Normalizing the bead displacement by the applied force generates the compliance function, plotted in Figure 6.7. The curves collapsed at early times ($t < 10$ ms) but quickly diverged. Beads pulled at low force never experienced a DSTE, and a few of the lowest force pulls completely collapsed, indicating a linear response.

I assumed the long-time response was at steady-state and used the slope to compute the apparent viscosity for each pull. Following the same methodology I used in Chapter 4, I plotted the calculated η_0 versus the maximum shear rate (Fig. 6.8). The low force, small displacement curves generated the early plateau, again because of the linear response. The middle, power law region includes curves that do and do not show the DSTE. Curves in this regime that do not exhibit the DSTE show intracurve linearity,

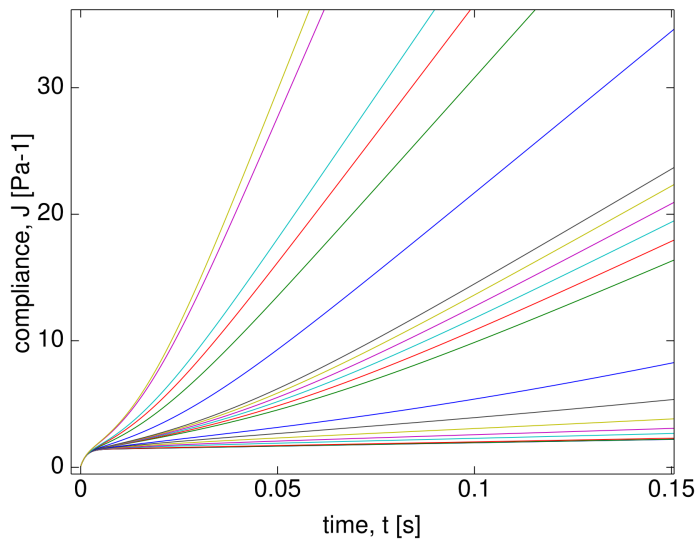


Figure 6.7: Normalizing the displacement by the applied force results in the compliance function which is shown here. For linear viscoelastic materials, this operation would result in a collapse of disparate displacement curves to a single compliance curve, like we see for HA in Figure 4.10.

where a linear Jeffrey model fits well for a single curve, but requires different parameters for a second curve. The second plateau occurs when the model begins to challenge the lower bound, η_∞ . The RP model and the empirical data (Fig. 6.9) converge at moderate shear rates. However, the zero-shear viscosities differ by more than one order of magnitude. The reason for this divergence is currently unknown.

Plotting the instantaneous apparent viscosity as a function of time results in a figure qualitatively similar to my own results in 1% guar (Fig. 6.2) as well as Figure 7 in (Teixeira et al., 2007), replicated earlier as Figure 6.1. The pull with the lowest applied force (0.1 pN) resulted in the highest final apparent viscosity. At the earliest time scales, the bead senses the solvent viscosity. For low force, small displacement

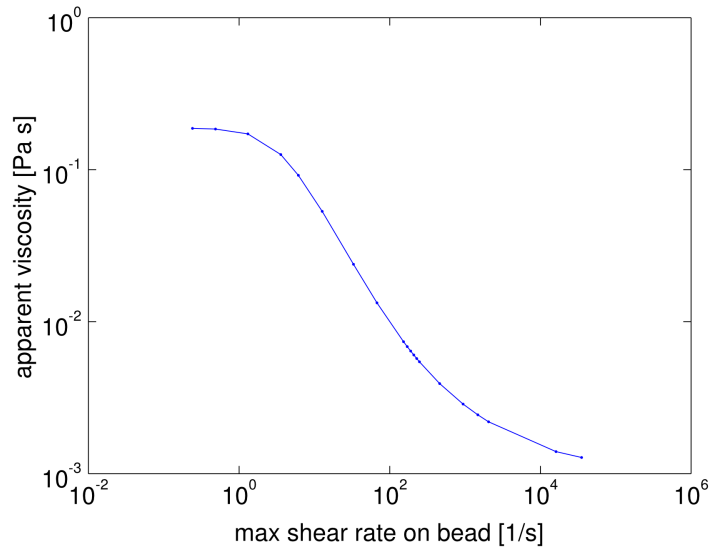


Figure 6.8: Just like the analysis used to generate Figures 4.8 and 4.13, we can recover the canonical relationship found in the CAP shear thinning curve.

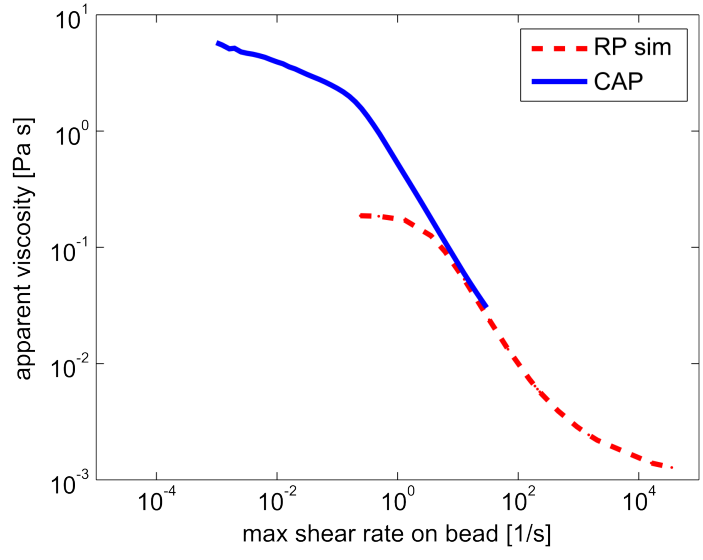


Figure 6.9: While I can recover the canonical relationship found in the CAP shear thinning curve, the RP model expects to achieve zero-shear at a much lower viscosity.

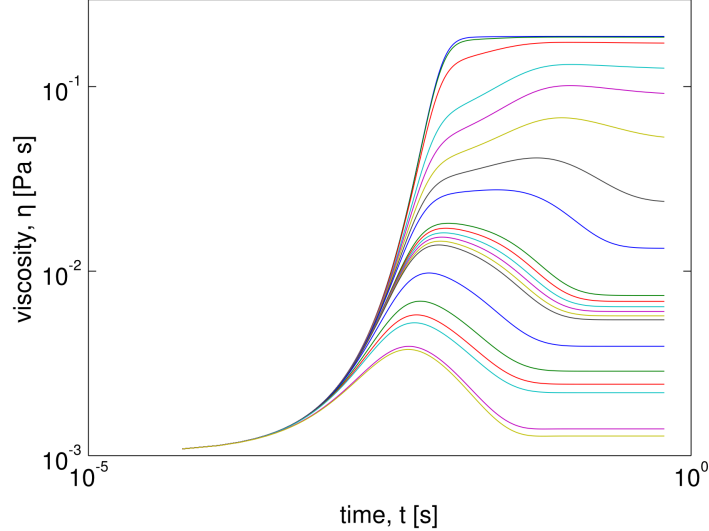


Figure 6.10: Plotting the viscosity as a function of time results in a figure similar to macroscale CAP shown by Teixeira and replicated here in Figure 6.1 for 1.5 mg/mL λ -DNA and measured by me in Figure 6.2 for 1% guar. Each line shown here corresponds to a pull shown in Figure 6.6 with a constant force. The minimum force for a pull was 0.1 pN which belongs to the data shown here with the highest steady state viscosity. These lower forces result in a simpler, linear viscoelastic response and correspond to the zero-shear viscosity plotted in the shear thinning curve in Figure 6.9.

pulls the viscosity quickly rises soon thereafter to a terminal, steady state value. As the applied force increases, the bead's response becomes more complicated, rising first to a thickened state before settling to its thinned, steady state value.

Finally, plotting compliance as a function of time for several materials, normalizing each by their maximum values, provides a look at the qualitative characteristics of each curve. In the empirical data, PGM and guar have sharper transitions than DNA and induced sputum. DNA and sputum being similar to one another shouldn't be too surprising since DNA is known to exist in sputum in large quantities. The DSTE does not transition as quickly in the modeled DNA fluid when compared to the empirical

data. This systematic error could be attributed to the order used for the RP modeling; which here is only first order. It is reasonable to assume that a higher order model could recover the sudden shift in bead velocity.

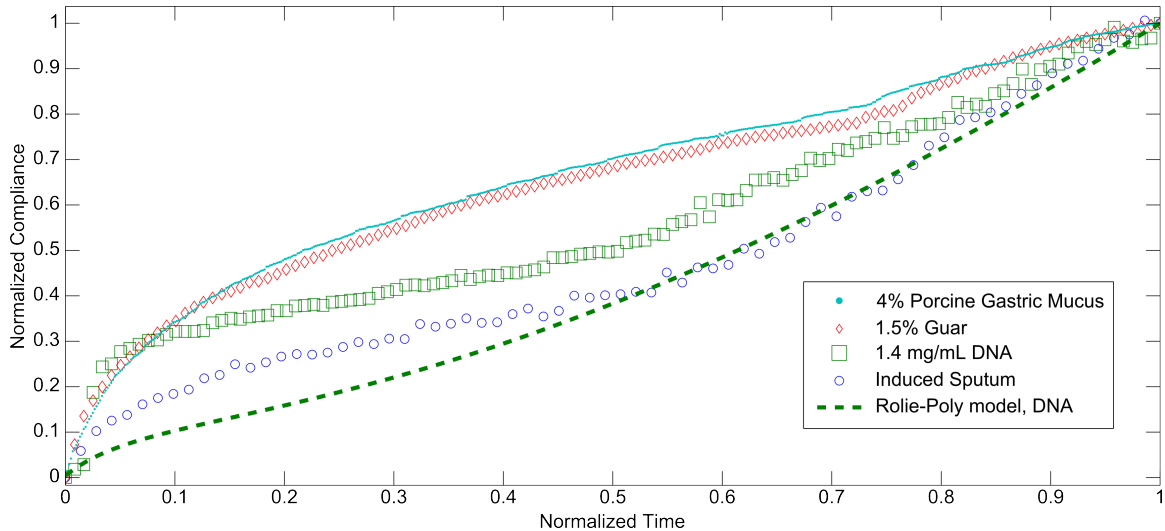


Figure 6.11: DMBR DSTE and strain thickening in four different polymer systems, normalized by the maximum compliance and time.

6.11 Discussion

Strain thickening may be relevant to understanding dynamic biological systems. Biological systems are always “on the move”— biochemical networks are modulated continuously through feedback loops, blood flows through the cardiovascular system delivering oxygen, gas exchange in the lungs keeps that oxygen biologically available and the organism in homeostasis. Also present in the lung are many billions of active cilia, increasing in relative population from the ninth bronchus generation up to the trachea. (Hubbard et al., 1991). These cilia are responsible for maintaining mucociliary

clearance, a homeostatic process where mucus, combined with pollutants and invading bacteria, is transported from the distal airways and to the trachea, finally being replaced with fresh, new mucus.

If the effective stroke length of a cilium is approximately $4\ \mu\text{m}$ at a frequency of 10 Hz, then the maximum velocity of the cilium tip would be $\approx 250\ \mu\text{m/s}$. Applying the same maximum shear rate analysis used in Section 2.2.7.3 and modeling the tip of the cilium as a half-sphere with a 200 nm diameter approximates the maximum shear rate (Eq. 2.47) applied by the cilium as $3750\ \text{s}^{-1}$ and a $Wi \gg 1$. The shear rate experienced by the fluid falls off as r^{-4} .

6.12 Conclusions

The sudden decrease in steady-state viscosity occurs repeatably in viscoelastic polymer solutions such as DNA, guar, and PGM and include induced sputum and HBE mucus. These signature behaviors appear to be related to convective constraint release and chain stretching (Teixeira et al., 2007) here by analogy.

The RP model is self-consistent and derived from polymer physics principles. It effectively and accurately models the canonical rheological response of entangled polymer solutions over a large experimental window. The RP model could prove useful in understanding the success or failure of some physiological processes such as mucociliary transport.

Chapter 7

Conclusion

Through the experiments and modeling done here, I present information in this dissertation that directly contributes to the studies of biomaterials and their rheologies at multiple scales. I found the process of shear thinning, a steady state rheological phenomenon, measurable not just with CAP but with the microscale DMBR technique as well, an observation previously unreported in the literature for flexible biopolymers. I was able to recover the macroscopic shear thinning behavior at the microscale by using the maximum shear rate experienced by the fluid because of the probe's velocity. This approach worked for two different probe geometries as seen in Chapter 4 and Chapter 5. Cast into the context of drug delivery, I made first observations regarding a shape preference for rod-shaped magnetic particles over sphere of equal volume, primarily due to the probe's response to the incident magnetic field and secondarily because of the shear thinning occurring at the probe's surface perpendicular to the direction of flow.

Additionally, I discovered the dynamic process of strain thickening in microrheology, unreported in the literature for microrheology techniques. Further, I speculated on how strain thickening might be important in studies of mucociliary interactions which are

integral to our full understanding of functional mucociliary clearance.

Substantial consistency exists between the macroscale and microscale rheology techniques for both steady-state shear thinning and dynamic strain thickening modalities in biopolymer systems. Such consistency reassures that large volumes of purified biomaterial are unnecessary for successful rheological testing. I also provided insight regarding the detection of heterogeneity in the polymer systems studied here in order to address possible inconsistency between measurements due to the wide variability in materials created by biological systems.

To perform these experiments I designed and implemented a process to calibrate variable forces across a sampling field in our magnetic tweezers system, the 3-dimensional force microscope (3DFM). I then used this system to present data for well-characterized Newtonian and homogeneous viscoelastic polymer solutions. My experimental results establish the ability of DMBR as a technique that can measure both linear and non-linear properties of non-Newtonian fluids for the first time.

A future direction of this project lies in the design of a high-throughput thermal and driven microbead system, where the video and tracking systems used here become automated. Such a system will be integral in understanding the breadth of variability in the microrheology of polymer systems across biological origin. This high-throughput system would as well provide the ability to quickly perform dose-response experiments where drug discovery is vital for the treatment of rheological pathologies as in the case of CF or COPD sputum.

Appendix A

Reagent Protocols

A.1 Preparation of Newtonian Fluids

A.1.1 2 M Sucrose Solution

To prepare a 2M sucrose solution, start by quantitatively adding 34.2 g of sucrose (dried at 80°C for 12-16 hours) to a 50 mL volumetric flask. Add approximately 25 mL of distilled water to the flask and heat the resulting solution to approximately 80-90°C. Occasionally agitate the solution to encourage dissolution. Add small amounts of water until the sucrose was fully dissolved. Add sodium azide to the solution (final concentration, 0.05%) to discourage microbial growth. Dilute the solution to volume at room temperature. The viscosity of the solution was predicted by a published model ([Mathlouthi and Reiser, 1995](#)) and confirmed by conventional cone and plate viscometric methods. To compare with model prediction it becomes important to be especially quantitative to reduce systematic error.

A.1.2 2.5 M Sucrose Solution

Follow the same protocol in Section A.1.1 except use 42.8 g of sucrose. Dissolution is substantially more difficult for 2.5 M sucrose and requires additional care when heating and mixing. Before adding additional water to volume, make sure that solution is at room temperature and mix until Schlieren lines dissipate.

A.1.3 Corn Syrup

Purchase corn syrup from a local grocery store and add sodium azide to a final concentration of 0.05-0.1% w/v in order to discourage bacterial growth. Test the syrup for viscosity magnitude as well as shear thinning (which it should not) using a cone and plate rheometer. When adding beads, heat the corn syrup in a hot water bath to 65-70 °C to reduce the syrup's viscosity which ensures successful mixing with a vortexer.

A.2 Bead PEGylation

A.2.1 Materials

- 200 nm, -COOH volume-labeled fluorescent beads
- 25 mM MES Buffer
- 5 mM NHS Buffer
- PEG Solution

- 500 mM TRIS Buffer, pH 7.6
- 15 mM EDAC Solution (cannot premake - decomposes quickly)
- Slow Rotator - use one in fridge if available

A.2.2 Reaction Protocol

1. Prepare 25 mM MES buffer. Add 40 mL water to 3.124 g of MES.
2. Dilute Molecular Probes 200 nm –COOH beads to 1:500 in 25 mM MES buffer.
3. Prepare 5 mM NHS solution. Add 50 μ L MES buffer to 15 mg of NHS.
4. Add 20 μ L of the 5 mM NHS solution to bead dilution and vortex.
5. Prepare 15 mM EDAC solution. Add 100 μ L MES buffer to 15 mg of EDAC.
(Do not prepare EDAC solution until ready to add to reaction.)
6. Immediately add 20 μ L of the 15 mM EDAC solution to the bead/NHS mixture.
7. Vortex and place the beads on the rotator. Allow beads to rotate for 30 minutes.
8. To wash beads with MES buffer, spin beads down in centrifuge (For 200 nm beads, use 18,000 rpm for 10 minutes.) and gently remove supernatant. Add 1 mL MES buffer. Vortex and sonicate to redisperse. Repeat washing procedure (Start by spinning beads down again). Resuspend beads in 1 mL MES buffer.
9. Prepare PEG solution. Add 330 μ L MES buffer to 47.5 mg of Nektar mPEG-NH₂.

10. Add 20 μL of the PEG solution to the reacted beads.
11. Vortex beads and rotate for 2 hours.
12. Wash beads with 500 mM TRIS buffer (pH=7.6). Spin beads down in centrifuge (12,000 rpm for 10 minutes.) Remove supernatant. Add 1 mL TRIS buffer. Vortex and sonicate. Repeat washing procedure 3 times. On last wash, resuspend beads in 300 μL TRIS buffer.

A.3 Distributing Probes into Specimen

1. In a small Eppendorf tube, create an ethanol/bead solution mixture with the desired concentration of beads. Approximately 6 μL of PEG-bead solution works fairly well with a 100 μL sample used in 3DFM pulling experiments. The ethanol:bead solution ratio should be 5:1. That is, if 6 μL of bead solution is used, 30 μL of ethanol should be added. Vortex the ethanol/bead solution mixture lightly.
2. Put a new pipette tip on the pipetter. If the sample is very viscous, snip the pipette tip off with scissors to enable easier pipetting (a few mm off the end should be fine). Using a permanent marker, label the pipette tip with the type of beads you are using for later identification.
3. Set the pipette to about 2 μL more than the amount of the ethanol/bead solution you made. Draw the ethanol/bead solution into the pipette tip. Because you specified more volume than was actually there, there should be a small air bubble

on the bottom.

4. Hold the pipette horizontally with the pipette tip over a clean Kimwipe. CAREFULLY remove the pipette tip and place it horizontally on the Kimwipe. None of the ethanol/bead solution should spill out, but a tiny drop or two is fine. Somewhere on the Kimwipe, clearly mark DO NOT TOUCH.
5. Place the pipette tip on the Kimwipe in the incubator for 20 minutes at 80°C. Do not incubate at a much higher temperature as it may warp the plastic of the pipette tip.
6. While the tip is incubating, remove 100 μL of sample from its stock and place it into a separate Eppendorf tube. This is important to ensure that beads are not accidentally dispersed into the stock.
7. Remove the pipette tip from the incubator. If done correctly, there should appear to be nothing in the pipette tip except for a brown cake-like “ring” around the very edge of the tip (the dried beads).
8. Put the prepared pipette tip on the pipette by hand and adjust the setting on the pipette to slightly more than 100 μL . Pipette the sample that was in the Eppendorf tube back into its own container. This only needs to be done once, but can be done multiple times if the sample is very viscous. There will still be a brown cake-like ring on the edge of the tip, but it should be lighter than before.
9. When analyzing the sample, first try to gather it from the bottom of the new

Eppendorf tube, as this will often be the location of the highest concentration of beads. If the bead population is too low, try gathering the sample from other locations in the Eppendorf tube. The middle of the tube usually has the lowest population of beads, and the edges typically have more.

A.4 Vortex Addition

Vortex addition simply refers to the method used to add a polymer in solid form to a buffer and get fast and efficient dissolution of material, resulting in a homogeneous dispersion. To achieve this, use a 50 mL Falcon tube and use no more than 10 mL of buffer. Weigh out the appropriate amount of polymer material onto a piece of wax paper that has been folded in half at least once and reopened, generating a sharp crease in which to put the polymer material. While the opened Falcon tube is on the vortex mixer, smoothly add the polymer to the sides of the vortex of buffer. If the addition is too slow, the vortex may degrade before all the polymer is added, leaving the remaining polymer on the surface to dissolve slower. If the addition is too fast, the polymer may form large clumps and take extra time to wet and dissolve.

A.5 λ -DNA Polymer System

The goal of this protocol is to construct a homogeneous viscoelastic standard, where the viscoelastic properties arise solely from associations called entanglements between DNA strands.

1. Order λ -DNA. Liquid form (protocol A): As of January 2006, the primary source for our λ -DNA is Invitrogen (www.invitrogen.com, catalog no. 25250). This material is not sold by volume or concentration, but is titrated by mass of λ -DNA. 6 mg of material runs about \$750 US dollars and will make a highly entangled solution with enough volume to do several experiments in the TA AR-G2 cone-and-plate rheometer (0.3 mL per sample). Lyophilized form (protocol B): As of Summer 2008, a lyophilized form of λ -DNA was found from Sigma-Aldrich (www.sigmaaldrich.com, product no. D9768). 10 UN of material runs about \$140, and each unit is about 50 μ g. If you want to make 1 mL of 2 mg/mL material, its going to run about \$560.

2. Order Oligonucleotide. The λ -DNA we use has 12 base pairs on each end that lack complimentary base-pairs. Each end is complementary with its opposite. When the λ -DNA solution is sufficiently concentrated and cooled (as it comes from Invitrogen), the ends are “sticky” and associate with one another and cause circular, star, or random cross-links or topologies between strands. To disrupt this we add high concentrations of one of the oligonucleotide sequences. There are two oligonucleotides one can order (one for each end) from UNC's Oligonucleotide Synthesis Core Facility (<http://www.med.unc.edu/olioli>)

Oligonucleotide #1: 5' - GGG CGG CGA CCT - 3'

Oligonucleotide #2: 5' - AGG TCG CCG CCC - 3'

I have always ordered oligo #1. It is VERY important not to order both ends

and use them in the same solution, as this can result in associations between complementary oligos!

The method used by the Synthesis Core has three scales of production: 40 nmol, 0.2 μmol , and 1 μmol , where these values indicate the number of reaction sites located on the reaction plate. Order the 1 μmol size with HPLC filtration for each oligonucleotide sequence. On the site, the field next to “Oligo A” and “Oligo B” is just a chooseable tag. You list “GGG” down each column to specify the structure of the oligo. The total cost for this should be \$60 per oligonucleotide. Add λ -DNA buffer to resuspend the oligonucleotide, if necessary.

3. Make necessary solutions and buffers.

5M NaCl– To a 50 mL conical centrifuge tube, add 14.61 g of NaCl and dilute to 50 mL. Vortex until dissolved.

400 mM Tris-HCl (pH 7.4)– To a 50 mL conical centrifuge tube, add 2.42 g of Tris-Base and dilute to 40 mL. Vortex to dissolve. The initial pH is about 10.5. Adjust pH to 7.4 using HCl. Typical volume added is \sim 2 mL of 3M HCl. Once pH of 7.4 is attained, dilute to 50 mL.

100 mM EDTA– To a 50 mL conical centrifuge tube, add 1.46 g of EDTA. Dilute to 50 mL. Vortex to dissolve.

Invitrogen λ -DNA Storage Buffer– The buffer Invitrogen uses in their λ -DNA solutions contains 10 mM Tris-HCl (pH 7.4), 5mM NaCl, and 0.1 mM EDTA (Inv, 2007)

The Tris-HCl serves as the pH buffer of which the ionic forms are monovalent. The Na^+ and Cl^- ions of the NaCl are both monovalent and should not contribute to any secondary ordered complexes between two negatively charged chemical species such as a DNA molecule and a negatively charged $-\text{COOH}$ bead. The EDTA is a chelating agent that is deprotonated up to 4 times at high pH. This should effectively bind any divalent ions like Ca^{2+} and minimize their effect on the state of the network.

The pH of the buffer solution is slightly basic, ensuring the deprotonation of the $-\text{COOH}$ groups on the surface of the bead to the $-\text{COO}^-$ ionic form. This sphere of negative charge around the beads helps by keeping them from coagulating.

4. Reconstitute λ -DNA (ONLY if using lyophilized material from Sigma). Add the appropriate amount of Invitrogen storage buffer to each vial. As an example, if there is 500 μg of material in each vial, add 250 μL to each one if the desired concentration is 2 mg/mL. Allow the vial to sit in the refrigerator either overnight or over the weekend to ensure proper reconstitution.
5. Combine λ -DNA vials. Remove λ -DNA solution from each vial via pipetting (maybe not pipetting, shear stress may be a concern here) and mix gently into a 15 mL Falcon tube by vortexing (again, this may be worth looking into for shear stress concerns. You dont want to break λ -DNA strands from too much shear stress. Maybe rocking?). Take out 70 μL of this solution for gel-filtration chromatography and laser scattering technique (aliquot A).

If you are using the lyophilized λ -DNA from Sigma, some of the material will be stuck to the side (particularly if you are making a high concentration) after you pipette the material out. Tie some yarn around one of the vials and spin it around lasso-style for a few minutes, then pipette out again. There is probably a better way to do this, but this works for now, as none of the centrifuges we have currently fit the sigma vials.

****IMPORTANT**** Whenever transferring this material, it is very important to ensure that all of the material that could be stuck to the sides has been gathered. First just pipette the material normally, then spin it down in the big centrifuge in 161 (lowest setting ≥ 2 minutes works fine), then pipette again. You should see some material “magically” appear at the bottom of the Falcon tube. It is usually a fairly substantial amount $50 \mu\text{L}$ or so. Make sure you pipette this as well to ensure the highest possible volume transfer and consistency in concentration.

6. Determine solution logistics via Spreadsheet. The current spreadsheet location is [//nsrg/nanodata/cribb/doc/rheology/DNA](https://nsrg.nanodata/cribb/doc/rheology/DNA). Remember to modify only the values that are in yellow.
7. Cap λ -DNA. The idea here is to heat λ -DNA between 65 and 90 °C for 15 minutes. Boil water and add to Styrofoam container (cooler). This will “melt” the λ -DNA and break up strand-strand interactions. Add the appropriate volume of oligonucleotides to λ -DNA solution. Set the solution in a Styrofoam container and allow it to cool slowly over 16 hours or overnight. Take out $70 \mu\text{L}$ of this

solution for gel-filtration chromatography and laser scattering technique (aliquot B).

8. Determine concentration of λ -DNA via UV/Vis. The λ -DNA vials that come from Invitrogen each contain 500 μg of λ -DNA in approximately 1 mL (Inv, 2007). The specific extinction of λ -DNA is $0.02 \text{ mL } \mu\text{g}^{-1}\text{cm}^{-1}$ at a wavelength of 260 nm. The UV/Vis Spectrometer is a Cary 400-Bio, with a 1 cm cell path. Beer's Law states that $A = \epsilon bc$, where A is the absorbance read by the instrument, ϵ is the specific extinction, b is the distance the light travels through the material (cell length), and c is the concentration of the material. Put 5 μL of the sample into a cuvette and dilute to 1 mL with λ -DNA buffer. This results in a dilution factor of $1000/5 = 200$. If all of the above protocol is followed, the concentration of the material can be measured by simply taking the absorbance number on screen and multiplying it by ten. ****Important**** Use UV-Clear cuvettes when taking these measurements.
9. Concentrate and Purify Capped λ -DNA Strands. This step is only necessary if the measured concentration is lower than the desired concentration. Currently, there are two methods to do this. Alcoholic precipitation is much more unpredictable and takes longer thus, it is not the currently preferred method. It certainly has benefits, however, if a large enough volume has to be concentrated. It has been included for completeness, but the microcentrifuge method is highly preferred when possible.

10. Check Concentration by UV/Vis. This λ -DNA solution should have about 2 times more λ -DNA per unit volume than the stock Invitrogen solution. Use 5 μL of λ -DNA solution in 495 μL of λ -DNA storage buffer and check concentration using method in Step 8. Take out 70 μL of this solution for gel-filtration chromatography and laser scattering technique (aliquot C).
11. Adjust Concentration and confirm by UV/Vis. If the resulting concentration from step 10 is too high, simply dilute the solution back down to the desired concentration with the λ -DNA buffer. This should be confirmed (again) by UV-Vis (method in Step 8).
12. Compute yield/recovery. This can be done in the same spreadsheet from Step 6.
13. Confirm Capping Procedure via Fluorescence Microscopy. Dilute the stock λ -DNA solution to a concentration of $0.01c^*$ ($c^* = 0.04 \text{ mg/mL}$) and look for homogeneous spot size (do this by eye or matlab has routine that can do this easily).
14. Add oligonucleotide at $1000\times$ stoichiometric requirements.
15. Heat mixture to 65°C to break up strand-strand associations.
16. Concentrate by appropriate method (alcoholic precipitation or microcon filtration).
17. Check concentration by spectrophotometric methods at 260 nm.
18. Confirm by fluorescence at $1/100 c^*$ by imaging for homogeneous spot size.

A.6 Concentrating λ -DNA

A.6.1 Microcentrifugation

Order Microcon YM-100 centrifugal concentrators from Fisher (www.fishersci.com, catalog no. Millipore 42412). These are mesh filters that have a nominal molecular weight limit (NMWL) of 100,000 Daltons that have been specially designed for use in any centrifugal device compatible with Eppendorf tubes. Each filter membrane has a maximum of three uses before physical failure.

- Insert the sample reservoir (blue part) into the vial, with the larger, non-ridged side on top.
- Pipette the solution into the sample reservoir (0.5 mL maximum volume for each reservoir, so multiple assemblies might need to be made depending on initial volume of solution) without touching the membrane with the pipette tip.
- Seal with attached cap.
- Place the assembly into the centrifuge, making sure to counterbalance, and spin at $500 \times g$ for 12 minutes.
- Take the sample reservoir out of the vial and place it upside down in a new clean vial, then spin for 6 minutes at $500 \times g$ to transfer the concentrate for a new vial. This process can be repeated multiple times to ensure higher concentrations, but keep in mind that each membrane can only be used three times before failure.

- Take the concentrate from each new vial and combine into one large vial when finished.
- Each membrane has a “dead volume” of 10 μL , which means that 10 μL of solution will be lost for each filter that is used. This is typically negligible, but the lowest possible number of filters should be used each time.
- As a point of reference, it took two spin cycles to concentrate from 1.2 mg/mL to 1.8 mg/mL. At lower concentrations, the microcentrifuge process will typically concentrate more effectively.
- The final concentration can be adequately estimated via the volume of solvent removed, but should be checked via UV-Vis (see step 6 and 10).

A.6.2 Alcoholic Precipitation

λ -DNA can be concentrated/purified by precipitation in the presence of ethanol (60% – 80% final volume) or isopropanol (30% – 50% final volume) and salt (LiCl, NaCl, NaOAc, or NH₄Ac is commonly used) , and cold environmental conditions (-20 C) and pelleted by high-speed (13,000 $\times g$) centrifugation. When alcoholic precipitation is used to concentrate λ -DNA strands, the free oligomers should not precipitate or spin out during centrifugation.

- Place 0.4 mL of capped λ -DNA into the appropriate number of 1.5 mL centrifuge tubes.

- Add 50 μL of 5 M NaCl solution to each tube.
- Vortex lightly, pulsing for no more than 1 second at a time.
- Add 800 μL of cold ethanol (EtOH) to each tube. Leave the EtOH in the freezer until needed.
- Vortex lightly, pulsing for no more than 1 second at a time.
- Place tubes at -20°C (standard consumer-grade freezer temperature) for 30 min.
- Confirm visually that precipitation has occurred. If not, then leave in freezer for another 30 min.
- Centrifuge for 10 minutes at $13,000 \times g$.
- Place tubes at -20°C (standard consumer-grade freezer temperature) for 5 min.
- Centrifuge for 5 minutes at $13,000 \times g$.
- Typically the pellet is stuck to the side of the tube and will not dislodge when you pour out the supernatant. Save the supernatant. If you don't want to risk it, you can aspirate the supernatant. Dry pellets are not required pre-rinse.
- Rinse: Add 80 μL of storage buffer and 800 μL of cold EtOH to each tube.
- Centrifuge for 2–3 minutes at $13,000 \times g$.
- Aspirate or pour out the supernatant. Allow the pellet to dry by leaving the tubes suspended upside-down for 5–10 min. Use a swab to remove excess liquid in the upper portion of the Eppendorf tube.

- You may want to segregate vials with large pellets from those with little to no pellet.
- Add appropriate volume of storage buffer such that the final collective volume is 2 mL. This will allow for sufficient volume to do cone-and-plate at the highest possible λ -DNA concentration.
- Leave the vials in the refrigerator overnight. The next day, vortex lightly, pulsing for no more than 1 second at a time. Centrifuge for 30 seconds at $5000 \times g$.
- Combine all vials that are equivalent (i.e. if you separated into “big pellet” vs. “little pellet”, then combine all big pellet vials separately from all little pellet vials).
- Rotate on slow rotator at room temperature for 30 minutes to ensure maximum hydration and strand intercolation and polymer homogeneity.

Appendix B

Optimized Sequences for Variable Force Calibration

Pole-tip saturation for Netic material

This is the most complete calibration protocol that creates force data across the entire range of available voltages.

Fluid	2.5M sucrose
Voltages [V]	[0.0 0.5 0.75 1.0 1.25 1.5 1.75 2.0 2.5 3.0 3.5 4.0 4.5 5.0]
Pulse Widths [s]	[0.2 0.2 0.1 0.1 0.1 0.1 0.1 0.1 0.1 0.1 0.1 0.1 0.1 0.1]

Fluid	2.5M sucrose
Voltages [V]	[0 0.1 0.2 0.4 0.5 0.6 0.8 1 1.2]
Pulse Widths [s]	[.624 0.416 0.416 0.208 0.208 0.208 0.104 0.104 0.104]

Pole-tip saturation for Co-Netic material

Bead saturation for Netic material (low-voltage calibration)

This method demonstrates bead saturation for 1 μm MyOne beads. More generally, this method provides precise data for calibrations at low force.

Fluid	2.0M sucrose
Voltages [V]	[0.0 0.05 0.1 0.15 0.2 0.25 0.3 0.35 0.4 0.45 0.5 0.55 0.6]
Pulse Widths [s]	[0.3 0.4 0.4 0.4 0.3 0.2 0.2 0.1 0.1 0.1 0.1 0.1 0.1]

Measuring remanence in Pole tips (force ratio)

Fluid	2.5M sucrose
Voltages [V]	[5.0 0.0]
Pulse Widths [s]	[0.2 0.5]

Fluid	Karo (3.4 Pa s)
Voltages [V]	[5.0 0.0]
Pulse Widths [s]	[0.1 0.2]

Measuring maximum force on 1 μm or 2.8 μm beads

Measuring viscosity of 2 M or 2.5 M sucrose

Fluid	Karo (3.4 Pa s)
Voltages [V]	[0.6 0.0]
Pulse Widths [s]	[0.2 0.3]

Bibliography

- (2007). Invitrogen lambda-dna product insert.
- Amblard, F., Maggs, A. C., Yurke, B., Pargellis, A. N., and Leibler, S. (1996a). Subdiffusion and anomalous local viscoelasticity in actin networks. *Physical Review Letters*, 77(21):4470–4473.
- Amblard, F., Yurke, B., Pargellis, A., and Leibler, S. (1996b). A magnetic manipulator for studying local rheology and micromechanical properties of biological systems. *Review of Scientific Instruments*, 67(3):818–827.
- Apgar, J., Tseng, Y., Fedorov, E., Herwig, M. B., Almo, S. C., and Wirtz, D. (2000). Multiple-particle tracking measurements of heterogeneities in solutions of actin filaments and actin bundles. *Biophysical Journal*, 79(2):1095–1106.
- Ashkin, A. and Dziedzic, J. (1987). Optical trapping and manipulation of viruses and bacteria. *Science*, 235(4795):1517–1520.
- Balazs, E. and Gibbs, D. (1970). The rheological properties and biological function of hyaluronic acid. *Chemistry and molecular biology of the intercellular matrix*, 3:1241–1253.
- Bausch, A. R., Moller, W., and Sackmann, E. (1999). Measurement of local viscoelasticity and forces in living cells by magnetic tweezers. *Biophysical Journal*, 76(1):573–579.
- Bausch, A. R., Ziemann, F., Boulbitch, A. A., Jacobson, K., and Sackmann, E. (1998). Local measurements of viscoelastic parameters of adherent cell surfaces by magnetic bead microrheometry. *Biophysical Journal*, 75(4):2038–2049.
- Berg, H. C. (1993). *Random Walks in Biology*. Princeton University Press, Princeton, NJ.
- Berry, C. C. and Curtis, A. S. G. (2003). Functionalisation of magnetic nanoparticles for applications in biomedicine. *Journal of Physics D-Applied Physics*, 36(13):R198–R206.
- Besseris, G. J. and Yeates, D. B. (2007). Rotating magnetic particle microrheometry in biopolymer fluid dynamics: Mucus microrheology. *Journal of Chemical Physics*, 127(10).
- Block, S., Goldstein, L., and Schnapp, B. (1990). Bead movement by single kinesin molecules studied with optical tweezers.

- Braun, E., Eichen, Y., Sivan, U., and Ben-Yoseph, G. (1998). Dna-templated assembly and electrode attachment of a conducting silver wire. *Nature*, 391(6669):775–778.
- Brown, R. (1828). On the existence of active molecules in organic and inorganic bodies. *Phil. Mag*, 4:162–173.
- Buhler, E. and Boue, F. (2004). Chain persistence length and structure in hyaluronan solutions: ionic strength dependence for a model semirigid polyelectrolyte. *Macromolecules*, 37(4):1600–1610.
- Celli, J., Turner, B., Afdhal, N., Ewoldt, R., McKinley, G., Bansil, R., and Erramilli, S. (2007). Rheology of Gastric Mucin Exhibits a pH-Dependent Sol-Gel Transition. *Biomacromolecules*, 8(5):1580–1586.
- Chen, T. M. and Dulfano, M. J. (1978). Mucus viscoelasticity and mucociliary transport rate. *J Lab Clin Med*, 91(3):423–31.
- Ciureanu, M., Beron, F., Clime, L., Ciureanu, P., Yelon, A., Ovari, T. A., Cochrane, R. W., Normandin, F., and Veres, T. (2005). Magnetic properties of electrodeposited cofeb thin films and nanowire arrays. *Electrochimica Acta*, 50(22):4487–4497.
- Colby, R., Boris, D., Krause, W., and Dou, S. (2007). Shear thinning of unentangled flexible polymer liquids. *Rheologica Acta*, 46(5):569–575.
- Creuwels, L., Van Golde, L., and Haagsman, H. (1997). The pulmonary surfactant system: biochemical and clinical aspects. *Lung*, 175(1):1–39.
- Crick, F. and Hughes, A. (1949). The physical properties of cytoplasm: a study by means of the magnetic particle method. *Exp. Cell Res*, 1:37–80.
- Crocker, J. C., Valentine, M. T., Weeks, E. R., Gisler, T., Kaplan, P. D., Yodh, A. G., and Weitz, D. A. (2000). Two-point microrheology of inhomogeneous soft materials. *Physical Review Letters*, 85(4):888–891.
- Dassios, G., Hadjinicolaou, M., Coutelieris, F., and Payatakes, A. (1995). Stokes flow in spheroidal particle-in-cell models with Happel and Kuwabara boundary conditions. *International Journal of Engineering Science*, 33(10):1465–1490.
- de Morales, M. P., Grabulosa, M., Alcaraz, J., Mullol, J., Maksym, G. N., Fredberg, J. J., and Navajas, D. (2001). Measurement of cell microrheology by magnetic twisting cytometry with frequency domain demodulation. *Journal of Applied Physiology*, 91(3):1152–1159.
- Desseyn, J., Aubert, J., Porchet, N., and Laine, A. (2000). Evolution of the large secreted gel-forming mucins. *Molecular Biology and Evolution*, 17(8):1175.

- Dobrynin, A. V. and Rubinstein, M. (2005). Theory of polyelectrolytes in solutions and at surfaces. *Progress in Polymer Science*, 30(11):1049–1118.
- Dobson, J. (2006). Gene therapy progress and prospects: magnetic nanoparticle-based gene delivery. *Gene Therapy*, 13(4):283–287.
- Einstein, A. (1905). Motion of suspended particles on the kinetic theory. *Annalen der Physik*, 17(3):549–560.
- Eliezer, N., Sade, J., Silberberg, A., and Nevo, A. C. (1970). The role of mucus in transport by cilia. *Am Rev Respir Dis*, 102(1):48–52.
- Encinas-Oropesa, A., Demand, M., Piraux, L., Ebels, U., and Huynen, I. (2001). Effect of dipolar interactions on the ferromagnetic resonance properties in arrays of magnetic nanowires. *Journal of Applied Physics*, 89(11):6704–6706.
- Feneberg, W., Aepfelbacher, M., and Sackmann, E. (2004). Microviscoelasticity of the apical cell surface of human umbilical vein endothelial cells (huvec) within confluent monolayers. *Biophysical Journal*, 87(2):1338–1350.
- Ferry, J. (1980). *Viscoelastic Properties of Polymers (3rd)*. New York.
- Fisher, J., Cummings, J., Desai, K., Vicci, L., Wilde, B., Keller, K., Weigle, C., Bishop, G., Taylor, R., Davis, C., et al. (2005). Three-dimensional force microscope: a nanometric optical tracking and magnetic manipulation system for the biomedical sciences. *Review of Scientific Instruments*, 76:053711.
- Fisher, J. K. (2007). *Development of a Magnetic Manipulator for Microbiological and Single Molecule Investigations*. PhD thesis, University of North Carolina at Chapel Hill.
- Fisher, J. K., Cribb, J., Desai, K. V., Vicci, L., Wilde, B., Keller, K., Taylor, R. M., Haase, J., Bloom, K., O’Brien, E. T., and Superfine, R. (2006a). Thin-foil magnetic force system for high-numerical-aperture microscopy. *Review of Scientific Instruments*, 77(2):–.
- Fisher, J. K., Vicci, L., Cribb, J., O’Brien, E. T., Taylor, R. M., and Superfine, R. (2006b). Magnetic force micromanipulation systems for the biological sciences. *Nano*, 1(3):191–205.
- Florin, E. L., Pralle, A., Stelzer, E. H. K., and Horber, J. K. H. (1998). Photonic force microscope calibration by thermal noise analysis. *Applied Physics a-Materials Science & Processing*, 66:S75–S78.
- Gardel, M., Valentine, M., and Weitz, D. (2005). Microrheology. *Microscale Diagnostic Techniques*. Heidelberg, Springer-Verlag Berlin Heidelberg, 2005, pages 1–49.

- Gardel, M. L., Crocker, J. C., Valentine, M. T., Bausch, A. R., and Weitz, D. A. (2003). One- and two-particle microrheology of f-actin. *Biophysical Journal*, 84(2):437a–437a.
- Gijs, M. (2004). Magnetic bead handling on-chip: new opportunities for analytical applications. *Microfluidics and Nanofluidics*, 1(1):22–40.
- Gittes, F. and MacKintosh, F. C. (1998). Dynamic shear modulus of a semiflexible polymer network. *Physical Review E*, 58(2):R1241–R1244.
- Gittes, F., Schnurr, B., Olmsted, P. D., MacKintosh, F. C., and Schmidt, C. F. (1997). Microscopic viscoelasticity: Shear moduli of soft materials determined from thermal fluctuations. *Physical Review Letters*, 79(17):3286–3289.
- Gittings, M., Cipelletti, L., Trappe, V., Weitz, D., In, M., and Marques1a, C. (2000). Structure of Guar in Solutions of H₂O and D₂O: An Ultra-Small-Angle Light-Scattering Study. *J. Phys. Chem. B*, 104(18):4381–4386.
- Goya, G. F., Grazu, V., and Ibarra, M. R. (2008). Magnetic nanoparticles for cancer therapy. *Current Nanoscience*, 4(1):1–16.
- Greenberg, M. (1998). *Advanced Engineering Mathematics*. Prentice-Hall, Englewood Cliffs, NJ.
- Groneberg, D., Witt, C., Wagner, U., Chung, K., and Fischer, A. (2003). Fundamentals of pulmonary drug delivery. *Respiratory medicine*, 97(4):382–387.
- Guthold, M., Liu, W., Sparks, E., Jawerth, L., Peng, L., Falvo, M., Superfine, R., Hantgan, R., and Lord, S. (2007). A comparison of the mechanical and structural properties of fibrin fibers with other protein fibers. *Cell Biochemistry and Biophysics*, 49(3):165–181.
- Hackley, V. and Ferraris, C. (2001). Guide to rheological nomenclature: measurements in ceramic particulate systems. *NIST Special Publication(USA)*, 946:31.
- Happel, J. and Brenner, H. (1991). *Low Reynolds number hydrodynamics: with special applications to particulate media*. Kluwer Academic Print on Demand.
- Hardingham, T. (2004). Solution properties of hyaluronan. *Chemistry and Biology of Hyalurona*, pages 1–19.
- Heo, Y. and Larson, R. G. (2005). The scaling of zero-shear viscosities of semidilute polymer solutions with concentration. *Journal of Rheology*, 49(5):1117–1128.
- Hill, D., Swaminathan, V., Estes, A., Cribb, J., O’Brien, E., Davis, C., and Superfine, R. (2010). Force Generation and Dynamics of Individual Cilia under External Loading. *Biophysical Journal*, 98(1):57–66.

- Hirakawa, E., Higuchi, H., and Toyoshima, Y. (2000). Processive movement of single 22S dynein molecules occurs only at low ATP concentrations.
- Holma, B. (1967). Lung clearance of mono- and di-disperse aerosols determined by profile scanning and whole-body counting. A study on normal and SO₂ exposed rabbits. *Acta medica Scandinavica. Supplementum*, 473:1.
- Howard, J. (2001). *Mechanics of Motor Proteins and the Cytoskeleton*. Sinauer, Sunderland, MA.
- Hubbard, R., Crystal, R., Crystal, R., West &, J., Barnes, P., Cherniack, N., and Weibel, E. (1991). The Lung Scientific Foundations.
- Hultgren, A., Tanase, M., Chen, C. S., Meyer, G. J., and Reich, D. H. (2003). Cell manipulation using magnetic nanowires. *Journal of Applied Physics*, 93(10):7554–7556.
- Hur, J. S., Shaqfeh, E. S. G., Babcock, H. P., Smith, D. E., and Chu, S. (2001). Dynamics of dilute and semidilute dna solutions in the start-up of shear flow. *Journal of Rheology*, 45(2):421–450.
- Hyun, K., Kim, S. H., Ahn, K. H., and Lee, S. J. (2002). Large amplitude oscillatory shear as a way to classify the complex fluids. *Journal of Non-Newtonian Fluid Mechanics*, 107(1-3):51–65.
- Imeson, A. (1999). *Thickening and gelling agents for food*. Aspen Publishers.
- Jain, K. K. (2003). Nanodiagnostics: application of nanotechnology in molecular diagnostics. *Expert Review of Molecular Diagnostics*, 3(2):153–161.
- Jay, G. D., Torres, J. R., Warman, M. L., Laderer, M. C., and Breuer, K. S. (2007). The role of lubricin in the mechanical behavior of synovial fluid. *Proc Natl Acad Sci U S A*, 104(15):6194–9.
- Kesimer, M., Kirkham, S., Pickles, R., Henderson, A., Alexis, N., DeMaria, G., Knight, D., Thornton, D., and Sheehan, J. (2009). Tracheobronchial air-liquid interface cell culture: a model for innate mucosal defense of the upper airways? *American Journal of Physiology- Lung Cellular and Molecular Physiology*, 296(1):L92.
- King, M. and Macklem, P. T. (1977). Rheological properties of microliter quantities of normal mucus. *J Appl Physiol*, 42(6):797–802.
- Kishino, A. and Yanagida, T. (1988). Force measurements by micromanipulation of a single actin filament by glass needles.
- Kocevar-Nared, J., Kristl, J., and Smid-Korbar, J. (1997). Comparative rheological investigation of crude gastric mucin and natural gastric mucus. *Biomaterials*, 18(9):677–81.

- Kong, Q. and Vazquez, M. (2008). Flow-induced shear stresses increase the number of cell-cell contacts within extracellular matrix. *Journal of biomedical materials research. Part A*.
- Krause, W. E., Bellomo, E. G., and Colby, R. H. (2001). Rheology of sodium hyaluronate under physiological conditions. *Biomacromolecules*, 2(1):65–69.
- Kuhn, S. J., Finch, S. K., Hallahan, D. E., and Giorgio, T. D. (2006a). Proteolytic surface functionalization enhances in vitro magnetic nanoparticle mobility through extracellular matrix. *Nano Lett*, 6(2):306–12.
- Kuhn, S. J., Hallahan, D. E., and Giorgio, T. D. (2006b). Characterization of superparamagnetic nanoparticle interactions with extracellular matrix in an in vitro system. *Ann Biomed Eng*, 34(1):51–8.
- Kuo, S. and Sheetz, M. (1993). Force of single kinesin molecules measured with optical tweezers. *Science*, 260(5105):232–234.
- Lai, G. L., Li, Y., and Li, G. Y. (2008). Effect of concentration and temperature on the rheological behavior of collagen solution. *International Journal of Biological Macromolecules*, 42(3):285–291.
- Lai, S. K., O’Hanlon, D. E., Harrold, S., Man, S. T., Wang, Y. Y., Cone, R., and Hanes, J. (2007). Rapid transport of large polymeric nanoparticles in fresh undiluted human mucus. *Proceedings of the National Academy of Sciences of the United States of America*, 104(5):1482–1487.
- Lehmann, U., Hadjidj, S., Parashar, V. K., Vandevyver, C., Rida, A., and Gijs, M. A. M. (2006). Two-dimensional magnetic manipulation of microdroplets on a chip as a platform for bioanalytical applications. *Sensors and Actuators B-Chemical*, 117(2):457–463.
- Li, C. Z. and Lodder, J. C. (1990). The influence of the packing density on the magnetic-behavior of alumite media. *Journal of Magnetism and Magnetic Materials*, 88(1-2):236–246.
- Likhtman, A. and Graham, R. (2003). Simple constitutive equation for linear polymer melts derived from molecular theory: Rolie–Poly equation. *Journal of Non-Newtonian Fluid Mechanics*, 114(1):1–12.
- Macosko, C. and Larson, R. (1994). *Rheology: principles, measurements, and applications*. Vch New York.
- Mao, H., Arias-Gonzalez, J., Smith, S., Tinoco, I., and Bustamante, C. (2005). Temperature control methods in a laser tweezers system. *Biophysical journal*, 89(2):1308–1316.

- Maret, G. and Wolf, P. (1987). Multiple light scattering from disordered media. The effect of Brownian motion of scatterers. *Zeitschrift für Physik B Condensed Matter*, 65(4):409–413.
- Mason, T. G. (2000). Estimating the viscoelastic moduli of complex fluids using the generalized stokes-einstein equation. *Rheologica Acta*, 39(4):371–378.
- Mason, T. G., Dhople, A., and Wirtz, D. (1998). Linear viscoelastic moduli of concentrated dna solutions. *Macromolecules*, 31(11):3600–3603.
- Mason, T. G., Ganesan, K., vanZanten, J. H., Wirtz, D., and Kuo, S. C. (1997). Particle tracking microrheology of complex fluids. *Physical Review Letters*, 79(17):3282–3285.
- Mason, T. G. and Weitz, D. A. (1995). Optical measurements of frequency-dependent linear viscoelastic moduli of complex fluids. *Physical Review Letters*, 74(7):1250–1253.
- Mathlouthi, M. and Reiser, P. (1995). *Sucrose: Properties and Applications*. Springer.
- Matsui, H., Wagner, V. E., Hill, D. B., Schwab, U. E., Rogers, T. D., Button, B., Taylor, R. M., Superfine, R., Rubinstein, M., Iglewski, B. H., and Boucher, R. C. (2006). A physical linkage between cystic fibrosis airway surface dehydration and pseudomonas aeruginosa biofilms. *Proceedings of the National Academy of Sciences of the United States of America*, 103(48):18131–18136.
- Meehan, T. (2007). *Quantitative Magnetophoresis of Micro and Nano Particles*. PhD thesis, University of North Carolina at Chapel Hill.
- Meyer, A., Marshall, A., Bush, B. G., and Furst, E. M. (2006). Laser tweezer microrheology of a colloidal suspension. *Journal of Rheology*, 50(1):77–92.
- Morris, G., Patel, T., Picout, D., Ross-Murphy, S., Ortega, A., Garcia de la Torre, J., and Harding, S. (2008). Global hydrodynamic analysis of the molecular flexibility of galactomannans. *Carbohydrate Polymers*, 72(2):356–360.
- Morrison, F. (2001). *Understanding rheology*. Oxford University Press, USA.
- Niensch, K., Muller, F., Li, A. P., and Gosele, U. (2000). Uniform nickel deposition into ordered alumina pores by pulsed electrodeposition. *Advanced Materials*, 12(8):582–586.
- O’Brien, E. T., Cribb, J., Marshburn, D., II, R. M. T., and Superfine, R. (2008). Chapter 16 magnetic manipulation for force measurements in cell biology. In Correia, D. J. J. and Dr. H. William Detrich, I., editors, *Biophysical Tools for Biologists, Volume Two: In Vivo Techniques*, volume 89 of *Methods in Cell Biology*, pages 433–450. Academic Press.

- Okada, H. and Toguchi, H. (1995). Biodegradable microspheres in drug-delivery. *Critical Reviews in Therapeutic Drug Carrier Systems*, 12(1):1–99.
- Osborn, J. A. (1945). Demagnetizing factors of the general ellipsoid. *Physical Review*, 67(11-12):351–357.
- Parkin, S., Knoner, G., Nieminen, T., Heckenberg, N., and Rubinsztein-Dunlop, H. (2006). Optical microrheology of biopolymers. In *Proc. SPIE*, volume 6038, pages 55–61.
- Perez-Vilar, J. and Hill, R. (1999). The structure and assembly of secreted mucins.
- Peterman, E., Gittes, F., and Schmidt, C. (2003). Laser-induced heating in optical traps. *Biophysical journal*, 84(2):1308–1316.
- Petkowicz, C., Reicher, F., and Mazeau, K. (1998). Conformational analysis of galactomannans: from oligomeric segments to polymeric chains. *Carbohydrate Polymers*, 37(1):25–39.
- Picout, D., Ross-Murphy, S., Errington, N., and Harding, S. (2001). Pressure cell assisted solution characterization of polysaccharides. 1. Guar gum. *Biomacromolecules*, 2(4):1301–1309.
- Pine, D. J., Weitz, D. A., Chaikin, P. M., and Herbolzheimer, E. (1988). Diffusing wave spectroscopy. *Phys. Rev. Lett.*, 60(12):1134–1137.
- Powell, R. L., Aharonson, E. F., Schwarz, W. H., Proctor, D. F., Adams, G. K., and Reasor, M. (1974). Rheological behavior of normal tracheobronchial mucus of canines. *J Appl Physiol*, 37(3):447–51.
- Puchelle, E., Polu, J. M., Zahm, J. M., and Sadoul, P. (1980a). Role of the rheological properties of bronchial secretions in the mucociliary transport at the bronchial surface. *Eur J Respir Dis Suppl*, 111:29–34.
- Puchelle, E., Zahm, J. M., Girard, F., Bertrand, A., Polu, J. M., Aug, F., and Sadoul, P. (1980b). Mucociliary transport in vivo and in vitro. relations to sputum properties in chronic bronchitis. *Eur J Respir Dis*, 61(5):254–64.
- Purcell, E. M. (1977). Life at low reynolds number.
- Quemada, D. (1998). Rheological modelling of complex fluids. *Eur. Phys. J. AP*, 1:119–127.
- Round, A. N., Berry, M., McMaster, T. J., Stoll, S., Gowers, D., Corfield, A. P., and Miles, M. J. (2002). Heterogeneity and persistence length in human ocular mucins. *Biophysical Journal*, 83(3):1661–1670.

- Rubin, B. K. (2006). The pharmacologic approach to airway clearance: Mucoactive agents. *Paediatric Respiratory Reviews*, 7(Supplement 1):S215–S219.
- Rubinstein, M. and Colby, R. H. (2003). *Polymer Physics*. Oxford University Press, Oxford, UK.
- Safarik, I. and Safarikova, M. (2002). Magnetic nanoparticles and biosciences. *Monatshefte Fur Chemie*, 133(6):737–759.
- Sahu, S., Tanswell, A., and Lynn, W. (1980). Isolation and characterization of glycosaminoglycans secreted by human foetal lung type II pneumocytes in culture.
- Saxton, M. J. and Jacobson, K. (1997). Single-particle tracking: applications to membrane dynamics. *Annual Review of Biophysics and Biomolecular Structure*, 26(1):373–399.
- Schmidt, F. G., Hinner, B., and Sackmann, E. (2000). Microrheometry underestimates the values of the viscoelastic moduli in measurements on f-actin solutions compared to macrorheometry. *Physical Review E*, 61(5):5646–5653.
- Schmitz, K., Holcomb-Wygle, D., Oberski, D., and Lindemann, C. (2000). Measurement of the force produced by an intact bull sperm flagellum in isometric arrest and estimation of the dynein stall force. *Biophysical Journal*, 79(1):468–478.
- Schneider, W. and Doetsch, R. (1974). Effect of viscosity on bacterial motility. *Journal of Bacteriology*, 117(2):696.
- Schnurr, B., Gittes, F., MacKintosh, F. C., and Schmidt, C. F. (1997). Determining microscopic viscoelasticity in flexible and semiflexible polymer networks from thermal fluctuations.
- Schubert, R. (2009). The video spot tracker (working title). (*in preparation*).
- Seddon, D. and Snashall, P. (1989). Measurement of lung tissue mass in Pneumocystis carinii pneumonia. *British Medical Journal*, 44(8):640.
- Shih, C. K., Litt, M., Khan, M. A., and Wolf, D. P. (1977). Effect of nondialyzable solids concentration and viscoelasticity on ciliary transport of tracheal mucus. *Am Rev Respir Dis*, 115(6):989–95.
- Silbert, L. E., Melrose, J. R., and Ball, R. C. (1999). The rheology and microstructure of concentrated, aggregated colloids. *Journal of Rheology*, 43(3):673–700.
- Skibbens, R. and Salmon, E. (1997). Micromanipulation of chromosomes in mitotic vertebrate tissue cells: tension controls the state of kinetochore movement. *Experimental cell research*, 235(2):314–324.

- Spero, R. C., Vicci, L., Cribb, J., Bober, D., Swaminathan, V., O'Brien, E. T., Rogers, S. L., and Superfine, R. (2008). High throughput system for magnetic manipulation of cells, polymers, and biomaterials. *Rev Sci Instrum*, 79(8):083707.
- Squires, T. (2008). Nonlinear Microrheology: Bulk Stresses versus Direct Interactions. *Langmuir*, 24(4):1147–1159.
- Stachel, J. and Raman, V. (1990). The Collected Papers of Albert Einstein. Vol. 2. The Swiss Years: Writings, 1900- 1909. *American Journal of Physics*, 58:700.
- Tartaj, P., Morales, M. D., Veintemillas-Verdaguer, S., Gonzalez-Carreno, T., and Serna, C. J. (2003). The preparation of magnetic nanoparticles for applications in biomedicine. *Journal of Physics D-Applied Physics*, 36(13):R182–R197.
- Teixeira, R., Dambal, A., Richter, D., Shaqfeh, E., and Chu, S. (2007). The individualistic dynamics of entangled DNA in solution. *Macromolecules*, 40(7):2461–2476.
- Ter-Oganessian, N., Pink, D. A., and Boulbitch, A. (2005). Active microrheology of networks composed of semiflexible polymers: Theory and comparison with simulations. *Physical Review E*, 72(4):–.
- Tirado, M. M. and de la Torre, J. G. (1979). Translational friction coefficients of rigid, symmetric top macromolecules. application to circular cylinders.
- Uhde, J., Feneberg, W., Ter-Oganessian, N., Sackmann, E., and Boulbitch, A. (2005a). Osmotic force-controlled microrheometry of entangled actin networks. *Physical Review Letters*, 94(19):–.
- Uhde, J., Ter-Oganessian, N., Pink, D. A., Sackmann, E., and Boulbitch, A. (2005b). Viscoelasticity of entangled actin networks studied by long-pulse magnetic bead microrheometry. *Physical Review E*, 72(6):–.
- Vicci, L. (2005). The 3dfm magnet drive amplifier. Technical report, University of North Carolina at Chapel Hill.
- Waigh, T. A. (2005). Microrheology of complex fluids. *Reports on Progress in Physics*, 68(3):685–742.
- Watson, J. D. and Crick, F. H. (1953). Molecular structure of nucleic acids; a structure for deoxyribose nucleic acid. *Nature*, 171(4356):737–8.
- Wilking, J. and Mason, T. (2008). Optically driven nonlinear microrheology of gelatin. *Physical Review E*, 77(5):55101.
- Woo, N. J., Shaqfeh, E. S. G., and Khomami, B. (2004). Effect of confinement on dynamics and rheology of dilute dna solutions. i. entropic spring force under confinement and a numerical algorithm. *Journal of Rheology*, 48(2):281–298.

- Wust, P., Hildebrandt, B., Sreenivasa, G., Rau, B., Gellermann, J., Riess, H., Felix, R., and Schlag, P. M. (2002). Hyperthermia in combined treatment of cancer. *Lancet Oncology*, 3(8):487–497.
- Yager, J., Chen, T., and Dulfano, M. (1978). Measurement of frequency of ciliary beats of human respiratory epithelium. *Chest*, 73(5):627.
- Yeates, D., Besseris, G., and Wong, L. (1997). Physicochemical properties of mucus and its propulsion. *The lung: scientific foundations. 2nd edition. RG Crystal, JB West, ER Weibel, and PJ Barnes, editors. Lippincott-Raven Publishers. Philadelphia, PA*, pages 487–503.
- Yin, H., Wang, M., Svoboda, K., Landick, R., Block, S., and Gelles, J. (1995). Transcription against an applied force. *Science*, 270(5242):1653.
- Zhu, X., Kundukad, B., and van der Maarel, J. R. (2008). Viscoelasticity of entangled lambda-phage dna solutions. *J Chem Phys*, 129(18):185103.
- Ziemann, F., Radler, J., and Sackmann, E. (1994). Local measurements of viscoelastic moduli of entangled actin networks using an oscillating magnetic bead microrheometer. *Biophysical Journal*, 66(6):2210–2216.
- Zwanzig, R. and Bixon, M. (1970). Hydrodynamic theory of the velocity correlation function. *Physical Review A*, 2(5):2005–2012.